MOBILE-TO-MOBILE CHANNELS: STATISTICAL AND EMPIRICAL MODELS

A Dissertation by

Yazan Ibdah

M.Eng, Stevens Institute of Technology, Hoboken, NJ, May. 2005

B.Sc., Yarmouk University, Irbid, Jordan, Feb. 2003

Submitted to the Department of Electrical Engineering and Computer Science
and the faculty of the Graduate School of
Wichita State University
in partial fulfillment of
of the requirements for the degree of
Doctor of Philosophy

DECEMBER 2013

MOBILE-TO-MOBILE CHANNELS: STATISTICAL AND EMPIRICAL MODELS

The following faculty members have examined the final copy of this dissertation for form and content, and recommend that it be accepted in partial fulfillment of the requirement for the degree of Doctor of Philosophy with a major in Electrical Engineering.

Yanwu Ding, Committee Chair

Janet Twomey, Committee Member

Mahmoud E. Sawan, Committee Member

Vinod Namboodiri, Committee Member

Abu Asaduzzaman, Committee Member

Accepted for the College of Engineering

Vish Prasad, Interim Dean

Accepted for the Graduate School

Abu S. M. Masud, Interim Dean

DEDICATION

To my parents, my wife and children.

ACKNOWLEDGEMENTS

It has been an honor to have Dr. Yanwu Ding as my thesis advisor. I would like to thank her for her guidance and support during this research. This course in my life was very fruitful and full of knowledge.

TABLE OF CONTENTS

TABLE OF CONTENTS (continued)

TABLE OF CONTENTS (continued)

LIST OF FIGURES

LIST OF FIGURES (continued)

LIST OF FIGURES (continued)

LIST OF TABLES

LIST OF ABBREVIATIONS

AOA	Angles of arrivals
AOD	Angles of departure
AFD	Average fade duration
CW	Continuous wave
d	Distance
$\mathbb{E}$	Expectation operator
GPS	Global positioning system
h_t	Transmitter height
h_r	Receiver height
IV2IV	Inside-vehicle-to-inside-vehicle
IV2W	Inside-vehicle-to-walk
K	Spectral to the scatter power ratio
LCR	Level crossing rate
log	Logarithm base 10
LOS	Line-of-sight
MSE	Mean squared error
M2M	Mobile-to-mobile
NLOS	No line-of-sight
PDF	Probability density function
PL	Path loss
P_r	Received signal power
Rx	Receiver
Tx	Transmitter
$\mathbb{VAR}$	Variance operator

ABSTRACT

In this dissertation, we first present statistical models for cascaded Rayleigh Isotropic fading channels with and without line-of-sight (LOS). These models contain two individual summations and are therefore easy to implement with lower complexity. Detailed statistical properties, including auto- and cross-correlations of the in-phase, quadrature components of the channels, envelopes, and squared envelopes, are derived. The time-average statistical properties and the corresponding variance are also investigated to justify that the proposed models achieve good convergence performance.

Then, we present mobile-to-mobile (M2M) channel measurements at 2.1GHz and 700MHz bands in suburban and forest environments. Four test scenarios are considered for the transmitter (Tx) and receiver (Rx) placed inside traveling vehicles or on a test cart pushed at a walking speed. Channel models are proposed for path loss, shadowing, small-scale fading based on measurements. The path loss exponents were found between 1.2 to 7.7, and the reference path loss is found larger due to the placement of antenna inside vehicle. The mean of shadowing is close to 0, and the variance varies from 1.8 to 4.9. Measurements suggest that small-scale fading follows distributions of the Weibull and cascaded Rayleigh with LOS. The level crossing rate and average fading duration are also justified using the measurements.

Finally, we extend the work to study Non-Isotropic channels. New models are proposed based on cascaded Rayleigh with NLOS and LOS. We derived its statistical properties similarly to was done for the Isotropic channels. The mean absolute errors was adopted to verify the performance. Power spectrum analysis brought additional insight on this kind of channels.

CHAPTER 1

INTRODUCTION

1.1 Mobile-to-Mobile Wireless Fading Channels

Mobile-to-Mobile (M2M) communications has gained a lot of attention in the past few years. Mobile ad hoc wireless networks, wireless local area networks, vehicular-to-vehicular (V2V), and intelligence transportation systems [1–6] are rapidly growing fields nowadays. V2V applications such as traffic safety including airbags and anti-lock braking system, collision avoidance, and traffic monitoring. A conventional cellular base station can benefit from a M2M connection to extend its range, reduce power consumption, and increase its overall capacity [7].

All design and optimization stages require the use of the best channel model available to run propagations/simulations for any network. M2M channels are often more dynamic and less reliable than those in Fixed-to-mobile (F2M) channels. Accurate channel models are highly desirable for analysis and designs of systems in which terminals are no longer stationary In mobile networks, users are likely to be moving in different environments, and it is essential to use a proper channel model that reflects that environment properties. Therefore, new channel models are needed to better fit unstudied environments as we'll show later as dense scattering environments where the received signal experiences deep fades.

1.1.1 Fading

The received signal experience narrow band fading, variations of received signal over time, due to physical phenomena of wireless channel like scattering, reflection, and diffraction.

Scattering which is our focus in our study is resulted when the obstacle/s dimensions between the Tx and Rx are much smaller than the wavelength of the transmitted signal. Reflection is resulted when transmitted signal is obstructed by an object with dimensions that are larger than the signal wavelength. Diffraction occur when the signal is reflected from a surface that has edges.

Fading can be classified as path loss, large-scale and small-scale fading.

Path loss The path loss represent the mean of the received signal at a specific distance. It is calculated by averaging the received signal over areas that has same separation from the Tx. Therefore, any interference associated to a specific location will be avoided and helps in predicting the average of the received signal with no interruption.

Large-scale Usually refers to shadowing fading which is the local average of the variations in the received signal around the path loss. The local average of the received signal can be estimated using a sliding window over distance. The window size is chosen based on the operating frequency and its coherence distance.

Small-scale These are small variations in the received signal are caused by multi paths. When different copies of the originally transmitted arrive at the Rx with different traveling paths, these copies can be added constructively or destructively. As a result, received signal will experience fast or slow fading depending how fast these changes are. If the changes happen during one symbol, it is fast fading otherwise it is slow fading.

1.1.2 Statistical Properties

Second-Order Properties

Correlations are key properties when studying wireless fading channels. These properties measure how fast the channel changes over time and movement. Correlation functions can be spatial, frequency, and temporal correlations. Spatial correlations measures channel changes by having multiple antennas at the Tx and Rx. It is important measure for the potential benefit of path diversity. Frequency correlation measures frequency selectivity of a channel and how channel changes with respect the frequency. When the channel frequency response varies with frequency, this results in a broad envelope in time domain. The temporal correlations functions which are our focus in this work, measure how fast the channel changes over time. It is important for measure for the quality of the channel, as it measure how long a channel property will remain in the channel. Due to relative motion between the Tx and Rx, fading becomes correlated and varies with time.

Higher-Order Properties

Level crossing rate (LCR) and average fading duration (AFD) are important properties when studying wireless fading channels. The LCR is a measure of channel stability and how often it varies over time. It is the number of crossings per second that the channel envelope crosses a specific threshold in the positive (or negative) direction. While the AFD, is a measure of the how long the channel envelope remains below that specific threshold.

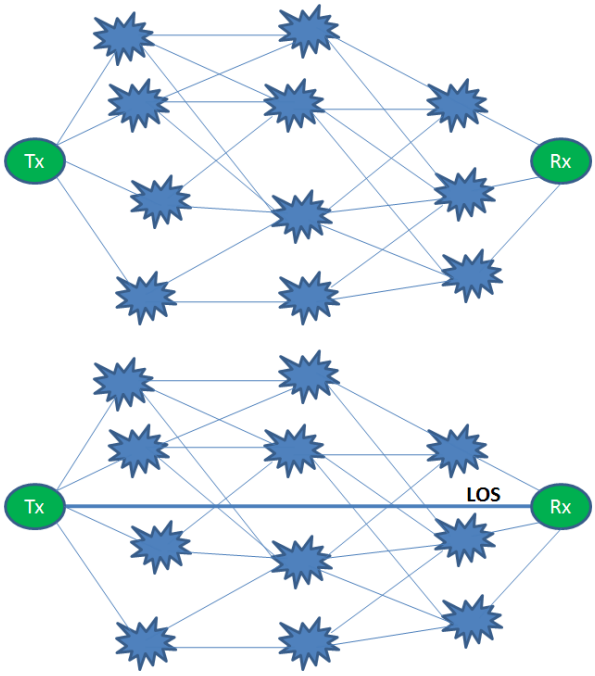

Figure 1.1: Multiple scattering environment for mobile-to-mobile without and with LOS.

1.1.3 Scattering

In Fig. 1.1, a scattering environment is shown for M2M with and without LOS. Scattering can be classified in to Isotropic and non-Isotropic. Isotropic scattering assumes the use of omni-directional antennas and angles of departures (AOD) and arrivals (AOA) of scatters are uniformly distributed around the transmitter (Tx) and the Receiver (Rx). This assumption is valid when the channel is a result of infinite number of scatters with equal weights. Empirical channel measurements in [8, 9] indicated that this doesn't occur in all M2M scenarios, and has a great impact on channel properties. This inspire us to study the general case, the no-isotropic scattering. While in non-isotropic scattering, the channel is resulted of non-uniform scattering or Tx and Rx use directional antennas.

Field measurements can be conducted using a continuous wave (CW) which is an unmodulated signal. Using the measured received signal, the channel can be estimated, as the original transmitted signal is known for the Rx. The estimation includes the path loss, shadowing, and small-scale components.

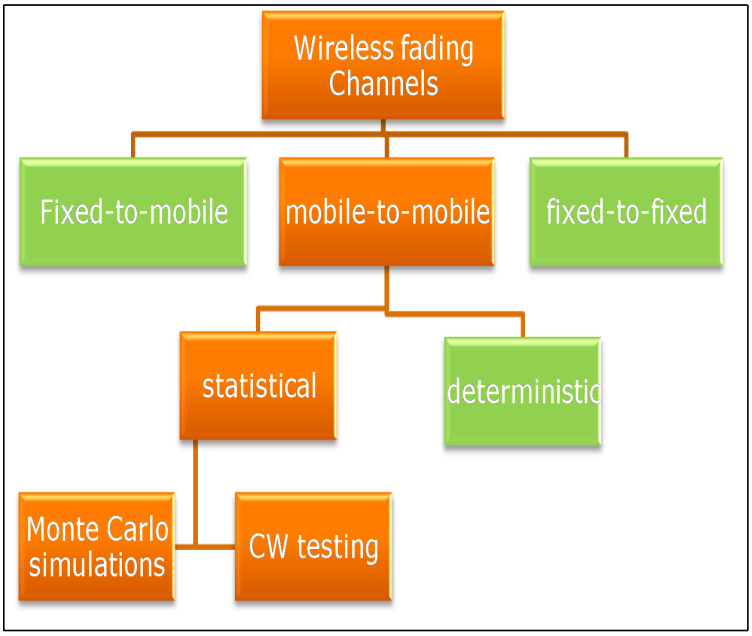

Figure 1.2: Statistical M2M channel models

1.2 M2M Statistical Models

Wireless fading channel models can be classified into two groups as shown in Fig. 1.2, deterministic and statistical models. Deterministic models don't require trials, and a single trial is enough to get desired properties, but much higher complexity and cost compared with statistical models as it require more uncorrelated signals [10, 11]. On the other hand, using statistical channel models, the desired statistical properties can be achieved by taking the average of a number of trials. Statistical channel models require fewer uncorrelated

sinusoids, but a number of trials are required to achieve the desired properties. For these advantages of statistical models, we focus on this type of models in this work.

Statistical models for Mobile-to-Mobile (M2M) channels based on cascaded Rayleigh fading seems few in the literature (most models are for M2M single Rayleigh fading). No channel models available in the literature for M2M appropriate to simulate scenarios in highly dense scattering environments such as suburbs, forests and outdoor-to-indoor (O2I), inside-vehicle-to-inside-vehicle (IV2IV), and inside-vehicle-to-walk (IV2W) scenarios. M2M channel measurements in dense and forest areas are not many.

The M2M mathematical model, which was later referred to as the mathematical reference model, was presented [12, 13]. Pioneering statistical models for M2M channels are found in [14, 15], where double-ring model was proposed to represent isotropic scatters nature around Tx and Rx. Omni-directional antennas and isotropic scattering were assumed around the transmitter (Tx) and the receiver (Rx). The single ring channel model was originally proposed to model a fixed-to-mobile (F2M) channel in [16]. For the scenario where both the Tx and the Rx are in motion, and based on the work in [12, 13]. This idea was applied on both mobile stations in [14], where the double-ring concept was used to derive a new channel model model called a "double-ring". The model is based on uniformly scattering applied around both transmitter and receiver. It defines two rings of uniformly spaced scatters with different radii, one around the transmitter and another around the receiver. In [15], a modification to the double-ring model was proposed to generate multiple uncorrelated complex faded envelopes.

The double-ring became popular over the past few years. It was extended in [17], and a new statistical channel model was proposed based on Rician channel where a line of sight

(LOS) component exists between Tx and Rx. Similarly to work done for F2M in [18,19] can be found in [17], were a LOS component was introduced.

Measurements in the 5GHz band were reported for V2V communications in [20–25]. In [21], testing was conducted in small city, urban and suburban areas. It was indicated that severe (worse than Rayleigh) fading was observed for several scenarios such as urban and small city. Similar scenarios were tested in [24] such as urban, suburban, motorway and highway. The received signal results were compared to analytical functions, such as the Rice, the Rayleigh distribution. Results show that LOS factor was dominant in those power measurements. Even though the Rician distribution was the closest fit, measurements indicates that possible "close to" Rician distribution can be a better fit. In [23], measurements show that a Double-Rayleigh distribution is better fit to received power measurements than a single Rayleigh in O2I scenarios. In [25], measurements were conducted in a dense scattering urban environment. Although the Rx was moving in a limited area, while the Tx had more freedom, same conclusions to the ones in [23] were obtained in [25].

The cascaded-Rayleigh model represents the second approach in statistical models. In [26, 27], the concept of a mix of single, double, triple Rayleighs was introduced to represent a general M2M channel. Testing was conducted in urban and forest environments. Results show that under certain conditions the double Rayleigh will dominate.

1.3 M2M Channel Measurements

Tests and measurements for V2V channels have been conducted in highway, suburban, and rural roads [20–25, 28–31]. The path loss, power-delay profiles, and delay-doppler spectra have been mainly analyzed for the 5GHz channel band [20–22, 30, 31]. Narrow-band

measurement in the 5.9GHz channel has been conducted with the doppler spread and coherence time characterized [32]. V2V Broad-band measurements have also been presented in the 700MHz band [30, 31]. While these studies focus on suburban, rural areas, tunnels, and some application-specific scenarios such as traffic congestion, M2M channel measurements in dense woody and forest areas are not many [28]. Characterization of the channel in areas play critical roles in emergency rescue or community tree service. That motivated us to conduct channel measurement testing areas with dense woods.

The available empirical models for M2M near ground communications are limited. The two-ray model [33] which was originally proposed for cellular communications, is believed to represent the M2M Path loss in rural scenarios [34]. A very recent measurements were presented in [35] under LOS condition in rural, urban, suburban, and highways suggested that a two-ray model is a good fit for rural areas but not for the rest of tested areas. In general, most suburbs and rural areas streets are determined by the geography of the land, and straight flat streets and LOS conditions are not always guaranteed.

Despite that many of possible scenarios were not tested as we show later in this paper, the results in [34] in general provide a good baseline for same/opposite/convoy movement, eg. the path loss exponent was found low for highway rural, and urban scenarios, but the data was collected for suburban was not enough to draw this conclusion. This is clearly shown in [36] where breakpoints were found in some in suburban measurements. These are common in micro cells when the transmit antennas are at lower heights compared with macro cells. Therefore, it is expected to have it in near ground measurements. Fixed-to-Fixed (F2F) Empirical models based on measurements in foliage areas can be found in [29, 37–40], where additional Path loss rather than the power law of distance, accurse in dense scattering areas.

In other words, the Path loss (function of distance) is no longer a straight line, but has an arc shape on the logarithmic scale. This is expected a better fitting for the results in [36] and break-points can be integrated in the model.

1.4 M2M Non-isotropic Models

A number of non-uniform distributions were proposed to fit the AOA and AOD in a non-isotropic scattering. Mainly are Gaussian [41], Quadrate [42], truncated Laplace [43,44], truncated uniform [45], cosine [46], and von Mises [8] distributions. Measurements in [47] suggested that von Mises distribution is a good fit for AOA and can approximate other non-uniform distributions. In [9], measurements were conducted in M2M campaigns in both a highway and an urban area. A 3-D non-isotropic scattering Rician model was proposed; and using von Mises distribution a good fit is shown with LCR and AFD.

In [47], the power spectrum density (PSD) and correlation properties for Rician F2M channel were derived for 3-D under non-isotropic scattering. Later, the psd was adopted in [48], to generate Rayleigh non-isotropic channel model using gaussian samples as an input. The spectrum shaping filter coefficients in [48] were chosen using an adaptive algorithm to produce the desired spectrum presented in [47]. A statistical Rayleigh channel model is proposed in [49], where both auto- and cross-correlations of the Rician proposed channel validated the psd and correlation in [47].

Multiple-input multiple-output (MIMO) for non-isotropic scattering was investigated in [50, 51]. A M2M statistical channel model based on cascaded-Rayleigh was proposed in [51]. The auto- and cross-correlations were derived with the assumption that AOD and AOA follow von Mises distribution. We'll refer to this model as a reference model in this

work. Rician fading channel was studied in [50] and proposed a geometric model based on a single-, double-bounced, and LOS. In [50, 51], Space-time correlation functions were derived for their models.

1.5 Motivation for the work

1.5.1 Statistical Models

It is clear now that the double-ring statistical channel model is not suitable for all M2M environments. Measurements in dense scattering environments confirm that the M2M channels may undergo cascaded Rayleigh fading (more severe than single Rayleigh fading). The proposed statistical models can be applied to simulate the underlying channels such as dense scattering environments, O2I, and cases where large separations between Tx and Rx are much larger than the max of both radii rings [51]. The time required to generate a sample of the channel is a key objective for any model. Motivated by the work in [13, 16–19, 23, 52], the proposed models have fast convergence, low number of sinusoids, and require a small number of trials to achieve the desired properties.

1.5.2 Empirical Models

The available V2V measurements in the literature are mainly for two cases, either both Tx and Rx are traveling in same (convoy) or opposite direction. Other possibilities such as approaching intersections and random movements are not many. Vehicle penetration loss was not taken into account in most V2V measurements, as majority of testing had antennas on the car rooftop, and the effect of having the antenna inside the vehicle was left unexplored. There is a high possibility that the mobile device be located inside a bag or

perse or pocket, and at a height that is lower than the rooftop of a vehicle. To complete the picture and incorporate these factors, we conducted IV2IV measurements scenarios in two different frequency bands. In addition, to the authors knowledge, there are no outdoor IV2W measurements available in the literature.

1.5.3 Non-isotropic Models

The assumption of M2M channel model is isotropic scattering, uniform distribution of AOD and AOA, is not always the case. Measurements suggested non-isotropic scattering is a better fit to measurements in urban and highways than isotropic. The von Mises distribution approximates some important distributions like uniform, impulse, and Gaussian. Therefore, we adopt this distribution to generate non-uniform AODs and AOAs. The auto-, cross-correlation, and power spectrum for the non-isotropic complex channel are found to be different than for the isotropic models. This motivated us to in-deep study the effects of its specific parameters and present generalization to isotropic study.

1.5.4 Performance Evaluation

M2M cascaded Rayleigh fading channel models are sparse in the literature. Therefore, we compare proposed channel models namely models A and B with the double-ring channel model. It is worth to mention that double-ring and the proposed models are for different categories of M2M channels. The comparison is solely for the illustration of complexity and performance of the proposed models. To investigate the performance of convergence, we examine the mean square error (MSE) between simulated autocorrelation and the theoretical for Models A, B, and double-ring model. The autocorrelation, as the key statistical

property, was chosen for complexity evaluation. The speed of convergence was measured by the averaged CPU time elapsed when generating one channel.

Since channel behavior can vary significantly with the frequency [32], this work presents analysis for IV2IV and IV2W Narrow-band continuous wave (CW) measurements in 700MHz and 2.1GHz frequency band in dense scattering environments. Proposed path loss models for forest were compared to existing F2F models, although it represent a different category, using MSE. While Path loss and large scale measurements in suburban where compared to existing V2V results. Small-scale parameters were estimated and used to compare the measurements with Rician, Cascaded-Rayleigh, and Weibull distributions.

In addition to models convergence tests used for isotropic channels, a new test is added to ensure stability of the proposed models, namely the mean absolute errors (MAE) of auto- and cross correlations. Power spectrum is presented to bring additional dimension to the study by looking at the fourier transform of the auto- and cross correlations for proposed channel models.

1.6 Contributions of Dissertation

1.6.1 Statistical Models

As presented in Chapter 2, contributions to this dissertation can summarized as following. We proposed new statistical models for M2M channels that experience cascaded Rayleigh fading without and with LOS.

We derived statistical properties for proposed models. This includes auto and cross-correlations of the in-phase, quadrature components, and squared envelopes of the channels are derived. The time-average statistical properties and the corresponding variance were

also derived to confirm that the proposed models have good convergence performance. Some derivations and proofs are too long, hence are outlined in the appendices in Appendices. We also proposed approximations for Average fading duration (AFD) and Level crossing rate (LCR) for Cascaded Rayleigh with NLOS. Simulations were compared to its theoretical to demonstrate the agreement between them.

1.6.2 Empirical Models

Our contributions to this task, as presented in Chapter 3, can be summarized as following. We conducted IV2IV and IV2W measurements in summer 2012 with and without visibility in the 2.1GHz and 700MHz bands in highly dense scattering environments. Three different locations were selected in northern New Jersey known for its rainforest trees. We presented measurements results in a great detail by estimating the received signal in terms of path loss fading, large-scale or shadowing, and small-scale fading for different scenarios. We proposed new empirical models for IV2IV in dense areas for different components of the received signal. We validate the proposed statistical models in Chapter 2 based on two cascaded Raleigh with LOS principle. We used the concept of a mix of single and cascaded Rayleigh in an attempt to find best distribution to fit measured data.

The available forms for both LCR and AFD for M2M Rician were not correct in the literature. The right representations were derived for this type of channel. There were no forms available for LCR and AFD for M2M Weibull channel. Therefore, we derived these properties for this channel as well.

1.6.3 Non-isotropic Models

Some of contributions in chapter 4 are similar to ones in chapter 3, but for a generalized form as the isotropic model becomes a special case of non-isotropic model. We begin by proposing new statistical channel models based on cascaded-Rayleigh with LOS for M2M channels under non-isotropic scattering. We derived major statistical properties for proposed models such as auto and cross-correlations of the in-phase, quadrature components. The mean absolute errors (MAE) of auto- and cross correlations of proposed Models are presented to ensure that the proposed models have good convergence and stable performance. The power spectrum analysis results shed some light on key parameters in these models.

1.7 Dissertation Organization

The remainder of this dissertation is organized as follows: Chapter 2 presents statistical channel models. It starts with a brief review of the general multiple Rayleigh channel transfer function and presents the proposed channel models without LOS and with LOS. Then, detailed statistical properties of the proposed models are presented. Simulation results are provided next. After that, the chapter concludes with a summary of observations.

In chapter 3, channel measurements are presented. It begins with measurement setup and test scenarios. Then, M2M channel models for path loss, shadowing, and small-scale fading based on the measured received signal power are presented. After that, level crossing rate and average fade duration for the channels are evaluated. Observations and conclusions are presented at the end of the chapter.

The study in chapter 4 is an extension to the work in chapter 2. A brief presentation for

existing models with NLOS and techniques to generate Non-isotropic distribution is followed by proposed simulation models based on Cascaded Rayleigh with LOS. Then, statistical properties are derived for models with NLOS and LOS. The effects of different parameters on the channel behavior are investigated later by deep analysis for the power spectrum. Finally, the chapter is concluded with observations and conclusions. Derivations of statistical channel properties are presented in Appendices. Chapter 5 concludes the thesis with conclusions and future work.

CHAPTER 2

STATISTICAL SIMULATION MODELS FOR M2M FADING CHANNELS

2.1 Literature Review

Mobile-to-mobile communications have found more and more applications in systems where the terminals and nodes are no longer stationary [53,54], such as mobile ad hoc wireless networks [1], wireless local area networks [2], intelligence transportation systems [3–5], and vehicular-to-vehicular systems [6]. Consequently, successful development of statistical models or models for mobile-to-mobile (M-M) channels is inevitable in order to understand the statistical properties of the underlying channels and effective designs for the systems. A pioneering mathematical reference model for M-M channels is found in the earlier work of Akki and Haber [12] and Akki [13]. This analysis is then extended to account for scattering in three dimensions by Vatalaro and Forcella [55]. A modified statistical model for suburban outdoor-to-indoor M-M communications channels has been discussed in [23]. A double-summation-of-sinusoids statistical model is applied to simulate M-M channels, assuming omni-directional antennas and isotropic scattering around the transmitter (Tx) and the receiver (Rx) [14]. Due to the uniform scattering around the Tx and Rx, the statistical model in [14] is also referred to as a "double-ring" statistical model (the single-ring statistical model is proposed for fixed-to-mobile channels [16]). The double-ring model is further modified to generate multiple uncorrelated complex faded envelopes using orthogonal in-phase and quadrature components [15]. The modification offers a faster convergence and lower variance at higher complexity. The double-ring concept is also applied to modeling M-M channels where a line-of-sight component exists between the Tx and Rx [17] (the single-ring-based

fixed-to-mobile Rican channel models can be found in [18,19]). In [51], stochastic properties for M-M narrow-band channels are derived from a geometrical two-ring scattering model, assuming that both the transmitter and the receiver are surrounded by an infinite number of local scatters. The model is further extended to a three-ring scattering model [56].

While the double-ring model characterizes a category of mobile-to-mobile channels that follow a Rayleigh fading distribution, various measurements in dense scattering urban and forest environments where signals diffract from street corners, building edges, and moving vehicles, suggest that if large separations between the Tx and Rx are much larger than both radii rings [51] at the TX and Rx, then the mobile-mobile channels follow fading distributions that are more severe than a single Rayleigh fading. In [23], the outdoor-to-indoor M-M radio channel measurements show that the received power follows a double-Rayleigh distribution rather than a single Rayleigh distribution. Similar observations are seen in the measurements [25], whereas the Tx is moving in within a circle of a 1 m and the RX are randomly chosen within a 10 m by 10 m square with no line of sight. The measurements in [21, 24, 57] indicate that severe (worse than Rayleigh) fading in vehicle-vehicle channels is observed in small cities, urban, and suburban areas, motorways, and highways.

In [26, 27], the concept of a mixture of single, double, and triple Rayleigh distributions is introduced to represent a general M-M channel. The general multiple Rayleigh channel transfer function was initially suggested in [23] for studying dense scattering environments. Effective statistical models for cascaded or multiple Rayleigh fading M-M channels seem sparse in the literature. In this paper, we develop two statistical models for a cascaded Rayleigh fading channel with no line-of-sight (NLOS) and extend the models to channels

with LOS. The models contain two individual summations; therefore, they are easy to implement with lower complexity. With appropriately chosen parameters, the proposed models can achieve the desirable statistical properties in a small number of trials, and provide satisfactory convergence performance. Detailed statistical properties, including auto- and cross-correlations of the in-phase, quadrature components of the channels, envelopes, and squared envelopes are derived for the models. The time-average statistical properties and corresponding variance are also investigated to justify that the proposed models can achieve good convergence performance. Extensive Monte Carlo simulation results are provided for various statistical properties to validate the proposed models.

2.2 Statistical Channel Models for Cascaded Rayleigh Fading Channels

2.2.1 Transfer function of cascaded Rayleigh fading channels

In highly dense scattering environments, the transmission path between the Tx and Rx are composed of many scattering paths. Fig. 1.1 illustrates a multiple scattering environment between two mobile terminals with no LOS exists between the Tx and Rx (first graph) and a LOS (second graph). We assume that the distance between the transmitter and receiver is much larger than both radii of the scattering rings at the Tx and Rx, the channel in the first graph follows cascaded Rayleigh distribution with NLOS, and that in the second graph cascaded Rayleigh distribution with LOS.

A cascaded Rayleigh transfer function is suggested in [23], assuming that the two groups of scatter at the transmitter and the receiver are stationary and located a relatively large distance apart with a separation distance of $D \gg R_t + R_r$, where R_t and R_r are the radii of

the scatters around the Tx and Rx, respectively. The transfer function is presented as

$$g_{\text{general}}(t) = \sum_{n=1}^{N} A_n G_{_T}(k_{_{Tn}}) e^{j(\omega_{_{Tn}} t + \Phi_{_{Tn}})} \sum_{m=1}^{M} B_m G_{_R}(k_{_{Rm}}) e^{j(\omega_{_{Rm}} t + \Phi_{_{Rm}})} \tag{2.2.1}$$

where subscripts T and R are associated with Tx and Rx, respectively, $A_n, \Phi_{_{Tn}}, n = 1, \cdots, N$, are the identically distributed random (i.i.d) amplitude and phase of N scatter components around the Tx, $B_m, \Phi_{_{Rm}}, m = 1, \cdots, M$ are the i.i.d amplitude and phase of M around the Rx, $G_{_T}$ and $G_{_R}$ are antennas gains, $k_{_{Tn}}$ and $k_{_{Rm}}$ are unit vectors corresponding, respectively, to the direction of departure and arrival of the n-th scatter at Tx and m-th scatter at the Rx, and $\omega_{_{Tn}}$ and $\omega_{_{Rm}}$ are Doppler spreads of the Tx and Rx. Efficient statistical models for (2.2.1) were left unexplored. In this section, we develop four channel models (Models A, B, C, and D) for the cascaded Rayleigh fading channels without and with LOS.

2.2.2 Statistical channel models without LOS

In this subsection, two models, namely Models A and B, are presented for cascaded Rayleigh fading without LOS in (2.2.1).

Model A

In the statistical channel model, the complex scattering components in cascaded Rayleigh fading channels are given by

$$g_{_A}(t) = \sqrt{\frac{\sqrt{2}}{Q}} \sum_{n=1}^{Q} e^{j\left(2\pi f_1 t \cos(\gamma_n) + \theta_n\right)} \sqrt{\frac{\sqrt{2}}{P}} \sum_{m=1}^{P} e^{j\left(2\pi f_2 t \cos(\zeta_m) + \Phi_m\right)} \tag{2.2.2}$$

where Q and P designate the number of scatters around the Tx and Rx, respectively, f_1 and f_2 are the Doppler's shift frequencies, θ_n and $\Phi_m \in [-\pi, \pi), n = 1, \cdots, Q, m = 1, \cdots, P$, are the phase shifts for each scatter from the Tx and to the Rx and they are i.i.d for all n and

m. γ_n represents the angle of departure for the n-th scatter at the Tx, and ζ_m is the angle of arrival for the m-th scatter at the Rx, given by, respectively,

$$\gamma_n = \frac{2n\pi - \pi + \psi}{4Q},\ \zeta_m = \frac{2m\pi - \pi + \varphi}{2P}, \tag{2.2.3}$$

where $\psi,\ \varphi$ are independent and uniformly distributed in $[-\pi, \pi)$. While those angles can be chosen as either dependent on or independent of n and m [14, 16, 17, 19], we choose them to be independent in order to reduce the complexity of the model.

Model B

The angles of departures and arrivals for Model A, as indicated in (2.2.3), are in $[0, \pi/2)$ and $[0, \pi)$, respectively. In fact, smaller angles of departures and arrivals in the scatters are expected for the channels under discussion, because the distance between Tx and Rx is relatively large with $D \gg R_t + R_r$. However, our simulations suggest that if the range of angles of arrivals is chosen smaller, the convergence performance of Model A degrades, especially for the cross-correlation between the in-phase and quadrature components. We seek an alternative model with an improved performance and the angles of departures and arrivals are both in $[0, \pi/2)$ to achieve a better representation of scattering patterns in the channels between a TX and Rx with larger separations. We assume that Model B has the following form: $g_{_B}(t) = \big(g_{1c}(t) + jg_{1s}(t)\big)\big(g_{2c}(t) + jg_{2s}(t)\big)$, where $g_{ic}(t)$ and $g_{is}(t), i = 1, 2$, are the sinusoidal functions which characterize, respectively, the scattering at the Tx and Rx. Here, we present the steps to obtain the functions at Tx, $g_{1c}(t)$ and $g_{1s}(t)$, while same procedure applies to obtain $g_{2c}(t)$ and $g_{2s}(t)$ at the Rx.

Let $\alpha_k = \frac{2k\pi - \pi + \psi}{K_{\text{Tx}}}$, and $\theta_k,\ k = 1, \cdots, K_{\text{Tx}}$, denote the angle of departure and phase

for the k-th scatter at the Tx, where $\psi,\ \theta_k$ are statistically independent and uniformly distributed in $[-\pi, \pi)$ for all k, and K_{Tx} is the number of scatters around the Tx. Next, we evaluate a summation of series of exponentials: $\sum_{k=1}^{K_{\text{Tx}}} \exp\big(j(2\pi f_1 t\cos(\alpha_k)+\theta_k)\big)$. While the summation admits a similar expression as the first summation in Model A, we consider a special case, $K_{\text{Tx}} = 4N$ with $N > 1$ being an integer. The summation is obtained as four terms corresponding to the quarters of K_{Tx}, $\sum_{k=1}^{K_{\text{Tx}}} \exp\big(j(2\pi f_1 t\cos(\alpha_k)+\theta_k)\big) = \sum_{\ell=0}^{3}\Omega_\ell$, where $\Omega_\ell = \sum_{n=\ell N+1}^{(\ell+1)N} \exp\Big(j\big(2\pi f_1 t\cos(\alpha_n)+\theta_n\big)\Big) = \sum_{n=1}^{N} \exp\Big(j\big(2\pi f_1 t\cos(\alpha_n+\frac{\ell\pi}{2})+\theta_{n+\ell N}\big)\Big),\ \ell = 0,\cdots,3$. Introducing uniform distributed random phases $\Theta_n \in [-\pi,\pi), n = 1,\cdots,N$, where Θ_n is independent of ψ, θ_k for all n and k, one can rewrite $\Omega_i, i = 1,2,3$ as

$$\Omega_1 = \sum_{n=1}^{N} \exp\Big(j\big(2\pi f_1 t\cos(\alpha_n+\frac{\pi}{2})-\Theta_n\big)\Big), \tag{2.2.4}$$

$$\Omega_2 = \sum_{n=1}^{N} \exp\Big(j\big(2\pi f_1 t\cos(\alpha_n+\pi)-\theta_n\big)\Big), \tag{2.2.5}$$

$$\Omega_3 = \sum_{n=1}^{N} \exp\Big(j\big(2\pi f_1 t\cos(\alpha_n+\frac{3\pi}{2})+\Theta_n\big)\Big). \tag{2.2.6}$$

The range of angles of departure in $\Omega_\ell,\ \ell = 0,\cdots,3$ is in $(0,\pi/2)$ as specified by $\alpha_n,\ n = 1,\cdots,N$ (the range give by $\alpha_k,\ k = 1,\cdots,K_{\text{Tx}}$ is in $(0,\pi/2)$). We assign the sinusoidal functions at the Tx, i.e. $g_{1c}(t)$ and $g_{1s}(t)$ equal, respectively, to the terms associated with $\cos(\alpha_n)$ and $\sin(\alpha_n)$ in $\sum_{\ell=0}^{3}\Omega_\ell$, along with a normalizing factor. Notice $\Omega_0+\Omega_2 = 2\sum_{n=1}^{N}\cos\big(2\pi f_1 t\cos(\alpha_n)+\theta_n\big)$, and $\Omega_1+\Omega_3 = 2\sum_{n=1}^{N}\cos\big(2\pi f_1 t\sin(\alpha_n)+\Theta_n\big)$. We obtain $g_{1c}(t) = \sqrt{\frac{\sqrt{2}}{N}}\sum_{n=1}^{N}\cos\big(2\pi f_1 t\cos(\alpha_n)+\theta_n\big)$, and $g_{1s}(t) = \sqrt{\frac{\sqrt{2}}{N}}\sum_{n=1}^{N}\cos\big(2\pi f_1 t\sin(\alpha_n)+\Theta_n\big)$ for Model B.

Let $\beta_k = \frac{2k\pi-\pi+\varphi}{K_{\text{Rx}}}$, and $\Phi_k,\ k = 1,\cdots,K_{\text{Rx}}$ denote the angle of arrival and phase for the k-th scatter at the Rx, where $\varphi,\ \Phi_k$ are uniformly distributed in $[-\pi,\pi)$, and they

are impendent for all k, and K_{Rx} is the number of scatters around the Rx. Evaluating the summation $\sum_{k=1}^{K_{\mathrm{Rx}}} \exp\Big(j\big(2\pi f_2 t\cos(\beta_k)+\Phi_k\big)\Big)$ for $K_{\mathrm{Rx}}=4M$, and following similar procedure describe above, we obtain $g_{2c}(t)=\sqrt{\frac{\sqrt{2}}{M}}\sum_{m=1}^{M}\cos\big(2\pi f_2 t\cos(\beta_m)+\Phi_m\big)$, and $g_{2s}(t)=\sqrt{\frac{\sqrt{2}}{M}}\sum_{m=1}^{M}\cos\big(2\pi f_2 t\sin(\beta_m)+\Psi_m\big)$ for Model B. The range of angles of arrivals at the Rx is in $(0,\pi/2)$ as specified by $\beta_m,\ m=1,\cdots,M$. In summary, Model B is expressed as

$$g_{_B}(t)=\big(g_{1c}(t)+jg_{1s}(t)\big)\big(g_{2c}(t)+jg_{2s}(t)\big) \tag{2.2.7}$$

where $g_{ic}(t)$ and $g_{is}(t), i=1,2$ are defined as

$$g_{1c}(t)=\sqrt{\frac{\sqrt{2}}{N}}\sum_{n=1}^{N}A_n(t), g_{1s}(t)=\sqrt{\frac{\sqrt{2}}{N}}\sum_{n=1}^{N}C_n(t), \tag{2.2.8}$$

$$g_{2c}(t)=\sqrt{\frac{\sqrt{2}}{M}}\sum_{m=1}^{M}B_m(t), g_{2s}(t)=\sqrt{\frac{\sqrt{2}}{M}}\sum_{m=1}^{M}D_m(t), \tag{2.2.9}$$

$A_n(t)=\cos\big(2\pi f_1 t\cos(\alpha_n)+\theta_n\big), C_n(t)=\cos\big(2\pi f_1 t\sin(\alpha_n)+\Theta_n\big), n=1,\cdots,N, B_m(t)=\cos\big(2\pi f_2 t\cos(\beta_m)+\Phi_m\big)$, and $D_m(t)=\cos\big(2\pi f_2 t\sin(\beta_m)+\Psi_m\big), m=1,\cdots,M$, f_1 and f_2 are the Doppler's shift frequencies, $\theta_n,\ \Theta_n\in[-\pi,\pi), n=1,\cdots,N$ are the phase shifts in the n-scatter at the Tx, $\Phi_m,\ \Psi_m,\in[-\pi,\pi), m=1,\cdots,M$ are the phase shifts in the m-scatter at the Rx and are i.i.d for all n and m, α_n is the angle of departure of the n-th scatter at the Tx, and β_m is the angle of arrival of the m-th scatter at the Rx, and they are calculated, respectively, as

$$\alpha_n=\frac{2n\pi-\pi+\psi}{4N},\ \beta_m=\frac{2m\pi-\pi+\varphi}{4M}, \tag{2.2.10}$$

where $\psi,\ \varphi$ are independent and uniformly distributed in $[-\pi,\pi)$, and they are independent to all the phases at the Tx and Rx. It is indicated that a statistical M-M model may result in

faster convergence rates by choosing a smaller range of angles of arrivals and departures [14]. Our simulations justify the observation as well. Compared with Model A, Model B has faster convergence and requires fewer number of trials to converge to the desired statistical properties.

2.2.3 Statistical channel models with LOS

Adding the LOS component to Models A and B, we present two models for cascaded Rayleigh fading channels with LOS, namely Models C and D, as

$$\text{Model C: } h_{_C}(t) = \frac{g_{_A}(t) + \sqrt{2K}e^{j(2\pi f_3 t\cos(\phi_3)+\phi_0)}}{\sqrt{2(1+K)}}, \tag{2.2.11}$$

$$\text{Model D: } h_{_D}(t) = \frac{g_{_B}(t) + \sqrt{2K}e^{j(2\pi f_3 t\cos(\phi_3)+\phi_0)}}{\sqrt{2(1+K)}}, \tag{2.2.12}$$

where K is spectral to the scatter power ratio, ϕ_0 is uniformly distributed in $[-\pi, \pi)$, f_3 is the Doppler frequency caused by the relative velocity, because both Tx and Rx have mobility, ϕ_3 is the relative angle between the relative movement and the LOS component, and the values of f_3 and ϕ_3 are given, respectively, by [17] as

$$f_3 = \frac{\left|\sqrt{\left(|v_1|\cos(\phi_{12}) - |v_2|\right)^2 + \left(|v_1|\sin(\phi_{12})\right)^2}\right|}{\lambda} \tag{2.2.13}$$

$$\phi_3 = \cos^{-1}\left(\frac{|v_1|^2 + |v_3|^2 - |v_2|^2}{2|v_1||v_3|}\right) + \phi_1 \tag{2.2.14}$$

where v_1 and v_2 are, respectively, the speeds of the Tx and Rx, v_3 is the relative speed calculated by $v_3 = f_3\lambda$, λ is the wavelength of the carrier, ϕ_1 is the angle between the Tx and the LOS, and ϕ_{12} is the angle between the Tx and Rx directions. Model D has a slightly additional complexity compared to Model C, due to the higher complexity in $g_B(t)$ than in $g_A(t)$. However, as indicated by the simulation results, Model D provides faster convergence to the desired statistical properties even for a lower value of K.

2.3 Statistical Properties of Proposed Models

Because Models A and B, $g_{_A}(t)$ and $g_{_B}(t)$, have the same statistical properties, as do Models C and D, $h_{_C}(t)$ and $h_{_D}(t)$, we focus on Models B and D when representing the statistical properties in this section. To make notations less bulky, we drop the subscripts, and use $g(t)$ and $h(t)$ to present, respectively, the models without and with LOS.

2.3.1 Second-order statistics for Model B

Let $g_c(t) = \mathrm{Re}\big(g(t)\big)$ and $g_s(t) = \mathrm{Im}\big(g(t)\big)$ be the real (in-phase) and imaginary (quadrature) parts of Model B. The autocorrelation, the cross-correlation of the in-phase, quadrature components, and the autocorrelation of complex envelopes are given below. Steps for the proof are presented in Appendix A.

$$R_{g_cg_c}(\tau) = \mathbb{E}\big[g_c(t+\tau)g_c(t)\big] = J_0(2\pi f_1\tau)J_0(2\pi f_2\tau) \tag{2.3.1}$$

$$R_{g_sg_s}(\tau) = \mathbb{E}\big[g_s(t+\tau)g_s(t)\big] = R_{g_cg_c}(\tau) \tag{2.3.2}$$

$$R_{g_cg_s}(\tau) = \mathbb{E}\big[g_c(t+\tau)g_s(t)\big] = 0, R_{g_sg_c}(\tau) = \mathbb{E}\big[g_s(t+\tau)g_c(t)\big] = 0 \tag{2.3.3}$$

$$\begin{aligned} R_{gg}(\tau) &= \frac{1}{2}\mathbb{E}\big[g(t+\tau)g^*(t)\big] \\ &= \frac{1}{2}\big(R_{g_cg_c}(\tau) + R_{g_cg_s}(\tau) + R_{g_sg_c}(\tau) + R_{g_sg_s}(\tau)\big) = J_0(2\pi f_1\tau)J_0(2\pi f_2\tau) \end{aligned} \tag{2.3.4}$$

$$\begin{aligned} &R_{|g|^2|g|^2}(\tau) = \mathbb{E}\big[g_c^2(t)g_c^2(t+\tau) + g_s^2(t)g_c^2(t+\tau) + g_c^2(t)s_s^2(t+\tau) + g_s^2(t)g_s^2(t+\tau)\big] \\ &= 4 + 4J_0^2(2\pi f_1\tau) + 4J_0^2(2\pi f_2\tau) + 4J_0^2(2\pi f_1\tau)J_0^2(2\pi f_2\tau) + \frac{J_0(4\pi f_1\tau)J_0(4\pi f_2\tau)}{4NM} \\ &+ \frac{J_0(4\pi f_1\tau) + J_0(4\pi f_1\tau)J_0^2(2\pi f_2\tau)}{N} + \frac{J_0(4\pi f_2\tau) + J_0(4\pi f_2\tau)J_0^2(2\pi f_1\tau)}{M} + \frac{4\xi(f_1,\tau)\xi(f_2,\tau)}{N^2M^2} \\ &- \frac{4M\big(1 + J_0^2(2\pi f_2\tau)\big) + J_0(4\pi f_2\tau)}{N^2M}\xi(f_1,\tau) - \frac{4N\big(1 + J_0^2(2\pi f_1\tau)\big) + J_0(4\pi f_1\tau)}{NM^2}\xi(f_2,\tau) \end{aligned} \tag{2.3.5}$$

where J_0 is the zero-order Bessel function first kind, $\xi(f_1,\tau)=\sum_{n=1}^{N}\Big(\mathbb{E}\big[\cos\big(2\pi f_1\tau\cos(\alpha_n)\big)\big]\Big)^2$, and $\xi(f_2,\tau)=\sum_{m=1}^{M}\Big(\mathbb{E}\big[\cos\big(2\pi f_2\tau\cos(\beta_m)\big)\big]\Big)^2$. The expectation terms in (2.3.5) can be evaluated numerically. It is also worth noting that, although Model B has a different probability density distribution function than the double-ring model in [14], their autocorrelation and cross-correlation properties are the same.

The time-average correlations for Model B can be derived as

$$\tilde{R}_{g_cg_c}(\tau)=\lim_{T\to\infty}\frac{1}{T}\int_0^T g_c(t)g_c(t+\tau)dt=\frac{1}{2MN}\sum_{n,m=1}^{N,M}\big(\tilde{A}_n(\tau)\tilde{B}_m(\tau)+\tilde{C}_n(\tau)\tilde{D}_m(\tau)\big) \quad (2.3.6)$$

$$\tilde{R}_{g_cg_s}(\tau)=\lim_{T\to\infty}\frac{1}{T}\int_0^T g_c(t)g_s(t+\tau)dt=0 \quad (2.3.7)$$

$$\tilde{R}_{g_sg_c}(\tau)=\lim_{T\to\infty}\frac{1}{T}\int_0^T g_s(t)g_c(t+\tau)dt=0 \quad (2.3.8)$$

$$\tilde{R}_{g_sg_s}(\tau)=\lim_{T\to\infty}\frac{1}{T}\int_0^T g_s(t)g_s(t+\tau)dt=\frac{1}{2MN}\sum_{n,m=1}^{N,M}\big(\tilde{A}_n(\tau)\tilde{D}_m(\tau)+\tilde{C}_n(\tau)\tilde{B}_m(\tau)\big) \quad (2.3.9)$$

where $\tilde{A}_n(\tau)=\cos\big(2\pi f_1\tau\cos(\alpha_n)\big)$, $\tilde{B}_m(\tau)=\cos\big(2\pi f_2\tau\cos(\beta_m)\big)$, $\tilde{C}_n(\tau)=\cos\big(2\pi f_1\tau\sin(\alpha_n)\big)$, and $\tilde{D}_m(\tau)=\cos\big(2\pi f_2\tau\sin(\beta_m)\big)$. The variance of the time-average correlations for Model B can be derived as

$$\mathrm{Var}[\tilde{R}_{g_cg_s}(\tau)]=\mathbb{E}[\tilde{R}^2_{g_cg_s}(\tau)]-(R_{g_cg_s}(\tau))^2=0 \quad (2.3.10)$$

$$\mathrm{Var}[\tilde{R}_{g_sg_c}(\tau)]=\mathbb{E}[\tilde{R}^2_{g_sg_c}(\tau)]-(R_{g_sg_c}(\tau))^2=0 \quad (2.3.11)$$

$$\mathrm{Var}[\tilde{R}_{g_sg_s}(\tau)]=\mathbb{E}[\tilde{R}^2_{g_sg_s}(\tau)]-(R_{g_sg_s}(\tau))^2=\mathrm{Var}[\tilde{R}_{g_cg_c}(\tau)] \quad (2.3.12)$$

$$\begin{aligned}\mathrm{Var}[\tilde{R}_{g_cg_c}(\tau)]&=\mathbb{E}[\tilde{R}^2_{g_cg_c}(\tau)]-(R_{g_cg_c}(\tau))^2\\&=\frac{(1+J_0(4\pi f_1\tau))(1+J_0(4\pi f_2\tau))+2NJ_0^2(2\pi f_1\tau)(J_0(4\pi f_2\tau)+1)+2MJ_0^2(2\pi f_2\tau)(J_0(4\pi f_1\tau)+1)}{8NM}\\&+\frac{J_0^2(2\pi f_2\tau)}{2N^2}V_{\tilde{A}\tilde{C}}+\frac{J_0^2(2\pi f_1\tau)}{2M^2}V_{\tilde{B}\tilde{D}}+\frac{1}{2N^2M^2}\Big(V_{\tilde{A}\tilde{C}}V_{\tilde{B}\tilde{D}}+\xi(f_1,\tau)\xi(f_2,\tau)\Big)\\&-\frac{1+J_0(4\pi f_2\tau)+2MJ_0^2(2\pi f_2\tau)}{4N^2M}\xi(f_1,\tau)-\frac{1+J_0(4\pi f_1\tau)+2NJ_0^2(2\pi f_1\tau)}{4NM^2}\xi(f_2,\tau)\end{aligned} \quad (2.3.13)$$

where $V_{\tilde{A}\tilde{C}}=\sum_{n=1}^{N}\big(\mathbb{E}[\tilde{A}_n(\tau)\tilde{C}_n(\tau)]-\mathbb{E}[\tilde{A}_n(\tau)]\mathbb{E}[\tilde{C}_n(\tau)]\big)$ and $V_{\tilde{B}\tilde{D}}=\sum_{m=1}^{M}\big(\mathbb{E}[\tilde{B}_m(\tau)\tilde{D}_m(\tau)]-$

$\mathbb{E}[\tilde{B}_m(\tau)]\mathbb{E}[\tilde{D}_m(\tau)]\big)$.

2.3.2 Second-order statistics for Model D

Autocorrelation, cross-correlation, autocorrelation of the complex envelopes, and autocorrelation of the squared envelope for Model D are given below. Steps for the proof are presented in Appendix B.

$$R_{h_ch_c}(\tau) = \mathbb{E}\big[h_c(t+\tau)h_c(t)\big] = \frac{J_0(2\pi f_1\tau)J_0(2\pi f_2\tau) + K\cos\big(2\pi f_3\tau\cos(\phi_3)\big)}{2(1+K)} \tag{2.3.14}$$

$$R_{h_ch_s}(\tau) = \mathbb{E}\big[h_c(t+\tau)h_s(t)\big] = -\frac{K\sin\big(2\pi f_3\tau\cos(\phi_3)\big)}{2(1+K)} \tag{2.3.15}$$

$$R_{h_sh_s}(\tau) = \mathbb{E}\big[h_s(t+\tau)h_s(t)\big] = R_{h_ch_c}(\tau) \tag{2.3.16}$$

$$R_{h_sh_c}(\tau) = \mathbb{E}\big[h_s(t+\tau)h_c(t)\big] = -R_{h_ch_s}(\tau) \tag{2.3.17}$$

$$\begin{aligned} R_{hh}(\tau) &= \frac{1}{2}\mathbb{E}\big[h(t+\tau)h^*(t)\big] = \frac{1}{2}\big(R_{h_ch_c}(\tau) + R_{h_sh_s}(\tau) - jR_{h_ch_s}(\tau) + jR_{h_sh_c}(\tau)\big) \\ &= \frac{J_0(2\pi f_1\tau)J_0(2\pi f_2\tau) + Ke^{j2\pi f_3\tau\cos(\phi_3)}}{1+K} \end{aligned} \tag{2.3.18}$$

$$R_{|h|^2|h|^2}(\tau) = \mathbb{E}\big[h_c^2(t)h_c^2(\varrho) + h_s^2(t)h_c^2(\varrho) + h_c^2(t)h_s^2(\varrho) + h_s^2(t)h_s^2(\varrho)\big] \tag{2.3.19}$$

$$= \frac{R_{|g|^2|g|^2}(\tau) + 8KR_{g_cg_c}(\tau)\cos\big(2\pi f_3\tau\cos(\phi_3)\big) + 8K + 4K^2}{4(1+K)^2} \tag{2.3.20}$$

For sufficient N and M, the expression of (2.3.20) can be simplified as

$$\begin{aligned} R_{|h|^2|h|^2}(\tau) = \frac{1}{(1+K)^2}\Big(&1 + J_0^2(2\pi f_1\tau) + J_0^2(2\pi f_2\tau) + J_0^2(2\pi f_1\tau)J_0^2(2\pi f_2\tau) \\ &+ 2K\big(1 + J_0(2\pi f_1\tau)J_0(2\pi f_2\tau)\cos(2\pi f_3\tau\cos(\phi_3))\big) + K^2\Big). \end{aligned} \tag{2.3.21}$$

The time-average correlations for Model D can be expressed as

$$\tilde{R}_{h_ch_c}(\tau) = \frac{\tilde{R}_{g_cg_c}(\tau) + K\cos\big(2\pi f_3\tau\cos(\phi_3)\big)}{2(1+K)} \tag{2.3.22}$$

$$\tilde{R}_{h_c h_s}(\tau) = \tilde{R}_{h_s h_c}(\tau) = \frac{K \sin\left(2\pi f_3 \tau \cos(\phi_3)\right)}{2(1+K)} \tag{2.3.23}$$

$$\tilde{R}_{h_s h_s}(\tau) = \frac{\tilde{R}_{g_s g_s}(\tau) + K \cos\left(2\pi f_3 \tau \cos(\phi_3)\right)}{2(1+K)}. \tag{2.3.24}$$

The variance of the time-average correlations for Model D can be derived as

$$\mathrm{Var}[\tilde{R}_{h_c h_c}(\tau)] = \mathbb{E}[\tilde{R}^2_{h_c h_c}(\tau)] - (R_{h_c h_c}(\tau))^2 = \frac{\mathrm{Var}[\tilde{R}_{g_c g_c}(\tau)]}{4(1+K)^2} \tag{2.3.25}$$

$$\mathrm{Var}[\tilde{R}_{h_s h_s}(\tau)] = \mathbb{E}[\tilde{R}^2_{h_s h_s}(\tau)] - (R_{h_s h_s}(\tau))^2 = \frac{\mathrm{Var}[\tilde{R}_{g_s g_s}(\tau)]}{4(1+K)^2} \tag{2.3.26}$$

$$\mathrm{Var}[\tilde{R}_{h_c h_s}(\tau)] = \mathbb{E}[\tilde{R}^2_{h_c h_s}(\tau)] - (R_{h_c h_s}(\tau))^2 = 0 \tag{2.3.27}$$

$$\mathrm{Var}[\tilde{R}_{h_s h_c}(\tau)] = \mathbb{E}[\tilde{R}^2_{h_s h_c}(\tau)] - (R_{h_s h_c}(\tau))^2 = 0 \tag{2.3.28}$$

2.4 Simulations Results

In this section, we present extensive Monte Carlo simulation results on the statistical properties of the proposed models. The simulation results are obtained using $N_s = 10^6$ samples in a 10s time duration with sampling period $T_s = 10^{-5}s$. The frequencies in all models are $f_1 = f_2 = 100Hz$, $P = Q = 16$ in Models A and C, $M = N = 16$ in Models B and D, and $\phi_1 = \phi_{12} = \frac{\pi}{2}$ in Models C and D. All plots are obtained using one trial unless stated otherwise. We also simulate the double-ring [14] and fixed-to-mobile channel models [16, 18, 58] to demonstrate the difference in statistical behavior of cascaded Rayleigh fading and single Rayleigh fading distributions,

2.4.1 Probability density functions for channel envelopes

The distribution of channel envelopes for cascaded Rayleigh channels without and with LOS has been discussed in [23, 59, 60]. Recognizing that the average power for models A and B is one, the probability density function (PDF), the cumulative density function (CDF)

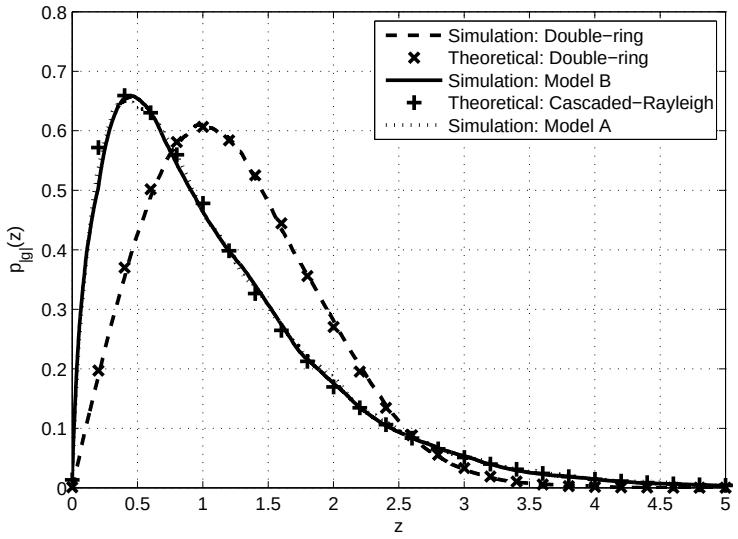

Figure 2.1: PDF for Models A and B.

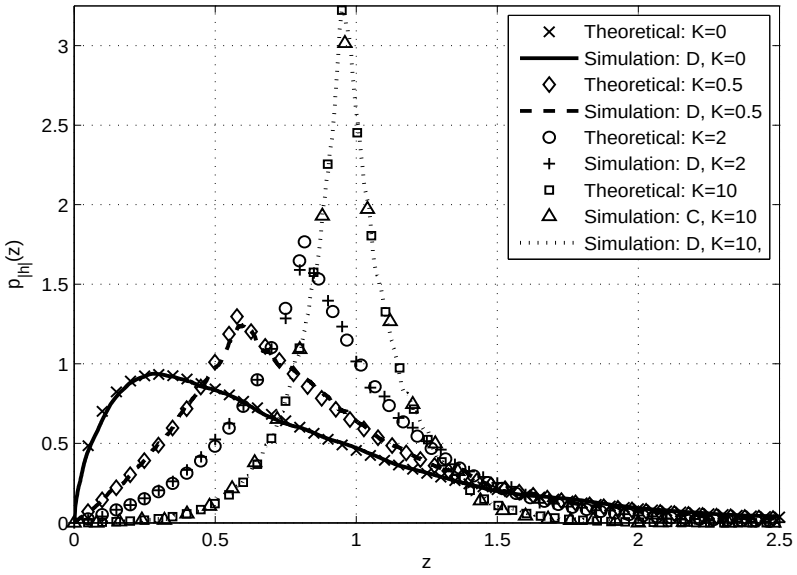

Figure 2.2: PDF for Models C and D.

of the envelopes of Models A and B are given, respectively, by (major steps are provided in the Appendix G for convenience of readers): $p_Z(z) = 2zK_0\big(z\sqrt{2}\big)$, and $P_Z(Z \leq z) = 1-\sqrt{2}zK_1\big(z\sqrt{2}\big)$, where z represents the envelope of Models A and B, i.e., $|g(t)|$, K_0 and K_1 are, respectively, the zero-order and first-order second kind modified Bessel function. Using (12) in [60] with $\sigma_i = \frac{1}{\sqrt{2\sqrt{1+K}}}$, for $i = 1, 2$, the PDF for the envelope of Models C and D is given by

$$p_Z(z) = \begin{cases} 4(1+K)zI_0\big(2\sqrt{1+K}z\big)K_0\big(2\sqrt{K}\big), & \text{for } z < \frac{\sqrt{K}}{\sqrt{1+K}} \\ 4(1+K)zI_0\big(2\sqrt{K}\big)K_0\big(2\sqrt{1+K}z\big), & \text{for } z \geq \frac{\sqrt{K}}{\sqrt{1+K}} \end{cases} \tag{2.4.1}$$

where $z = |h|$, I_0 is the zero-order first kind modified Bessel function.

Fig. 2.1 shows the simulation of the PDF of envelopes for Models A and B. The plots indicate that distributions of envelopes of both models match the theoretical curves very well. For comparison, simulations of the PDF for the double-ring M-M mobile channel model [14] is plotted. While the envelope of the double-ring model follows Rayleigh distribution, Models A and B follow cascaded Rayleigh (worse than Rayleigh) distribution.

Fig. 2.2 shows the simulation of the PDF of envelopes for Models C and D with different values of K. For the special case $K = 0$, Models C and D becomes, respectively, Models A and B up to a factor of $\sqrt{2}$. This figure shows that the distribution of envelopes of both models match the theoretical curves in (2.4.1) for all values of K.

2.4.2 Second-order statistics

Autocorrelation and cross-correlation of Model B. The autocorrelation of Model B is shown in Fig. 2.3 using one and three trials. This figure suggests that Model B converges to the theoretical autocorrelation in one trial, and the difference between the simulation and the

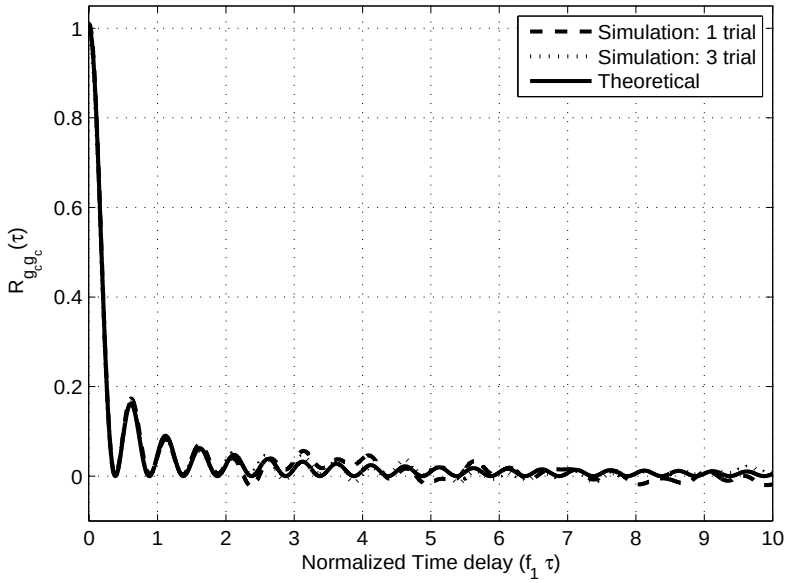

Figure 2.3: Autocorrelation for Model B.

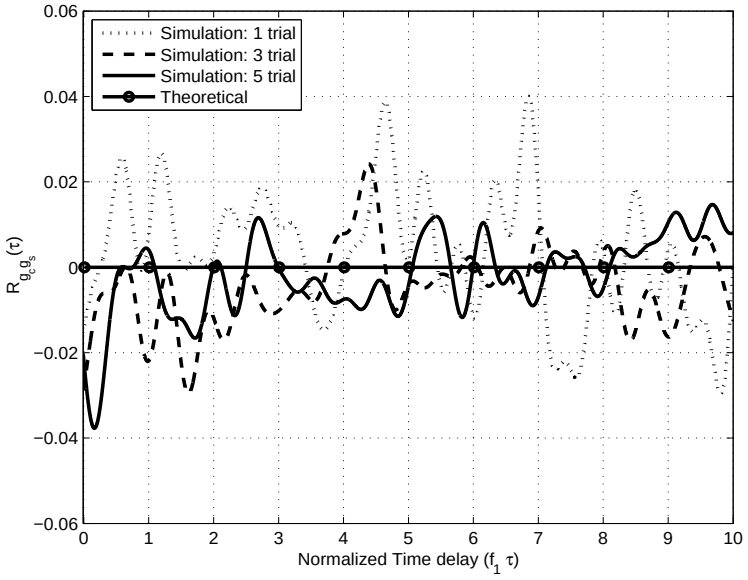

Figure 2.4: Cross-correlation for Model B.

theoretical (2.3.1) is smaller in three trials. The cross-correlation is shown in Fig. 2.4 using one, three, and five trials. While simulated cross-correlation using one trial converges to the theoretical (2.3.3) expression reasonably well, the simulated cross-correlation converges to the theoretical expression more closely when more trials are used.

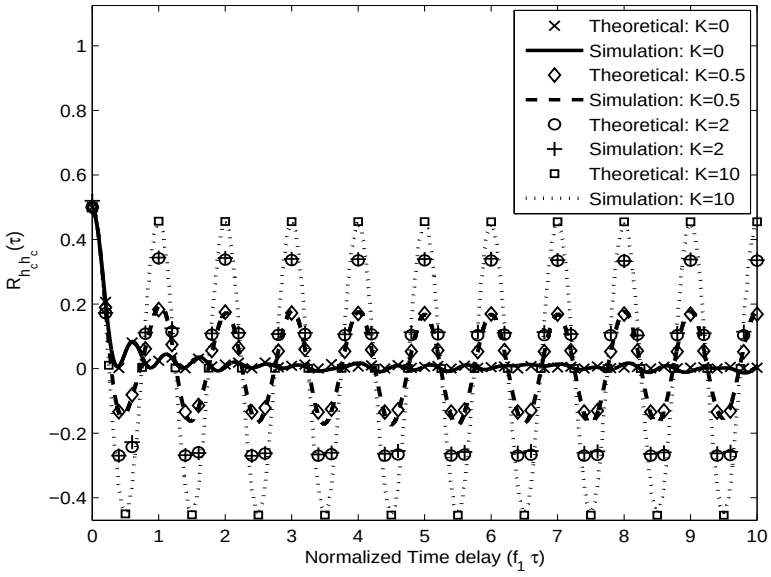

Figure 2.5: Autocorrelation for Model D.

Autocorrelation and cross-correlation of Model D. The autocorrelation of Model D with different values of K is shown in Fig. 2.5. These plots indicate that the simulated autocorrelation converges to the theoretical expression very well in one trial. It can also be observed that the LOS component dominates the autocorrelation as τ increases. This is because the Bessel function approaches zero when τ is large, and the autocorrelation thus approaches $K\cos\big(2\pi f_3\cos(\phi_3)\big)\big(2(1+K)\big)^{-1}$. The cross-correlation for various values of K is shown in Fig. 2.6. Again, the plots indicate that the simulation results converge to theoretical expressions in (2.3.14) and (2.3.17) in one trial.

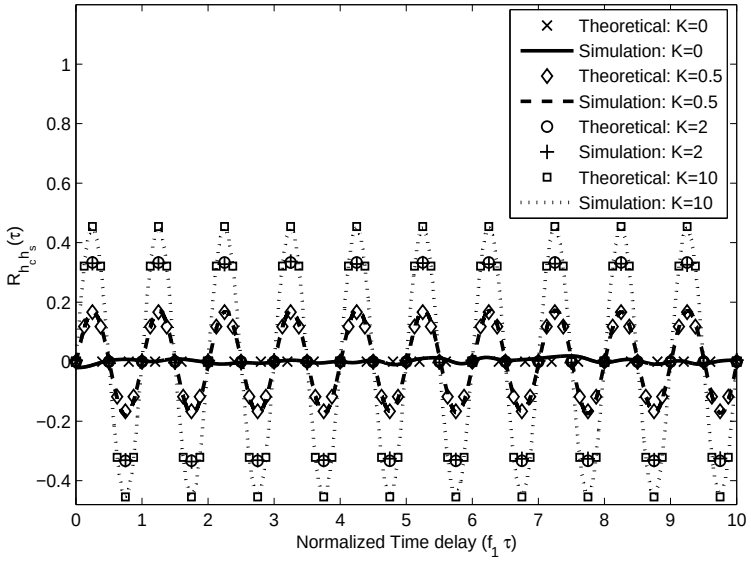

Figure 2.6: Cross-correlation for Model D.

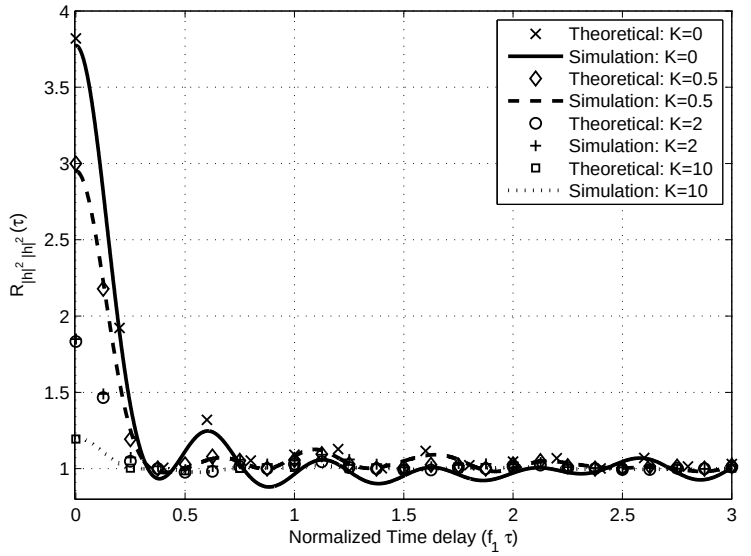

Figure 2.7: Autocorrelation for square envelope for Model D

Fig. 2.7 plots the autocorrelation of the squared envelope for different values of K. The simulated results converges to its theoretical in (2.3.20) in one trial. The plots suggests that the autocorrelation of the squared envelope approaches 1 when τ is large, regardless of K. As $\tau \to \infty$, all Bessel terms in (2.3.20) become zero, which results in $R_{|h|^2|h|^2}(\tau) = \frac{K^2+2K+1}{(1+K)^2} = 1$.

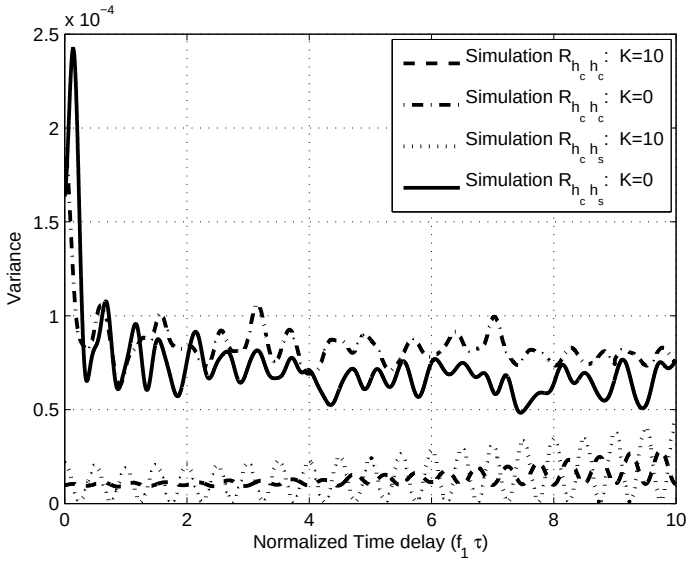

Figure 2.8: Variance of auto- and cross-correlation for Model D

Variance of the time-average correlations for Model D. The variance of time-average autocorrelation and cross-correlation for Model D with $K = 0$ and 10 are obtained by averaging 200 samples for each τ. As shown in Fig. 2.8, the variance time-average autocorrelation and cross-correlation are, respectively, in the magnitudes of 10^{-4} or 10^{-5}. Since the plot for $K = 0$ reflects a variance of the time-average correlations for Model B up to a factor of 2, the small variance in the figure confirms that all proposed models have satisfactory convergence performance.

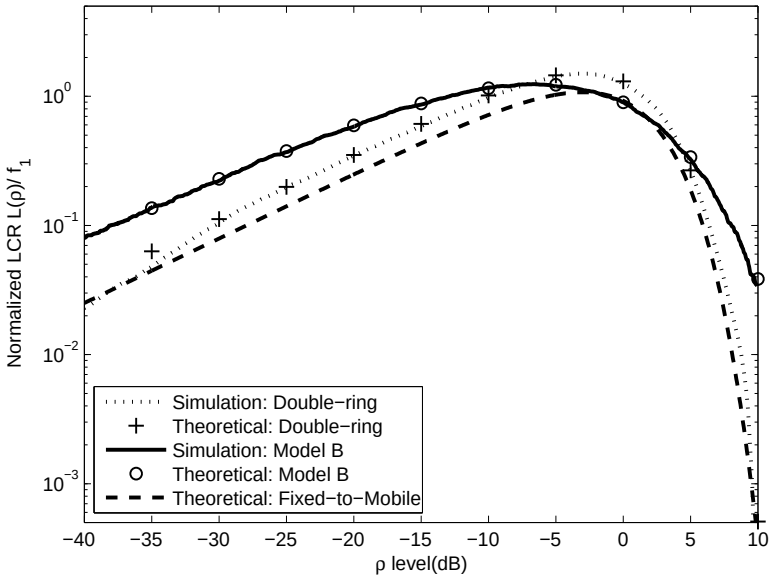

Figure 2.9: Normalized LCR for Model B.

2.4.3 Higher-order statistics: LCR and AFD

The level crossing rate and the average fade duration are two important statistical properties related to channel dynamics. At a specified level R, the LCR for a channel envelope is the rate (in crossings per second) at which the channel envelope crosses in the positive (or negative) direction [13, 36, 58]. The AFD is the average time duration that the envelope remains below the level R [36, 58]. Approximations for LCR and AFD are plotted in [52, 61] for the cascaded Rayleigh fading channels. Here, we present plots by numerical evaluation of the exact LCR and AFD functions.

LCR for Model B. The LCR for the cascaded Rayleigh channel without LOS has the following form [60, 62]:

$$L_{|g|}(R) = \left(2\pi\sqrt{2}\right)^{\frac{1}{2}} R f_1 \int_0^\infty x^{-2}\sqrt{a^2R^2 + x^4}\; e^{-\frac{R^2+x^4}{\sqrt{2}x^2}}\, dx \tag{2.4.2}$$

where $a = \frac{f_2}{f_1}$, and R is the level. In the simulations of LCRs, the normalized LCRs and

normalized signal level are used [12–14, 58]. For model B, the normalized LCRs is $L_{|g|}f_1^{-1}$, and normalized signal level is defined as $\rho = \frac{R}{\sqrt{\mathcal{P}}}$, where $\sqrt{\mathcal{P}}$ is the root mean square (rms) envelope level for the channel, and $\mathcal{P} = 2$. As shown in Fig. 2.9, the simulated LCR matches well with the theoretical (2.4.2). For comparison, we also simulated the LCR for a fixed-to-mobile channel [16]. It can be observed that, for given signal levels, the LCR for Model B is more likely higher than that for fixed-to-mobile and double-ring models. This can be explained by the higher dynamics of the statistical properties in cascaded Rayleigh fading than a single Rayleigh fading distribution.

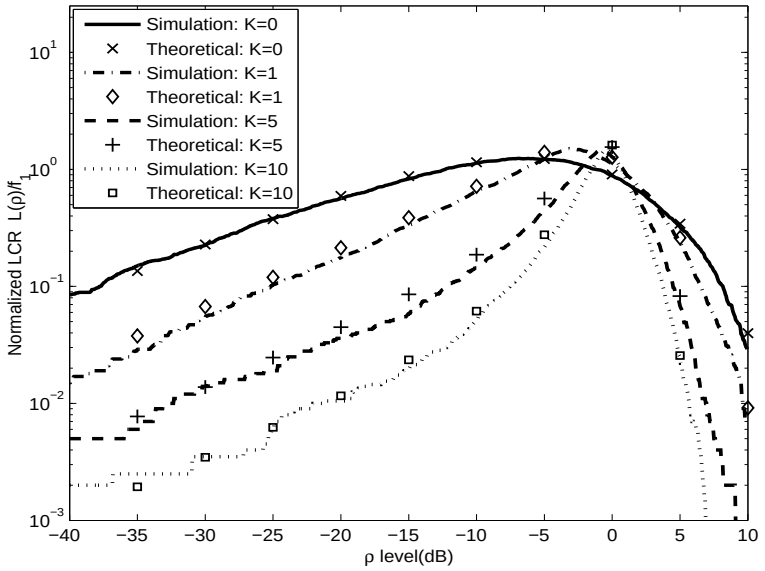

Figure 2.10: Normalized LCR for Model D.

LCR for Model D. The LCR for Model D is expressed as [60, 62]:

$$L_{|h|}(R) = \big(1+K\big)^{\frac{3}{4}} R f_1 \int_0^{\infty}\int_{-\pi}^{\pi} x^{-2}\sqrt{a^2 y_1(R,\vartheta)+x^4} \times \left(y_2(R,\vartheta,x)\Big(1+\mathrm{erf}\Big(\frac{y_2(R,\vartheta,x)}{\sqrt{2}}\Big)\Big)+\sqrt{\frac{2}{\pi}}e^{-\frac{y_2^2(R,\vartheta,x)}{2}}\right) e^{-\sqrt{1+K}(x^2+\frac{y_1(R,\vartheta)}{x^2})} d\vartheta dx \tag{2.4.3}$$

where erf$(\cdot)$ is the error function [63], and $y_1(R,\vartheta)$ and $y_2(R,\vartheta,x)$ are defined, respectively, as

$$y_1(R,\vartheta) = R^2 + \frac{K}{1+K} - \frac{2R\sqrt{K}\cos(\vartheta)}{\sqrt{1+K}} \tag{2.4.4}$$

$$y_2(R,\vartheta,x) = \frac{2xf_3\sqrt{K}\sin(\vartheta)}{f_1\sqrt{\sqrt{1+K}}\sqrt{a^2y_1(R,\vartheta)+x^4}}. \tag{2.4.5}$$

The LCRs of Model D with different values of K are shown in Fig. 2.10. The normalized signal level is $\rho = R$, since the rms envelope level for Model D is one. While the plots indicate a good match between the simulated LCRs and the theoretical expression in (2.4.3), it is also observed that the higher the K, the lower the observed LCRs.

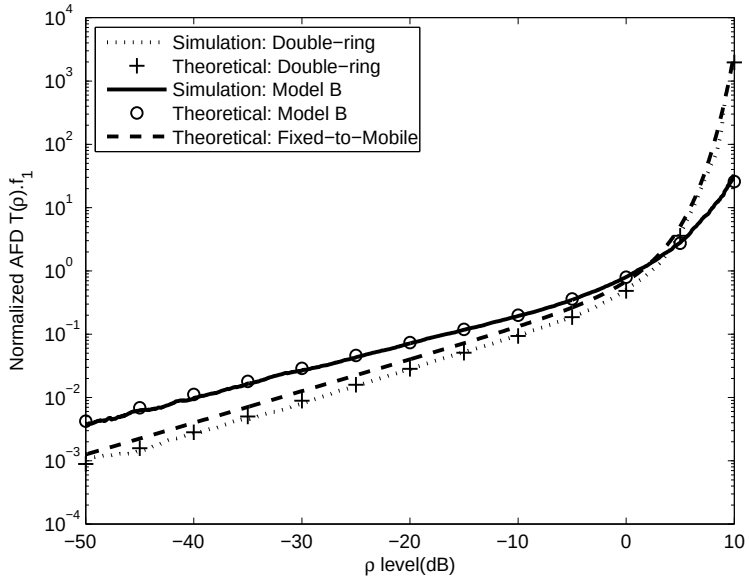

Figure 2.11: Normalized AFD for Model B.

AFD for Model B. Using (2.4.2) and the CDF for $|g|$, the AFD for Model B can be obtained as [36]:

$$T_{|g|}(R) = \frac{P_Z(z \le R)}{L_{|g|}(R)} = \left(1-\sqrt{2}RK_1\left(R\sqrt{2}\right)\right)\left(f_1R\sqrt{2\pi\sqrt{2}}\int_0^\infty x^{-2}\sqrt{a^2R^2+x^4}e^{-\frac{R^2+x^4}{\sqrt{2}x^2}}dx\right)^{-1} \tag{2.4.6}$$

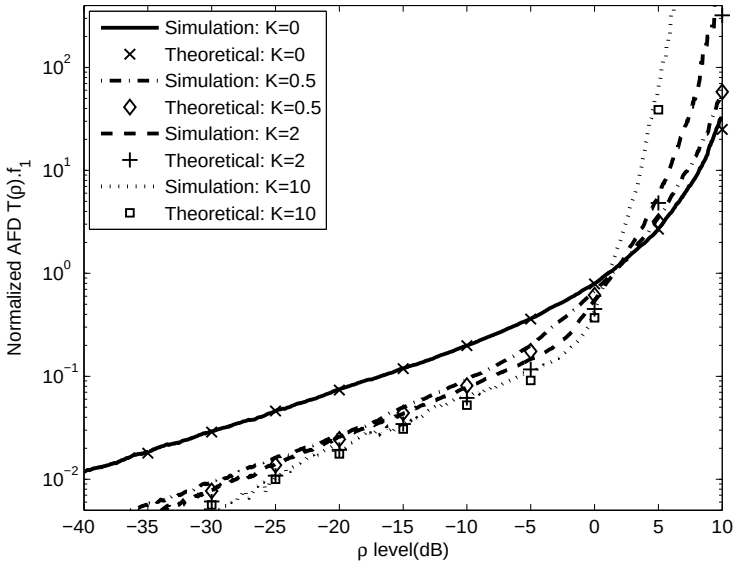

Figure 2.12: Normalized AFD for Model D.

In the simulations, normalized AFD [12–14, 16, 58] is plotted. For Model B, the normalized AFD is $T_{|h|}f_1$. The plots in Fig. 2.11 shows agreement between the simulated AFD with the theoretical (2.4.6). For lower level of signals ($\rho < 0$ dB), the AFD of Model B is longer than the AFDs of fixed-to-mobile and double-ring models; and for higher level of signals ($\rho > 0$ dB), the AFD of Model B is shorter than those of fixed-to-mobile and double-ring models. This indicates that cascaded Rayleigh fading is more severe fading than a single Rayleigh fading.

AFD for Model D. The AFD can be calculated as $T_{|h|}(R) = \frac{P_Z(z \le R)}{L_{|h|}(R)}$, where $L_{|h|}(R)$ is given in (2.4.3), and the CDF of the envelope $z = |h|$ is given by

$$P_Z(Z \le z) = \begin{cases} 2\sqrt{1+K}\,z I_1\big(2\sqrt{1+K}z\big)K_0\big(2\sqrt{K}\big), & \text{for } z < \frac{\sqrt{K}}{\sqrt{1+K}} \\ 1 - 2\sqrt{1+K}\,z I_0\big(2\sqrt{K}\big)K_1\big(2\sqrt{1+K}z\big), & \text{for } z \ge \frac{\sqrt{K}}{\sqrt{1+K}} \end{cases} \tag{2.4.7}$$

where I_0 and I_1 are the modified Bessel function first kind, zero-order and first-order, respectively. Fig. 2.12 shows the AFD for Model D. For lower level of signals ($\rho < 0$ dB), the

value of AFD decreases when the values of K increase (stronger component of LOS), and for higher level of signals ($\rho > 0$ dB), the value of AFD decreases when the values of K decrease (weaker component of LOS).

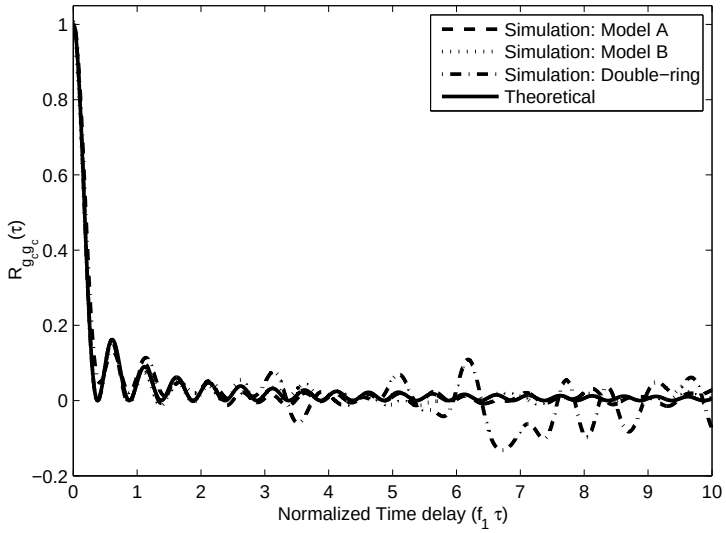

Figure 2.13: Autocorrelation for Models A, B, and double-ring

2.4.4 Complexity analysis

In this section, we examine the complexity of our proposed channel models. Since models are sparse for M-M cascaded Rayleigh fading channels in the literature, we compare Models A and B with the double-ring simulation model, one of the well-known models for M-M Rayleigh fading channels. It is worth to mention that double-ring and the proposed models are for different categories of M-M channels, the comparison is solely for the illustration of complexity and performance of the proposed models. The number of additions required for Models A and B to generate one channel sample are, respectively, $2(P+Q)$ and $2(M+N)$, and $2MN$ additions are required for the double-ring model (same notations (M and N) are

used in [14]). Besides additions, one multiplication is required for both Models A and B, and no multiplication is required for the double-ring model. Table 2.1 lists the averaged CPU time elapsed when generating one channel sample for Models A, B, and double-ring. A HP Compaq 8510p computer, Intel (R) Core (TM) 2 Duo CPU T7500 @ 2.20GHz, is used with $M = N = P = Q = 8$ for all models. It can be seen that the elapsed time to generate one sample for Models A and B is much shorter than that for the double-ring model. A relative CPU time is also listed, with T_D being the referenced time for the double-ring model.

TABLE 2.1:

CPU TIME ELAPSED FOR ONE CHANNEL SAMPLE

Model	Computations for one channel sample	CPU time	Relative CPU time
Model A	$2(Q+P)$ additions, 1 multiplication	3.8s	0.2 T_D
Model B	$2(M+N)$ additions, 1 multiplication	4.3s	0.23 T_D
Double-Ring	$2MN$ additions	18.8s	T_D

To investigate the performance of convergence, we examine the mean square error (MSE) between simulated autocorrelation and the theoretical for Models A, B, and double-ring model. These models have an identical theoretical autocorrelation expression (2.3.1). The MSEs are obtained using one trial for different complexity levels. As shown in the first four rows in Table 2.2, if the same number of additions are used to generate one channel sample, then both Models A and B have much better convergence performance with significantly smaller MSE than the double-ring model, and Model B provides the best convergence performance. If the same number of sinusoids are used (in this case, Models A and B have much

less complexity), the convergence performance of Models A and B is still comparable to that of the double-ring model.

Fig. 2.13 plots the autocorrelations of Models A, B, and double-ring model for the scenario listed in the second row of Table 2.2, whereby the number of additions to generate one channel sample is 200 for all models. The plots indicate that Model B has a faster convergence rate than the double-ring model.

TABLE 2.2:

MSE AND COMPLEXITY

Additions for One Channel Sample	Model A	Model B	Double-Ring
128	5.34×10^{-4} $\{Q = P = 32\}$	2.12×10^{-4} $\{M = N = 32\}$	8.1×10^{-3} $\{M = N = 8\}$
200	3.19×10^{-4} $\{Q = P = 50\}$	1.80×10^{-4} $\{M = N = 50\}$	4.69×10^{-3} $\{M = N = 10\}$
288	1.92×10^{-4} $\{Q = P = 72\}$	1.64×10^{-4} $\{M = N = 72\}$	2.91×10^{-3} $\{M = N = 12\}$
392	1.78×10^{-4} $\{Q = P = 98\}$	1.28×10^{-4} $\{M = N = 98\}$	2.40×10^{-3} $\{M = N = 14\}$
32: Models A and B 128: Double-Ring	7.3×10^{-3} $\{Q = P = 8\}$	2.8×10^{-3} $\{M = N = 8\}$	8.1×10^{-3} $\{M = N = 8\}$

2.5 Summary

We have proposed statistical models for mobile-to-mobile channels, whereby the received signals experience cascaded Rayleigh fading with or without LOS. The models contain two

individual summations and are therefore easy to implement with lower complexity. Furthermore, the models provide faster convergence to all the desired statistical properties, including the pdf, autocorrelations, LCRs, and AFDs. Theoretical derivation of the time-averaged statistical properties and the corresponding variance are derived to confirm that the proposed models have good convergence performance. Extensive Monte Carlo simulation results on various statistical properties and complexity analysis are provided to validate the proposed models. While measurements and tests in various highly dense scattering environments confirm that the M-M channels may undergo cascaded Rayleigh fading (more severe than single Rayleigh fading), our proposed models can be used to simulate the underlying channels and reveal the corresponding statical properties.

CHAPTER 3

M2M CHANNEL MEASUREMENTS IN SUBURBAN ENVIRONMENTS

3.1 Literature Review

In mobile ad hoc wireless networks and intelligence transportation systems, the nodes or terminals are no longer stationary [1–6]. Accurate mobile-to-mobile (M2M) channel modeling is highly desirable not only for analysis and designs of these systems, but also beneficial to conventional cellular base station infrastructures. A series of mobile-to-mobile hops are found helpful to extend the coverage and reduce power consumption in cellular base stations [7]. The channels in the M2M hops are different from those in cellular communication systems, since the Tx and Rx are both in motion, in addition, the antennas at the Tx and Rx are closer to ground levels. Small-scale M2M channel models are studied for isotropic and non-isotropic scattering in Rayleigh, cascaded-Rayleigh, and Rician fading [14, 17, 24, 50–52, 56, 64–66]. Intensive measurements for vehicle-to-vehicle (V2V) channels are conducted in various highway, suburban, rural roads, and some application-specific scenarios such as traffic congestion at 5GHz and 700MHz, e.g. [20–22, 24, 29–32, 34, 35, 67]. The path loss, power-delay profiles, and delay-doppler spectra have been analyzed [20–22, 30–32, 34, 35, 67]. The two-ray model [33], which was originally proposed for cellular communications, is suggested to represent the path loss in rural V2V channels [34] and confirmed by the measurements with a LOS environment [35]. Weibull distribution is verified for small-scale fading in urban V2V channels by the measurements in [29, 57].

In most V2V channel measurements, transmitter and/or receiver antennas are usually placed on the roof of test vehicles. However, in many application of M2M communications,

the mobile units (and their antennas) are often inside a vehicle traveling on roads; or inside a pocket or bag carried by a pedestrian walking at side roads, parking lots, or woody/forest areas. Available channel measurements and modelings for these types of M2M channels are found limited, although the vehicle penetration loss for antennas inside a vehicle is studied by measurements in $100 \sim 2400$MHz [68–70]. Small-scale fading is studied via measurements for outdoor and indoor walking M2M channels [23, 25, 28].

A double-Rayleigh or cascaded Rayleigh distribution is found for the outdoor-to-indoor vehicle-to-walk channels [23]. A similar observation is found in the outdoor walk-to-walk channel measurements in a downtown (New York) area without LOS, where the Tx moves within a circle of one meter (m) radius and Rx are randomly placed within a 10 m $\times$ 10 m square [25]. A walk-to-walk M2M channel measurement is conducted in a forest area, where a Weibull distribution is suggested for the small-scale fading of the channel [28]. Characterization of the channels in forest areas may play critical roles in emergency rescues [28]. While empirical path loss models are obtained for fixed-to-fixed (F2F) channels in foliage areas [29, 37–40], channel measurements and models for M2M channels in woody or forest areas seem not many in literature.

In this paper, we conduct measurements for the M2M channels in suburban area with dense scattering environments at 1.85 GHz frequency band, and explore the channel models for large scale and small-scale fading. Suburban areas usually include streets with one or two lanes in each traffic direction, and buildings or houses set back from the curb; while urban areas have wider streets with buildings or houses closer to the curb [34]. Depending on the tests routes and areas, the Tx and Rx travel towards or away from each other in an angle (e.g. perpendicularly), or in convoy and opposite directions as in many V2V

measurements (e.g. [20–22, 24, 29–32, 35, 67]). Different antenna placements are considered: a). inside-vehicle-to-inside-vehicle (IV2IV) where the antennas of both Tx and Rx are placed inside the test vehicles; b). inside-vehicle-to-walk (IV2W) where the antenna of Tx is inside the vehicle and antenna of Rx is placed inside the pocket or next to the head at a walking speed; c). walk-to-walk (IV2W) where the antenna of Tx is placed on a cart and antenna of Rx is also placed inside the pocket or next to the head at a walking speed.

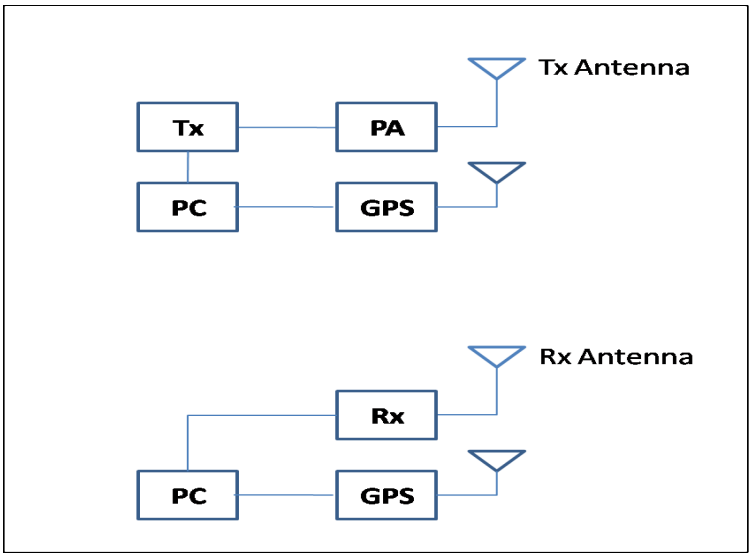

Figure 3.1: Setup diagram for the Tx and Rx.

3.2 Measurements Setup

The channel measurements were conducted in northern Kansas in November 2013 when the trees were in their final growth, while grass was still in full growth. Test area was chosen in a suburban area with a mix of trees, story buildings, street signs and corners, where heavy diffracting and dense scattering to radio signals were likely to occur [33]. The areas were scanned while the Tx was turned off before conducting the tests. A low received power at

−140dB was recorded at the testing frequency, 1850MHz, to ensure that the selected radio frequency was not used by other carriers. The receiver was configured to 100kHz narrow bandwidth with −151dB sensitivity/collection threshold. The measurements were collected using test vehicles and a mobile cart. Laptop computers were used to log the data. A Global Position System (GPS) was connected to the laptop to record the location, elevation, and speed. One GPS is used for the Tx and another was used at the Rx. To maintain reasonable resolutions for the measurements, tests were halted whenever the received signal approached low levels such as −150dB, and then resumed in the same areas to collect more data samples.

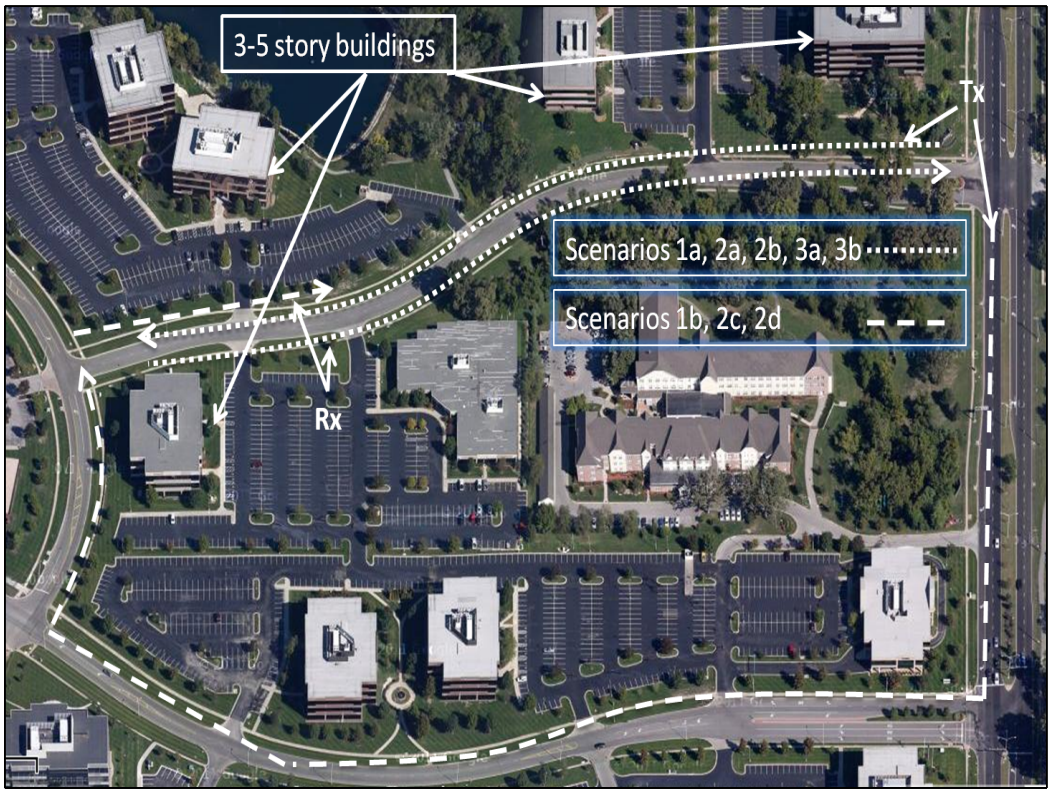

Figure 3.2: Test area in a suburban area

The Consultix WTX-35 Test Tx at -20dB transmitting power with a 22dB power amplifier (PA), and modified version of Consultix MRX-34 CW Rx were used in testings. A transmitted power of -25dB was used in case of Walk-to-Walk scenario. The Tx and Rx were equipped with omni antenna 0dBi gain, and the Tx was powered by 12v power supply, which was provided by either the internal batteries or externally from the power outlet in the test vehicle. The Rx was powered by USB connection from the logging PC which was also powered by internal battery or externally from the power outlet in the test vehicle. The Consultix Rx was connected to the computer by a USB port, and the data was recorded at rate of 1000 sample/sec. This rate allows to capture a max doppler of 5kHz and support speed up to 1.8×10^3 Mile/hr. The PA was powered by 12v AND 1Amp using a power inverter that was either connected to the car power outlet or a car battery in the Walk-to-Walk tests. Fig. 3.1 illustrates the equipment setup for these tests.

3.3 Test Scenarios

The test areas were in suburb streets shown in Fig. 3.2. Although suburban areas are determined by the geography of the land, trees, existing building in the area the visibility from the Tx to Rx are not always guaranteed. Three scenarios are characterized by Antenna location (inside or outside the vehicle.

Scenario 1 - IV2IV Suburban

In this scenario, both the Tx and Rx antennas were vertically placed inside the test vehicles at heights of 1m above the ground level. The Tx and Rx traveled at speed $10 \sim 30$ miles/hr with a separation distance $10 \sim 450$m between them.

We collected two sets of measurements: visibility existed and not existed, in order to obtain more accurate channel models. It is noticed that measurement data can also be collected and categorized by other criterions, such as different vehicle traveling directions [32, 35].

Scenario 1a - Without LOS The test streets are shown in Fig. 3.2. The Tx and Rx routes are shown in dashed lines. The Tx traveled in a two-way suburb street with one-lane in each direction at street speed $10 \sim 20$ miles/hr. While the Rx was driving in a U shape route at $10 \sim 30$ miles/hr speeds. Groups of two- or three-story or more buildings were found $20 \sim 40$m away from the curbs. Trees, bushes, and grass were on sides of the streets. The LOS between the Tx and Rx did not exist most the time. 110000 samples were collected for Scenario 1a.

Scenario 1b - With LOS The test route was configured as shown in Fig. 3.2 by dotted lines. The Tx traveled at a the local street at street speed along with the traffic and the Rx approached the Tx then moved away after passing in the same street at speed $10 \sim 20$ miles/hr. The Tx and Rx traveled in opposite direction with a separation $10 \sim 460$m, and there was visibility between them most time except after cross points when back of vehicle obstruct it. Around 164000 samples were collected for Scenario 1b.

Scenario 2 - IV2W Suburban

Similarly to Scenario 1, the Tx was inside the test vehicle with antenna 1m above the ground level. The Rx on the other hand was carried and the antenna was placed inside the pocket at 1m above ground or next to the face at height of 1.5m. The test area is the same as for

Scenario 1 are shown in Fig. 3.2.

Scenario 2a - Without LOS - Rx inside pocket As shown in Fig. 3.2. The Tx and Rx routes are shown in dashed lines. The Tx this time in contrast to scenario 1a, traveled at $20 \sim 35$ miles/hr in the streets marked by dashed U shape lines, and the Rx was moving in the local street at pedestrian speed at $2 \sim 3$ miles/hr in the side walks marked by dashed line. The separation between Tx and Rx was $20 \sim 500$m. Around 320000 samples were collected for this scenario. The LOS between the Tx and Rx did not exist for most of samples collected, excepts for those when the LOS was not blocked or partially blocked by the buildings, and the trees.

Scenario 2b - Without LOS - Rx Next to face In this scenarios, the same setup, conditions, and routes of Scenario 2a were used in this scenario as shown in Fig. 3.2. The only difference is the antenna of the Rx was placed next to the face at height of 1.5m. Around 200000 samples were collected for this scenario.

Scenario 2c - With LOS - Rx inside pocket Measurements in this scenario were collect in the local street as shown in dotted lines as shown in Fig. 3.2. Similarly to Scenario 1b, The Tx vehicle was moving on the local street at $10 \sim 25$ miles/hr. While the Rx was inside the pocked at height 1m and moved at pedestrian speed on the side walk marked by dotted line. There was visibility all the time even after crossing the Tx. Around 230000 samples were collected for this scenario.

Scenario 2d - With LOS - Rx Next to face In this scenario, the Rx antenna was placed next to the face at height of 1.5m while moving in the same route of Rx in Scenario 2c. The Tx traveled at same speed and same driving condition of Scenario 2c as showing in Fig. 3.2. The visibility from the Tx to Rx was guaranteed in most of the measurements collected. A total of 335000 samples were collect in this scenario.

Scenario 3 - W2W Suburban

The Tx was placed on a cart and pushed at pedestrian speed on the side walk. The Tx antenna was at height 1m above the ground. The Tx and its PA were powered by car battery using power inverter. The heights of the Rx were again 1m and 1.5m above the ground. As shown in Fig. 3.2, the Tx traveled on the side walk next to the two-way suburb street marked by dotted line approaching the Rx which was on the same side of the side walk. The separation between Tx and Rx was $10 \sim 450$m, and the visibility between them was partly obstructed by trees, bushes.

Scenario 3a - With LOS - Rx inside pocket In this scenario, The Rx was placed inside the pocket similarly to Scenario 2a and Scenario 2c. As showing in Fig. 3.2, both the Tx and Rx were traveling at pedestrian speeds walking on same side walk toward each other the away after crossing as illustrated in dotted lines. A total of 500000 Samples were collected for this scenario.

Scenario 3b - With LOS - Rx Next to face In contrast to previous scenario, the Rx antenna is placed next to the face at height of 1.5m. Both the Tx and Rx moved on the same side walk toward each other at pedestrian speeds as can be seen in dotted lines in Fig. 3.2.

In this scenario, a total of 600000 samples were collected.

3.4 Channel Modeling

In general, the received signal power at the receiver is determined by the transmitted power, path loss, large scale (shadowing), and small-scale fading [33]. The received signal power in (dB) can be generally expressed as $P_r = P_t - PL + S + \Omega$, where P_t is the transmitted power, PL is the path loss, S is the power of shadowing, and Ω is the power of small-scale fading [33]. In this section, we analyze the channel models for path loss, shadowing, and small-scale fading based on the measurements obtained in scenarios 1-4. We first obtain the path loss models, then remove the effect of path loss and obtain models for shadowing and small-scale fading. Table 3.1 provides a summary of the proposed models for all scenarios.

3.4.1 Path Loss Fading

According to the power law, the path loss in the received power is related to the separation distance between the Tx and Rx. The distance can be calculated by the spherical law of cosines or haversine formula using the latitude and longitude [71–73]. We use the spherical law of cosines in this paper.

$$d = \cos^{-1}\left(\sin\xi_{\mathrm{T}}\sin\xi_{\mathrm{R}} + \cos\xi_{\mathrm{T}}\cos\xi_{\mathrm{R}}\cos(\eta_{\mathrm{T}} - \eta_{\mathrm{R}})\right) \times 6.371 \times 10^6 \tag{3.4.1}$$

where d is the distance in meters, $\xi_{\mathrm{T}}, \eta_{\mathrm{T}}$ are, respectively, the latitude and longitude of the Tx recorded in the measurements, and $\xi_{\mathrm{R}}, \eta_{\mathrm{R}}$ are the latitude and longitude of the Rx.

Regression models with a simple form, $\mathrm{PL}(d) = \mathrm{PL}(d_0) + 10n\log(d/d_0)$, are proposed to estimate the path loss in [75, 76], where $\mathrm{PL}(d_0) = P_t - P_r(d_0) + 20\log h_t + 20\log h_r$ characterizes the path loss at the reference distance d_0, which is normally chosen as 1m for

indoor, 100m for micro cell, and 1km for urban mobile systems [33]. Values of PL(d_0) and the path loss exponent n are estimated by the measurements.

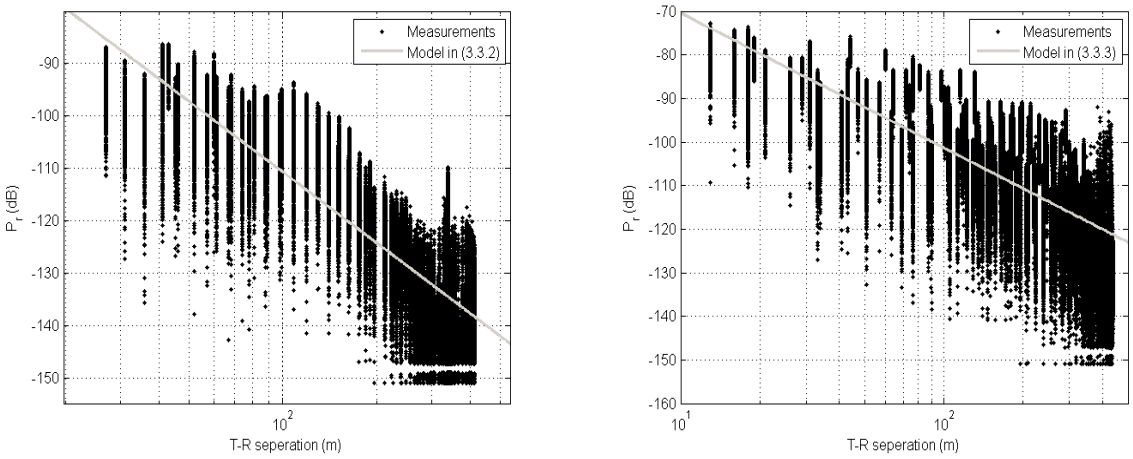

(a) Path loss for Scenario 1a

(b) Path loss for Scenario 1b

Figure 3.3: Path loss for Scenarios 1a and 1b

The path loss in Scenarios 1, 2, and 3 is expressed in the form, $\mathrm{PL}(d) = \mathrm{PL}(d_0) + 10n\log(d/d_0) - 20\log h_t - 20\log h_r$, where d_0 is chosen as 10m, h_t and h_r are the corresponding antenna heights in these scenarios. The values of PL(d_0) and n are obtained from measurements. The path loss models for Scenarios 1, 2, 3 are listed as follows:

$$\text{Scenario 1a:}\quad \mathrm{PL} = 68.2455 + 44.612\log(d/d_0) \tag{3.4.2}$$

$$\text{Scenario 1b:}\quad \mathrm{PL} = 72.5152 + 30.968\log(d/d_0) \tag{3.4.3}$$

$$\text{Scenario 2a:}\quad \mathrm{PL} = 58.3428 + 46.605\log(d/d_0) \tag{3.4.4}$$

$$\text{Scenario 2b:}\quad \mathrm{PL} = 64.9039 + 44.923\log(d/d_0) \tag{3.4.5}$$

$$\text{Scenario 2c:}\quad \mathrm{PL} = 79.0416 + 23.987\log(d/d_0) \tag{3.4.6}$$

$$\text{Scenario 2d:}\quad \mathrm{PL} = 80.8961 + 27.120\log(d/d_0) \tag{3.4.7}$$

$$\text{Scenario 3a:}\quad \mathrm{PL} = 76.7948 + 24.384\log(d/d_0) \tag{3.4.8}$$

$$\text{Scenario 3b: PL} = 75.1302 + 26.721 \log(d/d_0) \tag{3.4.9}$$

where the antenna height at the Tx and Rx $h_t = 1$m and $h_r = 1$m for Scenario 1a, 1b, 2a, 2c, and 3a. And, $h_t = 1$m and $h_r = 1.5$m for Scenario 2b, 2d, and 3b.

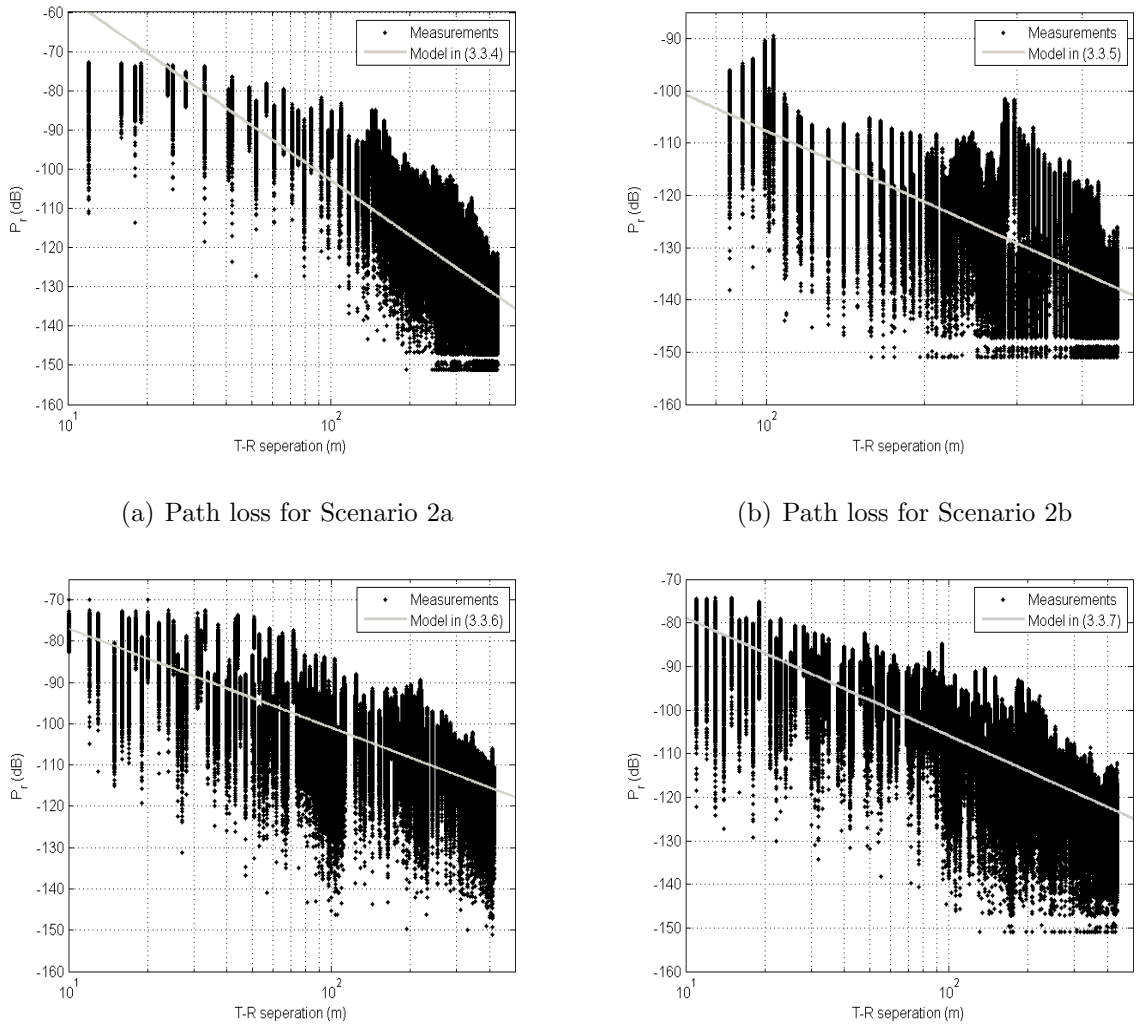

(a) Path loss for Scenario 2a

(b) Path loss for Scenario 2b

(c) Path loss for Scenario 2c

(d) Path loss for Scenario 2d

Figure 3.4: Path loss for Scenarios 2a-2d

We have the following observations for the path loss models for Scenario 1, 2, and 3:

- Scenario 1a: Measurements of the received signal power are shown in Fig. 3.4.2 with the proposed path loss model. The path loss exponent is found as $n = 4.4612$ and the

received power at reference distance is $P_r(d_0) = -66.2455$dB. The proposed model is valid for the Tx-Rx distance in $15 \sim 450$m, since the received power at $d = 450$m is close to -140 or -150dB, below which the measurement data is regraded as unreliable.

- Scenario 1b: As shown in Fig. 3.4.3, the path loss exponent is $n = 3.0968$ and reference path loss is $P_r(d_0) = -70.5152$dB. The model is valid for a similar range to Scenario 1a of Tx-Rx separation of $15 \sim 450$m. The path loss exponent and the reference path loss in Scenario 2b are found close to those observed in the suburban V2V channel measurements at 5.9GHz [32], where the exponent around 2.3 and reference path loss is 71.8 for data set 2 (data set 1 was collected in summer and data set 2 in winter). The path loss exponent in Scenario 2b is higher compared to the suburban V2V channels in [35], where the path loss exponent is 1.59. The reference path loss in Scenario 2b is found close to that in [35], which is 64.4dB, if the vehicle loss is taken into account for the Tx and Rx antennas inside the vehicles [68–70].

- Scenario 2a: Measurements of the received signal power are shown in Fig. 3.4(a) with the proposed path loss model. The path loss exponent is found as $n = 4.6605$ and the received power at reference distance is $P_r(d_0) = -56.3428$dB.

- Scenario 2b: As shown in Fig. 3.4(b), the path loss exponent is $n = 4.4923$ and reference path loss is $P_r(d_0) = -62.9039$dB. The model is valid for a wider range (than in Scenario 2a) of Tx-Rx separation in $80 \sim 480$m.

- Scenario 2c: Measurements of the received signal power are shown in Fig. 3.4(c) with the proposed path loss model. The path loss exponent is found as $n = 2.3987$ and the

received power at reference distance is $P_r(d_0) = -77.0416$dB. The proposed model is valid for the Tx-Rx distance in $10 \sim 430$m.

- Scenario 2d: As shown in Fig. 3.4(d), the path loss exponent is $n = 2.7120$ and reference path loss is $P_r(d_0) = -78.8961$dB. The model is valid for a wider range (than in Scenario 2a) of Tx-Rx separation in $10 \sim 450$m.

- Scenario 3a: Measurements of the received signal power are shown in Fig. 3.5(a) with the proposed path loss model. The path loss exponent is found as $n = 2.4384$ and the received power at reference distance is $P_r(d_0) = -78.7948$dB.

- Scenario 3b: As shown in Fig. 3.5(b), the path loss exponent is $n = 2.6721$ and reference path loss is $P_r(d_0) = -77.1302$dB. Both Scenario 3a and Scenario 3b models are valid for a range of Tx-Rx separation $10 \sim 380$m.

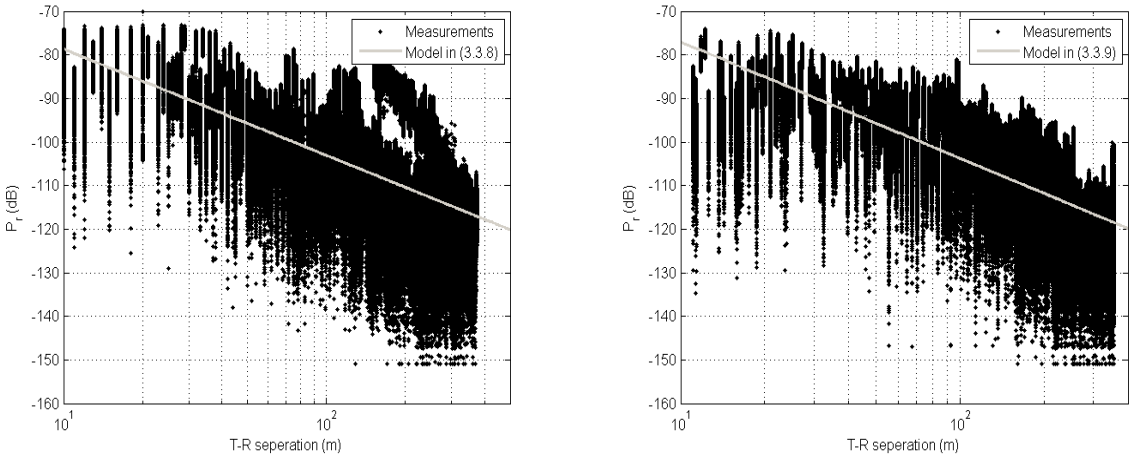

(a) Path loss for Scenario 3a

(b) Path loss for Scenario 3b

Figure 3.5: Path loss for Scenarios 3a and 3b

In summary, path loss exponent for LOS scenarios is lower than NLOS scenarios, which

is found ~ 1.4 in the IV2IV scenarios and $2.3 \sim 1.8$ in IV2W scenarios. The It can also be observed that path loss exponent for W2W LOS scenarios is very close. The path loss exponent in cases when the Rx is next to the face is (0.23, 0.3) higher for the LOS and very close (-0.17) in NLOS scenarios. It is expected to be higher in IV2IV NLOS scenario in compared to IV2W, but chances of LOS in between buildings were higher due to faster movements in IV2IV.

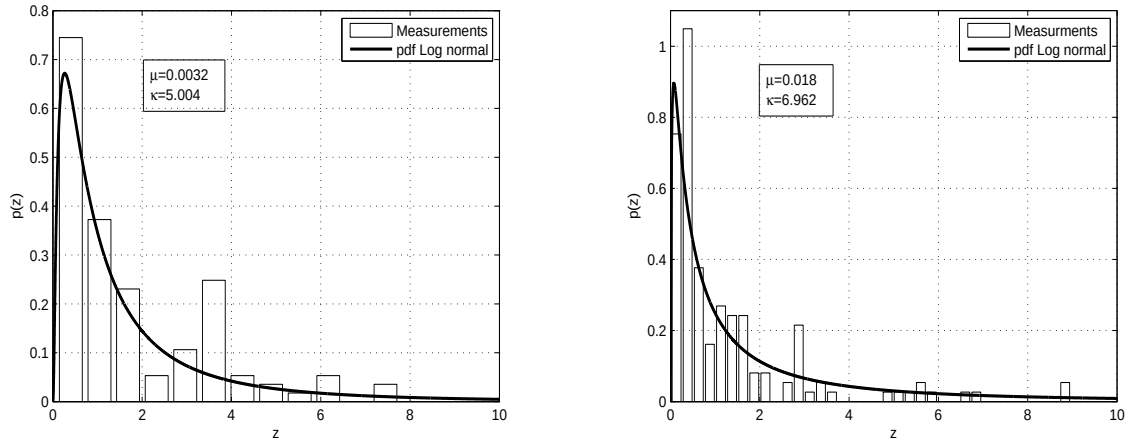

(a) Distribution of the shadowing in Scenario 1a (b) Distribution of the shadowing in Scenario 1b

Figure 3.6: Distributions of the shadowing in Scenarios 1a and 1b

3.4.2 Shadowing fading

Shadowing characterizes the local average variation of the envelope around the path loss. Typically, it is estimated by a moving average window over distance [33]. Depending on the test conditions and surrounding environments, the window size is usually $5 \sim 40$ times of the wavelength in the radio frequency [34]. Based on results of moving average windows with different sizes using the measurements, not shown here, window sizes of 1m, 2m, 3m, and 4m, respectively were examined. These window sizes correspond to 6.2, 12.3, 18.5, and 24.7

times of the wavelength in frequency 1.85GHz; It was observed that 4m window failed to follow the local average of shadowing in the received signal; the 1m and 2m windows seemed too small, as a result, picked up part of fast variations (small-scale fading) components. A $3m$ window appeared to be a reasonable choice to extract shadowing for the measurements which was used in our analysis.

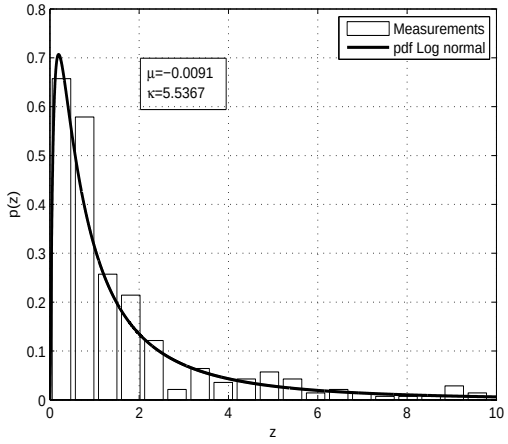

(a) Distribution of the shadowing in Scenario 2a

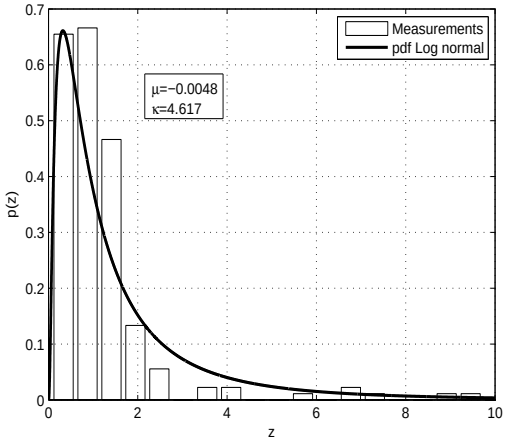

(b) Distribution of the shadowing in Scenario 2b

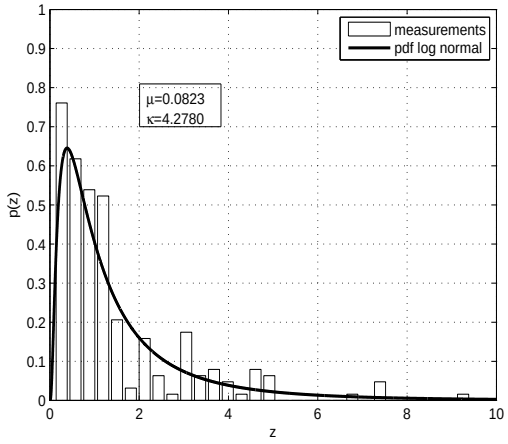

(c) Distribution of the shadowing in Scenario 2c

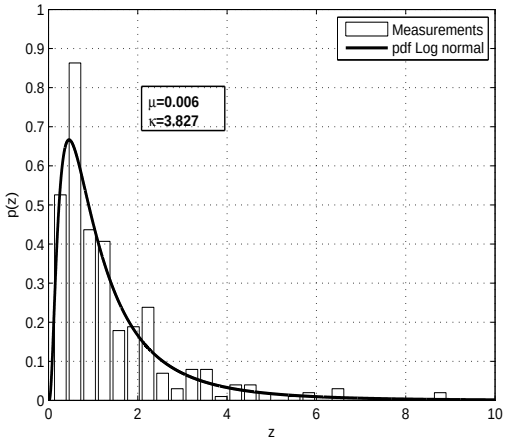

(d) Distribution of the shadowing in Scenario 2d

Figure 3.7: Distributions of the shadowing in Scenarios 2a and 2b

Let S represent the local average power (in dB) after removal of the path loss component.

The log-normal probability density function (pdf) for shadowing is given by (5.59) [77]: $f_s(s) = \frac{10}{\sqrt{2\pi}\kappa s \ln(10)} \exp\left(\frac{-(10\log s - \mu)^2}{2\kappa^2}\right)$, where ln is the natural logarithm of base e, mean $\mu = \mathbb{E}[S]$, and variance $\kappa^2 = \mathbb{V}[S]$. Figs. 3.6(a) to 3.8(b) show the distributions of shadowing in Scenarios 1 to 3. The probability density function of log-normal are also plotted with values of mean μ and standard deviation κ estimated from the measurements. As listed in Table 3.1, the means of shadowing are close to zero for all scenarios.

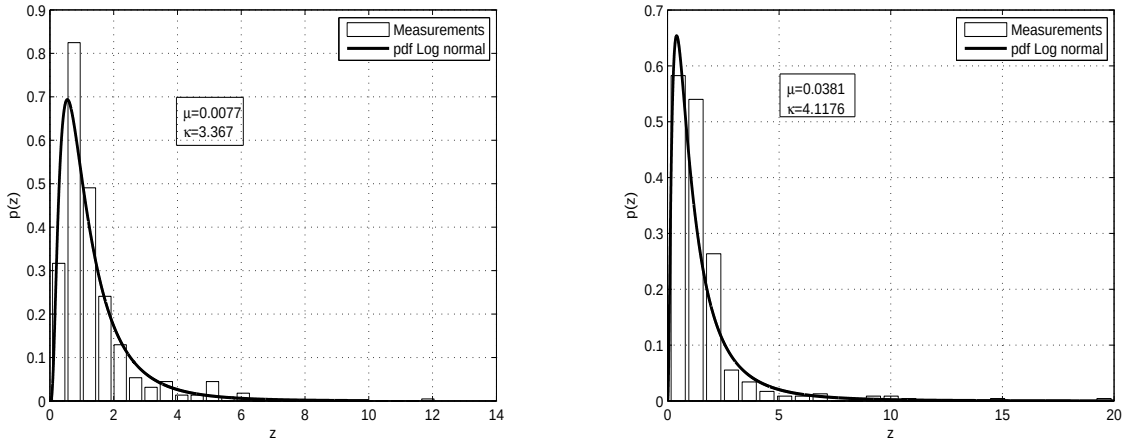

(a) Distribution of the shadowing in Scenario 3a (b) Distribution of the shadowing in Scenario 3b

Figure 3.8: Distributions of the shadowing in Scenarios 3a and 3b

The standard deviation of shadowing was found around ($4.6 \sim 5.5$dB) for all NLOS cases in suburban, and had a wider range ($3.4 \sim 7$dB) for LOS scenarios. It also obvious that having the Rx outside the vehicle results in lower standard deviation as can be seen in sub-scenarios of scenario 2 in compared with sub-scenarios of scenario 1. It can also be observed that ($-0.9 \sim 5.5$dB) difference between pocket and next to the face in NLOS IV2W and LOS IV2W respectively. Finally, (~ 0dB) mean is observed in all test scenarios.

It is worth noting that a zero mean in shadowing has been reported for V2V channel

measurements at 5.9GHz with antennas on roof [32,35]. Two data sets were collected summer and winter, respectively. Standard deviation of shadowing were found as $2.6 \sim 4.4$dB and $2 \sim 8.4$dB for the two data sets. Measurements with LOS in the suburban environment [35] suggested a standard deviation of shadowing around 4.41dB. This value is found close to the standard deviations in Scenarios 1a and Scenarios 1b at 1.85GHz with the antennas inside the vehicle.

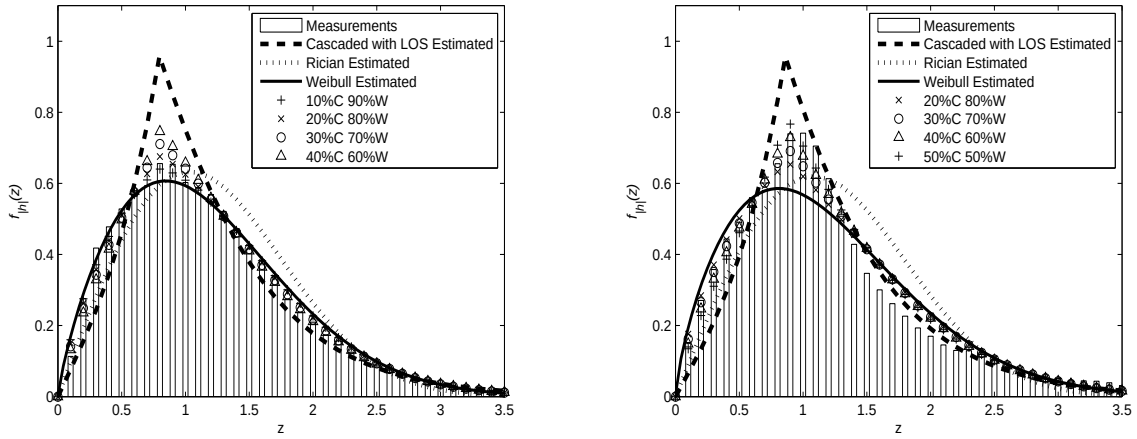

(a) Small-scale distribution in Scenario 1a

(b) Small-scale distribution in Scenario 1b

Figure 3.9: Small-scale distribution in Scenarios 1a and 1b

3.4.3 Small-scale Fading

Rician and Weibull distribution have been reported for small-scale fading in V2V channels [24, 29, 57, 78]. Cascaded (double) Rayleigh fading has been suggested by the measurements in M2M and V2V channels [21, 23, 25–27, 57]. Specifically, The measurements in [23] show that the outdoor-to-indoor M2M channel follows a double Rayleigh distribution rather than a single Rayleigh distribution, and similar observations are obtained from the measurements in [26, 27]. Measurements of V2V channels in [21, 57] indicate that severe (worse than

Rayleigh) fading appears in city motorways and highways. Authors in [26,27] have suggested that M2M channels may experience fading as a combination of single, double, triple, and quadruple product of Rayleigh fading components. In this paper, we study three distributions in our experiments: Rician, cascaded-Rayleigh with LOS, and Weibull distributions. To fully characterize the small-scale fading in the collected measurements, we also consider a distribution by a combination of Rician and cascaded-Rayleigh with LOS. The probability density functions of Rician, cascaded-Rayleigh with LOS, and Weibull distributions are well studied in literature, we re-state the results for convenience of readers.

- Rician distribution: A M2M channel with Rician distribution is expressed as [17],

$$h_{\mathrm{R}}(t) = \frac{\sqrt{\Omega}g(t) + \sqrt{\Omega K}e^{j(2\pi t f_{\mathrm{L}}\cos\theta_{\mathrm{L}}+\phi_0)}}{\sqrt{(1+K)}}, \tag{3.4.10}$$

  where subscript "R" represents Rician, Ω is power for small-scale fading, the complex exponential $e^{j(2\pi t f_{\mathrm{L}}\cos\theta_{\mathrm{L}}+\phi_0)}$ is the LOS component, K is the spectral to the scatter power ratio, f_{L} is the Doppler frequency shift due to the motions in Tx and Rx, θ_{L} is the angle of the relative velocity (between Tx and Tx) with respect to the Tx-Rx direct path, and ϕ_0 is the random phase offset [17,36], $g(t)$ characterizes the scattering component without LOS, and it is usually modeled as a complex Gaussian process whose envelope follows a Rayleigh distribution [14,17],

$$g(t) = \sqrt{\frac{1}{MN}}\sum_{n=1}^{N}\sum_{m=1}^{M} e^{j\left(2\pi f_1 t\cos\gamma_n + 2\pi f_2 t\cos\zeta_m + \theta_{nm}\right)} \tag{3.4.11}$$

  where N and M designate the number of scatters around the Tx and Rx, respectively, f_1 and f_2 are respectively, the maximum Doppler's shift frequencies at the Tx and Rx, $\theta_{nm} \in [-\pi,\pi), n = 1,\cdots,N, m = 1,\cdots,M$, are the independent and uniformly

distributed phase shifts, γ_n represents the angle of departure for the n-th scatter at the Tx, and ζ_m is the angle of arrival for the m-th scatter at the Rx. Using (2.50) in [36], the pdf of Rician distribution can be obtained as

$$f_{|h_{\mathrm{R}}|}(z) = \frac{2z(K+1)}{\Omega} \exp\Big(- \frac{z^2(K+1)}{\Omega} - K\Big) I_0\Big(2z\sqrt{\frac{K(K+1)}{\Omega}}\Big), z \geq 0 \qquad (3.4.12)$$

where I_0 is the modified Bessel function of the first kind zero-order.

- Cascaded Rayleigh with LOS: A model for M2M channel of cascaded Rayleigh with LOS has the form

$$h_{\mathrm{C}}(t) = \frac{\sqrt{\Omega} g_1(t) g_2(t) + \sqrt{\Omega K} e^{j(2\pi t f_{\mathrm{L}} \cos\theta_{\mathrm{L}} + \phi_0)}}{\sqrt{(1+K)}}, \qquad (3.4.13)$$

where subscript "C" represents cascaded, $g_1(t)$ and $g_2(t)$ are independent complex Gaussian processes whose envelop follow Rayleigh distribution. The scattering component in the channel is cascaded Rayleigh fading (instead of a single Rayleigh fading) characterized by the product $g_1(t)g_2(t)$,

$$g_1(t)g_2(t) = \sqrt{\frac{1}{N}} \sum_{n=1}^{N} e^{j\left(2\pi f_1 t \cos\gamma_n + \theta_n\right)} \sqrt{\frac{1}{M}} \sum_{m=1}^{M} e^{j\left(2\pi f_2 t \cos\zeta_m + \Phi_m\right)} \qquad (3.4.14)$$

θ_n and $\Phi_m \in [-\pi, \pi), n = 1, \cdots, N, m = 1, \cdots, M$, are the phase shifts for each scatter at the Tx and to the Rx, and they are independent and uniformly distributed for all n and m. Using Eq.(12) in [60], one can obtain the pdf for cascaded Rayleigh with LOS channel in (3.4.13) as follows:

$$f_{|h_{\mathrm{C}}|}(z) = \begin{cases} \frac{z}{\sigma_1^2\sigma_2^2} I_0\big(\frac{z}{\sigma_1\sigma_2}\big) K_0\big(2\sqrt{\frac{K}{1+K}}\big), & \text{for } z < \sqrt{\frac{\Omega K}{1+K}} \\ \frac{z}{\sigma_1^2\sigma_2^2} I_0\big(2\sqrt{\frac{K}{1+K}}\big) K_0\big(\frac{z}{\sigma_1\sigma_2}\big), & \text{for } z \geq \sqrt{\frac{\Omega K}{1+K}} \end{cases} \qquad (3.4.15)$$

where K_0 is the modified Bessel function of the second kind zero-order.

- Weibull distribution: The pdf for a Weibull distribution channel has the form [57]

$$f_{|h_{\mathrm{W}}|}(z) = \beta z^{\beta-1}\left(\sqrt{\frac{\Omega}{\Gamma(1+2/\beta)}}\right)^{-\beta} \exp\left(-\left(\frac{z\sqrt{\Gamma(1+2/\beta)}}{\sqrt{\Omega}}\right)^{\beta}\right) \tag{3.4.16}$$

where subscript "W" represents Weibull, $\Gamma(\cdot)$ is the gamma function, and β is the shape parameter for Weibull distribution.

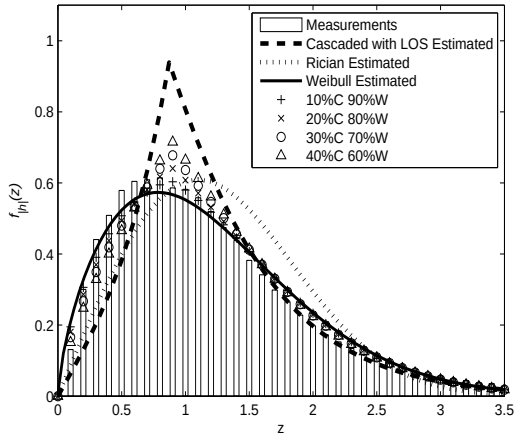

(a) Small-scale distribution in Scenario 2a

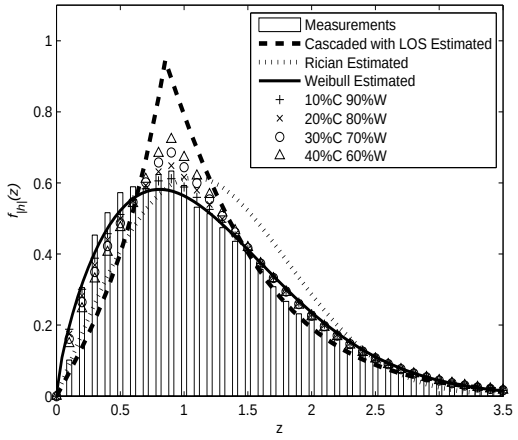

(b) Small-scale distribution in Scenario 2b

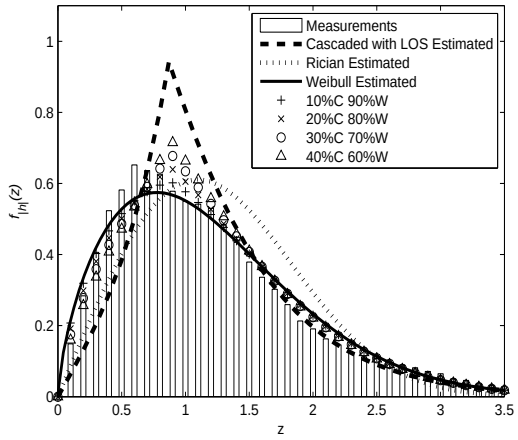

(c) Small-scale distribution in Scenario 2c

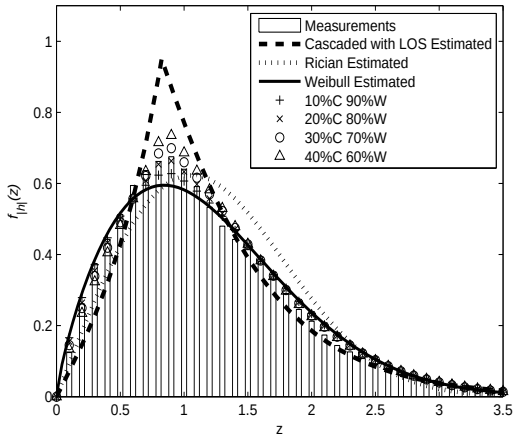

(d) Small-scale distribution in Scenario 2d

Figure 3.10: Small-scale distribution in Scenarios 2a-2d

To verify the closest of the models, we calculate the mean square error (MSE) of the models by, MSE $= \frac{\sum_{i=1}^{N} |\Delta_i|^2}{N}$, where N is the total number of measurements samples, and Δ_i is the difference between the histogram of measured small scale and its theistical estimated for the ith sample.

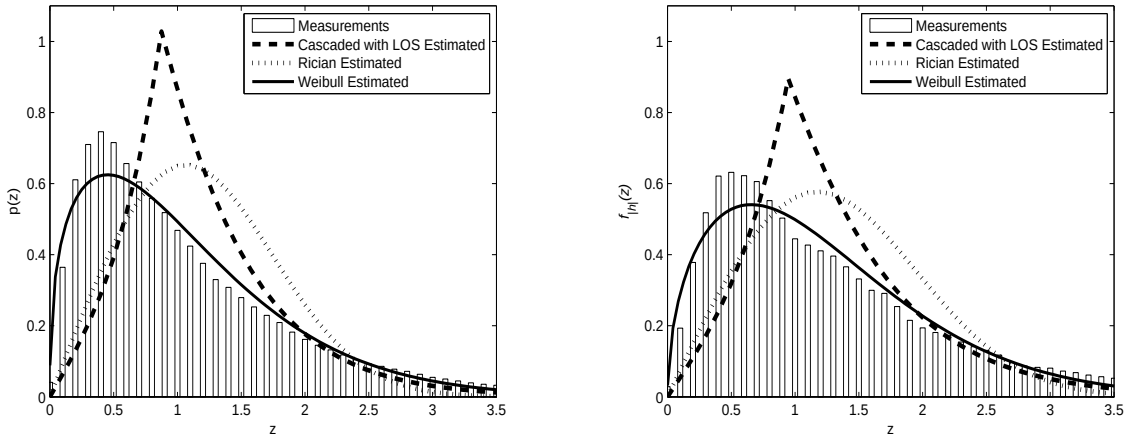

(a) Small-scale distribution in Scenario 3a

(b) Small-scale distribution in Scenario 3b

Figure 3.11: Small-scale distribution in Scenarios 3a and 3b

Extending the observations in [26,27] that M2M channels may experience fading which is a combination of single Rayleigh and cascaded Rayleigh fading, we try to fit the measurement data using a pdf which combines the distributions of Weibull and cascaded Rayleigh with LOS, as Weibull is general case for Rician: $f_{\text{com}}(z,\tau) = (1-\tau)f_{|h_{\text{W}}|}(z)+(\tau)f_{|h_{\text{C}}|}(z), 0 \leq \tau \leq 1$, where the subscript "com" represents combination. For special cases when $\tau = 0$ or 1, $f_{\text{com}}(z,\tau)$ becomes $f_{|h_{\text{W}}|}(z)$ or $f_{|h_{\text{C}}|}(z)$, respectively. Combinations of Rician and cascaded Rayleigh with LOS were also investigated, but these fits were not as close as $f_{\text{com}}(z,\tau)$ fits.

Removing the path loss and shadowing components from the received power in the measurements, we obtain the small-scale fading components for all scenarios. The power Ω and

TABLE 3.1:

SCENARIOS SUMMARY

Scenario		heights h_t(m), h_r(m)	Path loss $n, P(d_0)$ (dB)	Shadowing μ (dB), κ (dB)	K-factor	Ω	Envelope
Scenario 1	1a	1, 1	4.4612, 68.2455	0.0032, 5.0035	0.5187	1.8546	$f_{\text{com}}(z, 0.1)$ $\beta = 1.8$
	1b	1, 1	3.0968, 72.5152	0.0180, 6.9619	0.6105	1.9553	$f_{\text{com}}(z, 0.4)$ $\beta = 1.7$
Scenario 2	2a	1, 1	4.6605, 58.3428	-0.0091, 5.5367	0.6030	2.0219	$f_{\text{com}}(z, 0.1)$ $\beta = 1.68$
	2b	1, 1.5	4.4923, 64.9039	-0.0048, 4.6170	0.5808	1.9758	$f_{\text{com}}(z, 0.1)$ $\beta = 1.7$
	2c	1, 1	2.3987, 79.0416	0.0823, 4.2780	0.6041	2.0099	$f_{\text{com}}(z, 0.1)$ $\beta = 1.65$
	2d	1, 1.5	2.7120, 80.8961	0.0055, 3.8269	0.5493	1.9168	$f_{\text{com}}(z, 0.2)$ $\beta = 1.77$
Scenario 3	3a	1, 1	2.4384, 76.7948	0.0077, 3.3670	0.7357	1.8046	Weibull $\beta = 1.35$
	3b	1, 1.5	2.6721, 75.1302	0.0381, 4.1176	0.6495	2.2742	Weibull $\beta = 1.5$

the spectral to the scatter power ratio K-factor are estimated from the measurements by, $\Omega = \mathbb{E}[|h(t)|^2]$ [36], and $K = \frac{\sqrt{1-\gamma}}{1-\sqrt{1-\gamma}}$ [79], where $\gamma = \frac{\mathbb{V}[|h(t)|^2]}{(\mathbb{E}[|h(t)|^2])^2}$, and $|h(t)|$ is the envelope of the small-scale component (here we drop the subscript in the channel without confusion).

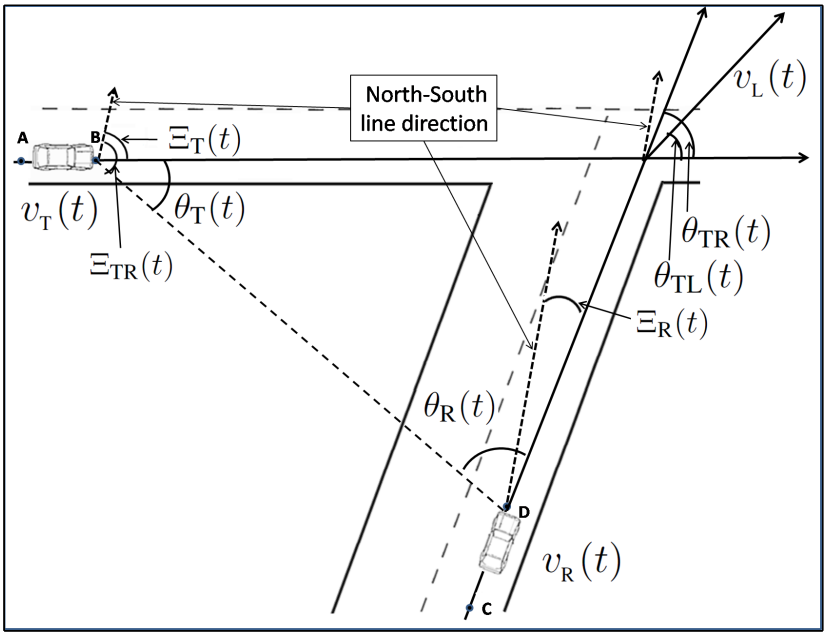

Figure 3.12: Doppler effect due to relative movement in Tx and Rx

Table 3.1 summarizes the estimated values of Ω and K-factor, and the small-scale distributions for all the scenarios under study. The values of total power of spectral + scatter in small scale, was found $\Omega = (1,85 \sim 2.27)$. It is found 1.8546 for Scenario 1a, which is expected lower than the LOS case in scenario 1b that is 1.9553. And between 1.9168 to 2.0219 for sub-scenarios 2 which is slightly higher than sub-scenarios 1. The values of K-factor was found $(0.5 \sim 0.7)$ in all scenarios. This indicates that the scatter contributes to about $(\%30 \sim \%50)$ of the received small scale component and the rest is in the spectral component. The lowest is found for Scenarios 1a with 0.5187. This means that half the

small scale component is spectral and the scatter component is contributing to the second half. K-factor is higher than for scenario 1b and sub-scenarios 2 than scenario 1a and very close, between 0.5493 to 0.6041. This is expected since the visibility between the Tx and Rx is better compared with scenario 1a during the tests. A strong K-factor in the LOS component contributes to the average received power. More detailed observations in each scenario are as follows:

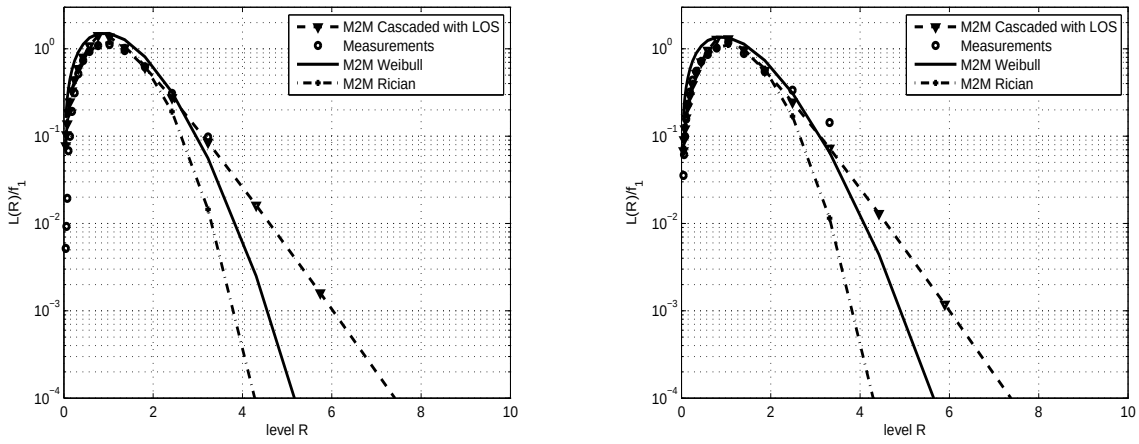

(a) LCR in Scenario 1a

(b) LCR in Scenario 1b

Figure 3.13: LCR in Scenarios 1a and 1b

- Scenario 1: The distribution of small-scale fading is shown by the histogram in Figs. 3.9(a) and 3.9(b). The probability density functions for Rician, Weibull, cascaded-Rayleigh with LOS, and combination of them $f_{\text{com}}(x, \tau)$ with $\tau = 0.5, 0.4, 0.3, 0.2$, and 0.1 are plotted, respectively. It can be noticed that the envelope in this scenario does not follow a Rician, nor a Weibull distribution. In Fig. 3.9(a), it is obvious that the $f_{\text{com}}(z, 0.1)$ distribution, labeled as $10\%C$ $90\%W$, has the closest fit to measured data with parameter $\beta = 1.8$. While in Fig. 3.9(b), $f_{\text{com}}(z, 0.4)$ is labeled as $40\%C$ $60\%W$ gave the

closest fit to the distribution with parameter $\beta = 1.7$.

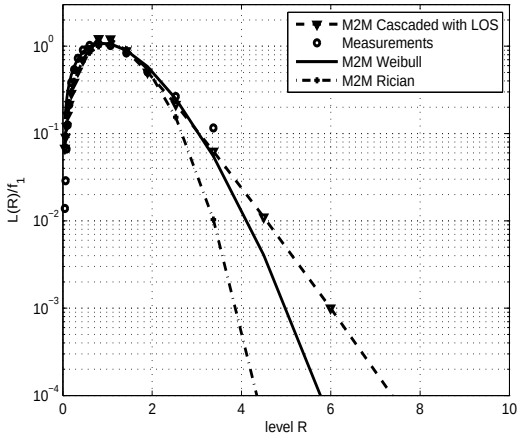

(a) LCR in Scenario 2a

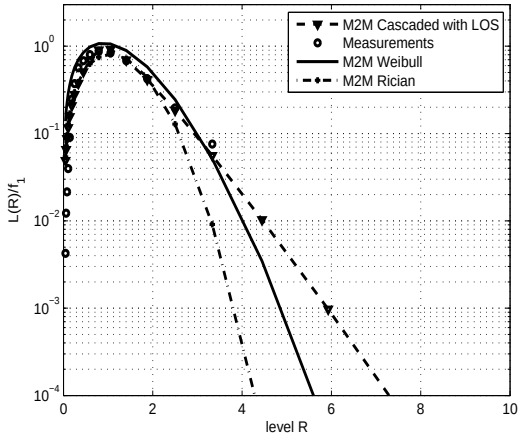

(b) LCR in Scenario 2b

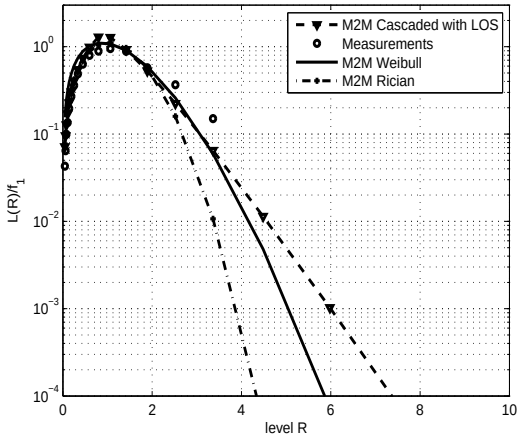

(c) LCR in Scenario 2c

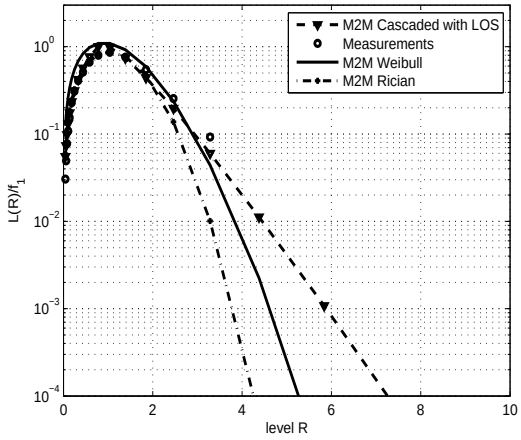

(d) LCR in Scenario 2d

Figure 3.14: LCR in Scenarios 2a-2d

- Scenario 2: Figs. 3.10(a), 3.10(b), and 3.10(c) show, respectively, the small-scale envelope distribution for Scenario 2a, Scenario 2b and Scenario 2c. The distribution of Rician, cascaded Rayleigh with LOS, and Weibull distributions are plotted. Again, $f_{\text{com}}(z, 0.1)$ distribution, labeled as $10\%C$ $90\%W$ with $\beta = 1.77$, is the winner in these

scenarios with parameter $\beta = 1.68,\ 1.7,$ and 1.65 respectively. In Figs. 3.10(d), the closest fit was found $f_{\text{com}}(z, 0.2)$ and labeled as $20\%C$ $80\%W$ with $\beta = 1.77$.

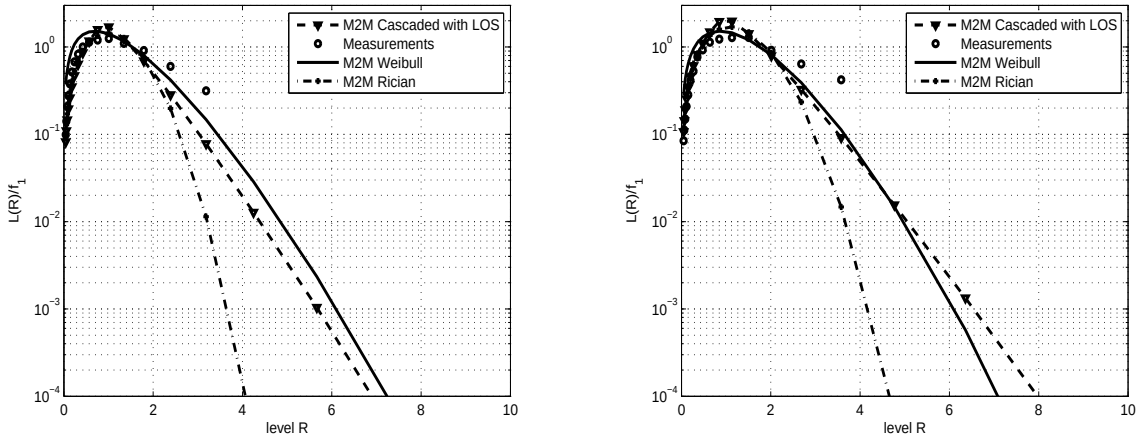

(a) LCR in Scenario 3a

(b) LCR in Scenario 3b

Figure 3.15: LCR in Scenarios 3a and 3b

- Scenario 3: Figs. 3.11(a), and 3.11(b) plots the distribution of the envelope for these sub-scenarios. It can be indicated that the Weibull distribution is the best fit for these scenarios with $\beta = 1.35$ and $\beta = 1.5$ respectively.

3.5 Evaluation of Higher-Order Statistics

The level crossing rate and the average fade duration are two important statistical properties related to channel fading. At a specified level R, the LCR for a channel envelope is the rate (in crossings per second) at which the channel envelope crosses in the positive (or negative) direction [13, 36]. The AFD is the average time duration that the envelope remains below the level R [36]. The expressions of LCR and AFD for Rician, cascaded with Rayleigh, and Weibull distributions are presented as follows.

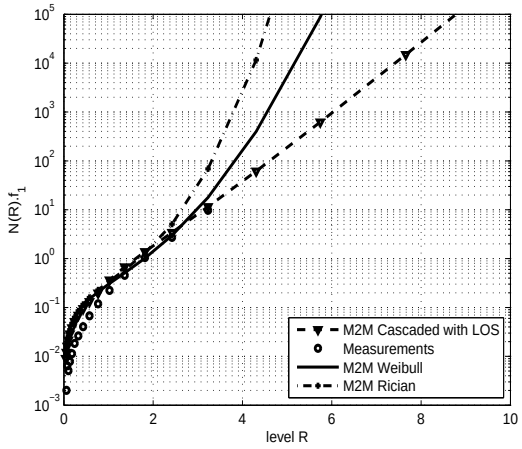

(a) AFD in Scenario 1a

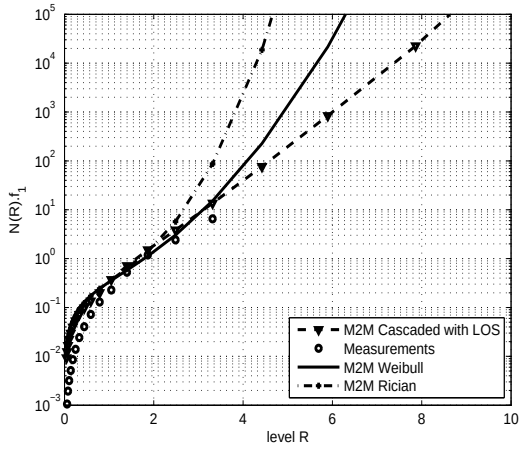

(b) AFD in Scenario 1b

Figure 3.16: AFD in Scenario 1a and 1b

3.5.1 Expressions of LCR and AFD

Rician Distribution: The LCR can be obtained using (2.91) in [36], $L_{|h_{\mathrm{R}}|}(R) = \int_0^\infty \dot{z} f_{|h_{\mathrm{R}}|}(z, \dot{z}) d\dot{z}$, where R is the level, and $f_{|h_{\mathrm{R}}|}(z, \dot{z})$ is the joint pdf given by

$$f_{|h_{\mathrm{R}}|}(z, \dot{z}) = \frac{z}{\sqrt{(2\pi)^3 B b_0}} \exp\Big[- \frac{z^2 + \hat{s}^2}{2b_0} \Big] \int_{-\pi}^{\pi} \exp\Big[\frac{z\hat{s}\cos\theta}{b_0} - \Big(\frac{b_0 \dot{z} + b_1 \hat{s} \sin\theta}{\sqrt{2Bb_0}} \Big)^2 \Big] d\theta \quad (3.5.1)$$

and where $2b_0 = \frac{\Omega}{K+1}$, $\hat{s} = \sqrt{\frac{\Omega K}{K+1}}$, $b_1 = -2b_0\sqrt{K}\pi f_3 \cos\theta_{\mathrm{L}}$, and $B = \frac{\Omega^2\pi^2(f_1^2+f_2^2)}{2(1+K)^2}$. Using the joint pdf in (3.5.1)and the steps in Appendix H, the LCR for the M2M Rician channel is calculated by

$$\begin{aligned} L_{|h_{\mathrm{R}}|}(R) = \rho\sqrt{\frac{f_1^2+f_2^2}{2\pi}} \exp\big[-(1+K)\rho^2 - K \big] \int_{-\pi}^{\pi} \exp\Big[2\rho\sqrt{K(1+K)}\cos\theta \Big] \\ \times \Bigg(\sqrt{\frac{2\pi}{f_1^2+f_2^2}} f_3 \cos\theta_{\mathrm{L}} K \sin\theta \ \mathrm{erfc}\Big(- f_3 \cos\theta_{\mathrm{L}} K \sqrt{\frac{2}{f_1^2+f_2^2}} \sin\theta \Big) \\ + \exp\Big[- \frac{(f_3\cos\theta_{\mathrm{L}})^2 K^2 \sin^2\theta}{2(f_1^2+f_2^2)} \Big] \Bigg) d\theta \end{aligned} \quad (3.5.2)$$

where $\mathrm{erfc}(\cdot)$ is the complementary error function [63], $\rho = R/\sqrt{\Omega}$.

The AFD for the M2M Rician channel, $T_{|h_{\mathrm{R}}|}(R)$ is calculated by

$$T_{|h_{\mathrm{R}}|}(R) = \frac{1 - Q\Big(\sqrt{2K}, \sqrt{\frac{2(K+1)}{\Omega}}R\Big)}{L_{|h_R(t)|}(R)} \tag{3.5.3}$$

where $Q(\cdot)$ is Marcum's Q-function [63]. It is worth noting that the LCR and AFD in [13] and [36] are the special cases in (3.5.2) and (3.5.3), for without LOS $K = 0$, and fixed-to-mobile (F2M) with $f_3 = f_1 = 0$.

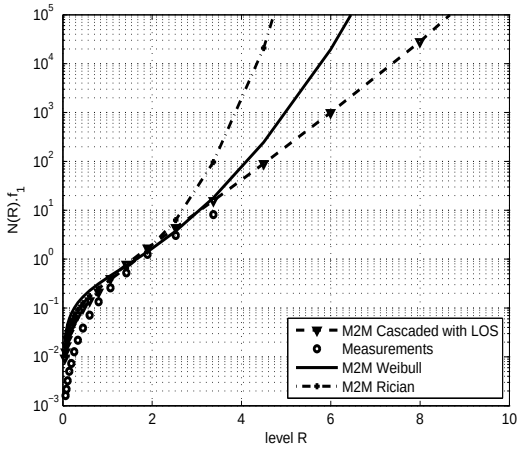

(a) AFD in Scenario 2a

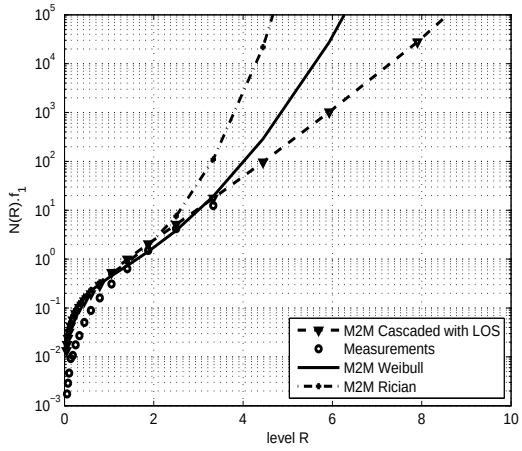

(b) AFD in Scenario 2b

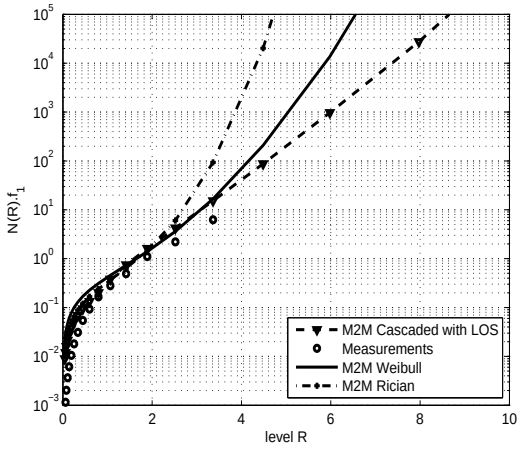

(c) AFD in Scenario 2c

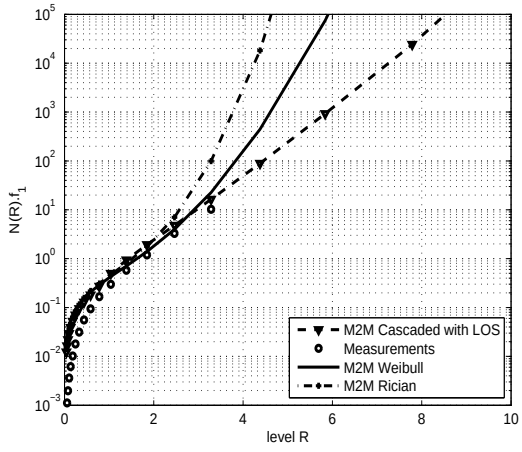

(d) AFD in Scenario 2d

Figure 3.17: AFD in Scenarios 2a-2d

Cascaded Rayleigh with LOS: Using (30) in [60], the LCR for channel in (3.4.13) is given by

$$L_{|h_{\mathrm{C}}|}(R) = \Big(\frac{1+K}{\Omega}\Big)^{\frac{3}{4}} R f_1 \int_0^{\infty}\int_{-\pi}^{\pi} x^{-2}\sqrt{a^2 y_1(R,\vartheta)+x^4} \\ \times \bigg(y_2(R,\vartheta,x)\Big(1+\mathrm{erf}\Big(\frac{y_2(R,\vartheta,x)}{\sqrt{2}}\Big)\Big) + \sqrt{\frac{2}{\pi}} e^{-\frac{y_2^2(R,\vartheta,x)}{2}}\bigg) e^{-\sqrt{\frac{1+K}{\Omega}}(x^2+\frac{y_1(R,\vartheta)}{x^2})} d\vartheta dx \tag{3.5.4}$$

where $\mathrm{erf}(\cdot)$ is the error function [63], $a = f_2/f_1$, $y_1(R,\vartheta)$, and $y_2(R,\vartheta,x)$ are defined, respectively, as

$$y_1(R,\vartheta) = R^2 + \frac{\Omega K}{1+K} - 2R\cos(\vartheta)\sqrt{\frac{\Omega K}{1+K}} \tag{3.5.5}$$

$$y_2(R,\vartheta,x) = \frac{2x f_3 \cos\theta_{\mathrm{L}}\sqrt{K}\sin(\vartheta)\sqrt{\sqrt{\Omega}}}{f_1\sqrt{\sqrt{1+K}}\sqrt{a^2 y_1(R,\vartheta)+x^4}}. \tag{3.5.6}$$

The AFD for the channel of cascaded Rayleigh with LOS can be calculated as $T_{|h_{\mathrm{C}}|}(R) = \frac{P_Z(z\le R)}{L_{|h_{\mathrm{C}}|}(R)}$, where $L_{|h_{\mathrm{C}}|}(R)$ is given in (3.5.4), and the CDF of the envelope $z = |h_{\mathrm{C}}(t)|$ is given by

$$P_{|h_{\mathrm{C}}|}(Z\le z) = \begin{cases} \frac{z}{\sigma_1\sigma_2} I_1\big(\frac{z}{\sigma_1\sigma_2}\big) K_0\big(2\sqrt{\frac{K}{1+K}}\big), & \text{for } z < \sqrt{\frac{\Omega K}{1+K}} \\ 1 - \frac{z}{\sigma_1\sigma_2} I_0\big(2\sqrt{\frac{K}{1+K}}\big) K_1\big(\frac{z}{\sigma_1\sigma_2}\big), & \text{for } z \ge \sqrt{\frac{\Omega K}{1+K}} \end{cases} \tag{3.5.7}$$

where I_1 and K_1 are modified Bessel functions first and second kinds first-order, respectively.

Weibull Distribution: The LCR and ADF for F2M Weibull can be found in (9) [80]. To add the effect of the Tx mobility, we replace the variance in time derivative of the channel envelop $\widehat{\sigma}^2$ by $\widehat{\sigma}^2 = \pi^2\Omega(f_1^2+f_2^2)$, which is also known as the second moment of the spectrum for M2M channel in (A5) [13]. Inserting $\widehat{\sigma}^2$ into (9) [80], the LCR and AFD for M2M Weibull channel envelope can be expressed, respectively, as

$$L_{|h_{\mathrm{W}}|}(R) = \sqrt{2\pi(f_1^2+f_2^2)}\bigg(R\sqrt{\frac{\Gamma(1+\frac{2}{\beta})}{\Omega}}\bigg)^{\frac{\beta}{2}} \exp\bigg[-\bigg(R\sqrt{\frac{\Gamma(1+\frac{2}{\beta})}{\Omega}}\bigg)^{\beta}\bigg] \tag{3.5.8}$$

$$T_{|h_{\mathrm{W}}|}(R) = \frac{1 - \exp\left[-\left(R\sqrt{\frac{\Gamma(1+\frac{2}{\beta})}{\Omega}}\right)^{\beta}\right]}{L_{|h_{\mathrm{W}}|}(R)}. \tag{3.5.9}$$

3.5.2 Simulations of LCR and AFD

To evaluate the LCR and AFD from the theoretical expressions, we need to determine the following parameters: doppler frequencies at the Tx and Rx f_1 and f_2, doppler frequency in the LOS component f_{L}, and angle of relative velocity θ_{L}. Using the measurement, the doppler frequencies at the Tx and Rx are calculated by $f_1 = \frac{\mathbb{E}[|v_{\mathrm{T}}(t)|]}{\lambda}$ and $f_2 = \frac{\mathbb{E}[|v_{\mathrm{R}}(t)|]}{\lambda}$, where $v_{\mathrm{T}}(t)$ and $v_{\mathrm{R}}(t)$ are, respectively, the velocities of the Tx and Rx in meters per second (m/s) at time t. The Doppler frequency in the LOS component is calculated by $f_{\mathrm{L}} = \frac{\mathbb{E}[|v_{\mathrm{L}}(t)|]}{\lambda}$, where $v_{\mathrm{L}}(t)$ is the relative speed with a magnitude $|v_{\mathrm{L}}(t)| = \sqrt{\left(v_{\mathrm{T}}(t) - v_{\mathrm{R}}(t)\cos\left(\theta_{\mathrm{TR}}(t)\right)\right)^2 + \left(v_{\mathrm{R}}(t)\sin\left(\theta_{\mathrm{TR}}(t)\right)\right)^2}$, where $\theta_{\mathrm{TR}}(t)$ is the angle between $v_{\mathrm{T}}(t)$ and $v_{\mathrm{R}}(t)$. If the Tx and Rx travel in a opposite direction, then $\theta_{\mathrm{TR}}(t) = \pi$; and the relative speed achieves a magnitude $|v_{\mathrm{L}}(t)| = |v_{\mathrm{T}}(t) + v_{\mathrm{R}}(t)|$, which is the case presented in [60], [67]. The angle between the relative velocity and the LOS path is evaluated as, $\theta_{\mathrm{L}} = \mathbb{E}\Big[\theta_{\mathrm{T}}(t) + \tan^{-1}\left(\frac{v_{\mathrm{R}}(t)\sin\left(\theta_{\mathrm{TR}}(t)\right)}{v_{\mathrm{T}}(t) - v_{\mathrm{R}}(t)\cos\left(\theta_{\mathrm{TR}}(t)\right)}\right)\Big]$, where $\theta_{\mathrm{T}}(t)$ is the angle between $v_{\mathrm{T}}(t)$ and the LOS path, $\theta_{\mathrm{R}}(t)$ is the angle between $v_{\mathrm{R}}(t)$ and the LOS path.

These angles are illustrated in Fig. 3.12, when Tx and Rx approach an intersection. The Tx travels at speed $v_{\mathrm{T}}(t)$ and is at point A at time $t - \Delta t$, and the Rx travels at $v_{\mathrm{R}}(t)$ and is at point C. At time t, the Tx arrives at point B and the Rx gets to point D. Using the bearing angles referenced by the north-south line, $\theta_{\mathrm{T}}(t), \theta_{\mathrm{R}}(t)$, and $\theta_{\mathrm{TR}}(t)$ are calculated, respectively, by

$$\theta_{\mathrm{T}}(t) = \Xi_{\mathrm{TR}}(t) - \Xi_{\mathrm{T}}(t)\ ,\ \theta_{\mathrm{R}}(t) = \pi - \Xi_{\mathrm{TR}}(t) + \Xi_{\mathrm{R}}(t)\ ,\ \theta_{\mathrm{TR}}(t) = \Xi_{\mathrm{T}}(t) - \Xi_{\mathrm{R}}(t), \tag{3.5.10}$$

where $\Xi_{\mathrm{T}}(t)$ and $\Xi_{\mathrm{R}}(t)$ are, respectively, the bearing angles of $v_{\mathrm{T}}(t)$ and $v_{\mathrm{T}}(t)$ referenced by the north-south line, and $\Xi_{\mathrm{TR}}(t)$ is the bearing angle of the Tx-Rx LOS path referenced by the north-south line. These angles are give by

$$\Xi_{\mathrm{TR}}(t) = \tan^{-1}\left(\frac{\sin(\eta_{\mathrm{R}}(t)-\eta_{\mathrm{T}}(t))\cos(\xi_{\mathrm{R}}(t))}{\cos(\xi_{\mathrm{T}}(t))\sin(\xi_{\mathrm{R}}(t))-\sin(\xi_{\mathrm{T}}(t))\cos(\xi_{\mathrm{R}}(t))\cos(\eta_{\mathrm{R}}(t)-\eta_{\mathrm{T}}(t))}\right) \tag{3.5.11}$$

$$\Xi_{\mathrm{x}}(t) = \tan^{-1}\left(\frac{\sin\left(\eta_{\mathrm{x}}(t)-\eta_{\mathrm{x}}(t-\Delta t)\right)\cos\left(\xi_{\mathrm{x}}(t)\right)}{\cos\left(\xi_{\mathrm{x}}(t-\Delta t)\right)\sin\left(\xi_{\mathrm{x}}(t)\right)-\sin(\xi_{\mathrm{x}}(t-\Delta t))\cos\xi_{\mathrm{x}}(t)\cos\left(\eta_{\mathrm{x}}(t)-\eta_{\mathrm{x}}(t-\Delta t)\right)}\right) \tag{3.5.12}$$

and where $\eta_{\mathrm{T}}(t)$ and $\xi_{\mathrm{T}}(t)$ are the coordinates at Tx, and $\eta_{\mathrm{R}}(t)$ and $\xi_{\mathrm{R}}(t)$ are the coordinates at Rx, and subscript x takes value of T or R, respectively. The time difference Δt is chosen as 3 seconds in the paper, to ensure the vehicle (or test cart) moves enough distance to determine its moving direction.

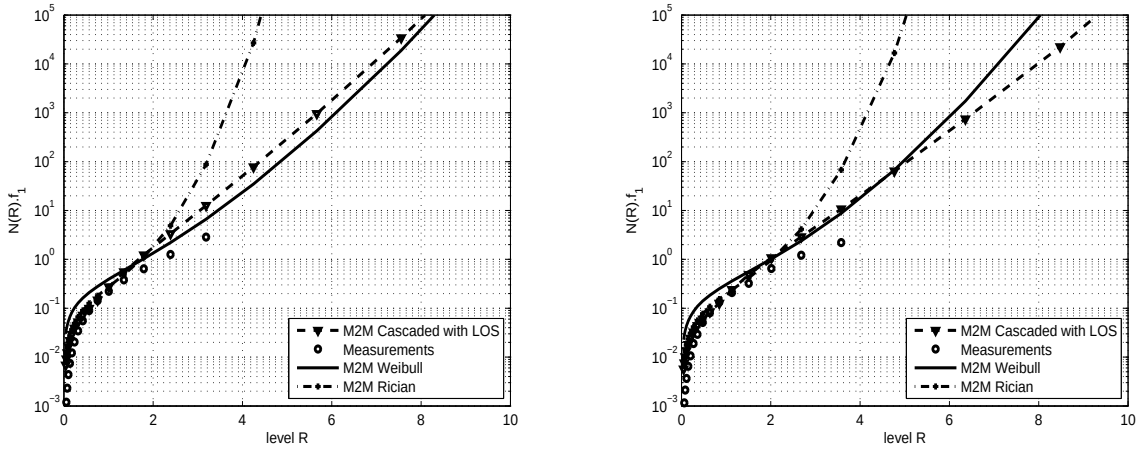

(a) AFD in Scenario 3a

(b) AFD in Scenario 3b

Figure 3.18: AFD in Scenario 3a and 3b

Figs. 3.13(a)-3.15(b) and 3.16(a)-3.18(b) plot the normalized LCRs $L_{|h|}f_1^{-1}$ and AFDs $T_{|h|}f_1$ evaluated from the measurements for the four scenarios (here the subscript for different channels is omitted without confusion). Theoretical expressions of LCRs in (3.5.2), (3.5.4), (3.5.8)

and AFDs in (3.5.3), (3.5.7), (3.5.9) are also plotted for comparisons. The figures indicate that the LCRs and AFDs evaluated from the measurements have close agreement with the theoretical expressions from the designated distributions. For Scenario 1a, scenario-1b, and scenarios 2a, 2b, and 2c, LCR measurements reside in between cascaded Rayleigh with LOS (3.5.4) and Weibull (3.5.8), and same for AFD measurements reside in between (3.5.7) and (3.5.9). For scenarios 3a, 3b the LCRs and AFDs from measurements are close to the theoretical expressions derived in (3.5.8) and (3.5.9) for Weibull distribution.

3.6 Summary

We presented IV2IV, IV2W, and W2W M2M channel measurements in suburban area with dense scattering environments in 1.85GHz. Empirical models for path loss, shadowing, and small-scale fading are studied based on the measurements. The LCR and AFD are verified from the measurements. Depending on the test scenarios, the path loss exponents in the M2M channels are between 3.1 to 4.4 for IV2IV, and lower as 2.4 to 4.7 for IV2W due to the placement of antenna outside the vehicle. The measurements suggest that the mean of shadowing is close to zero, the variance varies from 5 to 6.9 for IV2IV and 3.8 to 5.5 for IV2W. The K-factor was estimated in the range of 0.5 to 0.6 assumes the received small scale component spectral and scatter are very close. The total small scale power is found to be around 2 for all scenarios. The small-scale fading for M2M channels in the suburban dense scattering environment follows Weibull distribution most the time, experiences more sever fading than a single Rayleigh or Rician fading. Some cases, a combination of weibull and cascaded Rayleigh with LOS is closer fit for IV2IV in LOS condition or as shown in Scenario 2c.

CHAPTER 4

M2M STATISTICAL CHANNEL MODELS FOR NON-ISOTROPIC CASCADED-RAYLEIGH WITH LOS

4.1 Literature Review

The main assumption when studying isotropic scattering is angles of arrivals (AOA) and angles of departures (AOD) of scatter components are uniformly distributed around the Tx and Rx. This also suggest the use of omni-antennas at both Tx and Rx. Recent measurements in [8,9] reported non-uniform distributions for AOA and AOD around the Tx and Rx. As a result, It was suggested in [8, 9] that Mobile-to-mobile (M2M) channel can experience Non-isotropic scattering. Although this results in small difference in the first order statistics of the channel model [81]. But, obvious differences can be seen in the second-order channel properties such as auto-, cross-correlations, and rest of correlation properties [81].

Different non-uniform distributions are available for AOA and AOD in a non-isotropic scattering [8, 41–46]. The von Mises [8] distributions was suggested in [9, 47] to represent non-isotropic scattering. It is shown through measurements results in [47] that von Mises distribution has a good fit for AOA. It was also proposed as a choice to approximate other non-uniform distributions. A similar observation is found in [9] while conducting measurements in M2M campaigns in both a highway and an urban area. A 3-D non-isotropic scattering Rician model was proposed in [9]; and a good fit is shown using von Mises distribution with measured LCR and AFD. Other possible distribution are Gaussian [41], Quadrate [42], truncated Laplace [43, 44], truncated uniform [45], and cosine [46].

A 3-D F2M Rician channel under non-isotropic scattering was proposed in [47]. The main work focused on studying the PSD and correlation properties for this type of channel under

non-isotropic condition. A F2M non-isotropic Rayleigh channel model was proposed in [48] using gaussian samples as an input. By adopting the psd in [47], the spectrum shaping filter coefficients in [48] were chosen using an adaptive algorithm to produce the desired spectrum in [47]. A statistical M2M Rician channel model was proposed in [49]. Correlation properties such as auto- and cross-correlations and psd spectrum in [47] were verified.

Non-isotropic scattering was extended to M2M MIMO channels in [50, 51]. Space-time correlation functions were derived in both works. In [51], a statistical channel model with NLOS was proposed based on cascaded-Rayleigh principle under the assumption that AOD and AOA follow von Mises distribution. While a Rician fading geometric channel model was proposed in [50] based on a single-, double-bounced, and a LOS.

In summary, we assume that the AOA and AOD follow von Mises distribution and adopt the technique for calculating these angles from [82]. We present new statistical channel models based on Cascaded-Rayleigh principle with and without LOS. The statistical properties for these M2M non-isotropic channels are derived and verified using monte carlo simulations.

4.2 Existing Simulation Channel models

The reference model which can be found in [51], suggest that at a large distance compared to the Tx and Rx radii, the phase shift of a scatter, θ_{mn} using nth Tx and mth Rx scatter pair, can be divided to two independent phases such as $\theta_{mn} = \theta_m + \theta_n$, where θ_m is the mth Rx scatter phase and θ_n is the nth Tx scatter phase where both are uniformly distributed such as $\theta_m, \theta_n \in (0, 2\pi]$. The Reference simulation model can be expressed as

$$\text{Model I:} \quad s(t) = \frac{1}{\sqrt{PQ}} \sum_{m=1}^{Q} \sum_{n=1}^{P} g_{mn} e^{j(2\pi[f_T(m)\phi_T(m) + f_R(n)\phi_R(n)]t + \theta_m + \theta_n)} \tag{4.2.1}$$

And

$$g_{mn} = a_m b_n c_{mn} \tag{4.2.2}$$

$$a_m = e^{j\pi(\delta_T/\lambda)\cos(\phi_T(m)-\xi_T)} \tag{4.2.3}$$

$$b_n = e^{j\pi(\delta_R/\lambda)\cos(\phi_R(m)-\xi_R)} \tag{4.2.4}$$

$$c_{mn} = e^{j\frac{2\pi}{\lambda}(R_T\cos\phi_T(m)-R_R\cos\phi_R(n))} \tag{4.2.5}$$

$$f_T(m) = f_{T_{max}}\cos(\phi_T(m)-\zeta_T) \tag{4.2.6}$$

$$f_R(n) = f_{R_{max}}\cos(\phi_R(n)-\zeta_R) \tag{4.2.7}$$

where δ_T and δ_R are inter element spacing for MIMO in wavelength. $\phi_T(m)$ and $\phi_R(n)$ are angles of departures and arrivals respectively. ξ_T and ξ_R are tilt angles with respect to the x-axis for Tx and Rx. Ring radii are denoted by R_T and R_R for Tx and Rx. $f_{T_{max}}$ and $f_{R_{max}}$ are the maximum doppler frequencies for Tx and Rx. ζ_T and ζ_R are angles of motion of the Tx and Rx respectively with respect to x-axis.

For single-input-single-output case, using (4.2.1) a statistical channel for cascaded Rayleigh with NLOS can be written in the form

$$y(t) = \sqrt{\frac{\sqrt{2}}{P}}\sum_{n=1}^{P} e^{j\varsigma_n}e^{j\left(2\pi f_1 t\cos(\gamma_n)+\theta_n\right)}\sqrt{\frac{\sqrt{2}}{Q}}\sum_{m=1}^{Q} e^{j\varepsilon_m}e^{j\left(2\pi f_2 t\cos(\beta_m)+\Phi_m\right)} \tag{4.2.8}$$

where $e^{j\varsigma_n}$ and $e^{j\varepsilon_m}$ are the gains of the nth and mth scatters around the Tx and the Rx. f_1 and f_2 are the max Doppler's shift frequencies, γ_n and β_m represent angles of departures and arrivals of the scatters around at Tx and Rx respectively. $\theta_n,\ \Phi_m \ \in [0, 2\pi)$ are phase shifts for each scatter from the Tx and to the Rx respectively, and they are independent, and uniformly distributed for all n and m. Adding the LOS component to (4.2.8), we obtain

a reference model as:

$$\text{Model I-L:}\quad L(t) = \frac{y(t) + \sqrt{2K}e^{j(2\pi f_3 t\cos(\phi_3)+\phi_0)}}{\sqrt{2(1+K)}}, \tag{4.2.9}$$

where K is spectral to scatter powers ratio, ϕ_0 is uniformly distributed random in $[-\pi, \pi)$, f_3 is the Doppler frequency caused by the relative velocity, as both Tx and Rx moving, ϕ_3 is the relative angle between the relative movement and the LOS component.

AOD and AOA are calculated for the Non-Isotropic case using MMEA [51]. Using this method, AOA and AOD can be determined by finding roots of the following

$$\frac{n-\frac{1}{4}}{N} - \int_{\hat{a}_T-\pi}^{\gamma_n} p_\gamma(\gamma)d\gamma = 0, n = 1, 2, .., N \tag{4.2.10}$$

$$\frac{m-\frac{1}{4}}{M} - \int_{\hat{a}_R-\pi}^{\beta_m} p_\beta(\beta)d\beta = 0, m = 1, 2, .., M \tag{4.2.11}$$

where $p_\gamma(\gamma)$ and $p_\beta(\beta)$ follow Von Misses distribution. While $\hat{a}_T,\ \hat{a}_R \in (0, 2\pi]$ are the mean of AOD and AOA respectively. Von Mises distribution was suggested to present AOA and AOD in Non-Isotropic scattering [8]. The probability density function of a Von Mises distribution [83] can be expressed as

$$p_\gamma(\gamma) = \frac{1}{2\pi I_0(\kappa_T)}e^{\kappa_T\cos(\gamma-\hat{a}_T)}, \gamma \in [0, 2\pi) \tag{4.2.12}$$

$$p_\beta(\beta) = \frac{1}{2\pi I_0(\kappa_R)}e^{\kappa_R\cos(\beta-\hat{a}_R)}, \beta \in [0, 2\pi), \tag{4.2.13}$$

where I_0 is the modified Bessel function zero order. κ_T and κ_R are parameters that control the angular spread for γ and β respectively.

4.3 New Simulation Channel models

We begin by taking the advantage of symmetric distribution of Von Mises by choosing $P = 2N$ and $Q = 2M$. Eq. (4.2.8) can be split into two parts $y(t) = y_1(t)y_2(t)$, the Tx

scatter part of $y_1(t) = \sqrt{\frac{\sqrt{2}}{P}} \sum_{n=1}^{P} e^{j\varsigma_n} e^{j\left(2\pi f_1 t \cos(\gamma_n)+\theta_n\right)}$ can be written as

$$y_1(t) = \sqrt{\frac{\sqrt{2}}{2N}} \sum_{n=1}^{N} e^{j\varsigma_n} e^{j\left(2\pi f_1 t \cos(\gamma_n)+\theta_n\right)} + \sqrt{\frac{\sqrt{2}}{2N}} \sum_{n=1}^{N} e^{j\varsigma_{n+N}} e^{j\left(2\pi f_1 t \cos(\gamma_n)+\theta_n\right)} \tag{4.3.1}$$

Making $\varsigma_{n+N} = -\varsigma_n$, applying same approach for $y_2(t) = \sqrt{\frac{\sqrt{2}}{Q}} \sum_{m=1}^{Q} e^{j\varepsilon_m} e^{j\left(2\pi f_2 t \cos(\beta_m)+\Phi_m\right)}$, and $\varepsilon_{m+M} = -\varepsilon_m$, a simulation model for cascaded Rayleigh with NLOS with non-isotropic scattering can be expressed as

$$z(t) = \sqrt{\frac{2\sqrt{2}}{N}} \sum_{n=1}^{N} \cos(\varsigma_n) e^{j\left(2\pi f_1 t \cos(\gamma_n)+\theta_n\right)} \sqrt{\frac{2\sqrt{2}}{Q}} \sum_{m=1}^{Q} \cos(\varepsilon_m) e^{j\left(2\pi f_2 t \cos(\beta_m)+\Phi_m\right)} \tag{4.3.2}$$

4.3.1 Deterministic Channel Model

A deterministic simulation model for cascaded Rayleigh with NLOS with non-isotropic scattering can be expressed as

$$\text{Model II-D:} \quad r(t) = r_1(t) r_2(t) \tag{4.3.3}$$

where $r_1(t)$ and $r_2(t)$ can be written after expanding to their real and imaginary parts, $r_i(t) = r_{ic}(t) + j r_{is}(t),\ i = 1, 2$, where $r_{1c}(t)$ and $r_{1s}(t)$ are defined as:

$$r_{1c}(t) = \sqrt{\frac{2\sqrt{2}}{N}} \sum_{n=1}^{N} \cos(\Theta_n) \cos\left(2\pi f_1 t \cos(\gamma_n) + \theta_n\right) \tag{4.3.4}$$

$$r_{1s}(t) = \sqrt{\frac{2\sqrt{2}}{N}} \sum_{n=1}^{N} \cos(\Theta_n) \sin\left(2\pi f_1 t \cos(\gamma_n) + \theta_n\right), \tag{4.3.5}$$

and $r_{2c}(t)$ and $r_{2s}(t)$ are defined as:

$$r_{2c}(t) = \sqrt{\frac{2\sqrt{2}}{M}} \sum_{m=1}^{M} \cos(\Psi_m) \cos\left(2\pi f_2 t \cos(\beta_m) + \Phi_m\right) \tag{4.3.6}$$

$$r_{2s}(t) = \sqrt{\frac{2\sqrt{2}}{M}} \sum_{m=1}^{M} \cos(\Psi_m) \sin\left(2\pi f_2 t \cos(\beta_m) + \Phi_m\right) \tag{4.3.7}$$

where $\cos(\Theta_n),\ \cos(\Psi_m)$ are weights for each scatter from the Tx and to the Rx respectively, and they are calculated as $\Theta_n = \frac{n\pi-\pi}{8N}$ and $\Psi_m = \frac{m\pi-\pi}{8M}$. $\theta_n,\ \Phi_m \quad \in [0, 2\pi)$ are phase shifts for each scatter from the Tx and to the Rx respectively, and they are independent, and uniformly distributed for all n and m.

4.3.2 Statistical Channel Models

Statistical model with NLOS: We allow the weights to be random to allow faster and better convergence. Using (4.3.4)-(4.3.7), a statistical channel model can be expressed as

$$\text{Model II:}\ \ s(t) = r_1(t)r_2(t) \tag{4.3.8}$$

where $\Theta_n,\ \Psi_m \in [0, \pi)$, $\cos(\Theta_n),\ \cos(\Psi_m)$ are weights for each scatter from the Tx and to the Rx respectively, and they are independent, and uniformly distributed for all n and m.

Statistical model with LOS: A Statistical model using (4.3.8) for cascaded Rayleigh with LOS in non-isotropic scattering can be expressed as

$$\text{Model III:}\ \ \ell(t) = \frac{s(t) + \sqrt{2K}e^{j(2\pi f_3 t\cos(\phi_3)+\phi_0)}}{\sqrt{2(1+K)}} \tag{4.3.9}$$

4.3.3 Second-order statistics

Correlation statistics for Model II Correlation properties for the Non-Isotropic with NLOS can easily derived using the equality$\int_{-\pi}^{\pi} exp(b\sin(x) + c\cos(x))\ dx = 2\pi I_0(\sqrt{b^2+c^2})$ $(eq.3.338-4)$ in [63]. The Auto- and cross-correlation be expressed as

$$R_{r_c r_c}(\tau) = \mathbb{E}\big[r_c(t)r_c(\varrho)\big] = \mathfrak{Re}\Big\{ \prod_{x=T,R} \frac{1}{I_0(\kappa_x)} I_0\big(\sqrt{{\kappa_x}^2 - 4\pi^2\tau^2 f_{x_{max}}^2 + j4\pi\kappa_x\tau f_{x_{max}}\cos(\hat{a}_x)}\ \big) \tag{4.3.10}$$

$$R_{r_s r_c}(\tau) = \mathbb{E}\big[r_s(t) r_c(\varrho)\big] = \mathfrak{Im}\Big\{ \prod_{x=T,R} \frac{1}{I_0(\kappa_x)} I_0\big(\sqrt{{\kappa_x}^2 - 4\pi^2\tau^2 f_{x_{max}}^2 + j4\pi\kappa_x\tau f_{x_{max}} \cos(\hat{a}_x)}\ \big) \tag{4.3.11}$$

$$R_{r_s r_s}(\tau) = \mathbb{E}\big[r_s(t) r_s(\varrho)\big] = R_{r_c r_c}(\tau) \tag{4.3.12}$$

$$R_{r_c r_s}(\tau) = \mathbb{E}\big[r_c(t) r_s(\varrho)\big] = -R_{r_s r_c}(\tau) \tag{4.3.13}$$

$$R_{rr}(\tau) = \frac{1}{2}\mathbb{E}\big[r^*(t) r(\varrho)\big] = \frac{1}{2}\big(R_{r_c r_c}(\tau) + R_{r_s r_s}(\tau) - jR_{r_c r_s}(\tau) + jR_{r_s r_c}(\tau)\big) \tag{4.3.14}$$

where $\mathfrak{Re}$ and $\mathfrak{Im}$ are real and imaginary parts, $\prod$ is the product function. When $\kappa_T = \kappa_R = 0$, the autocorrelation becomes $R_{r_c r_c}(\tau) = J_0(2\pi f_1\tau)J_0(2\pi f_2\tau)$, while the cross-correlation becomes $R_{r_c r_s}(\tau) = 0$

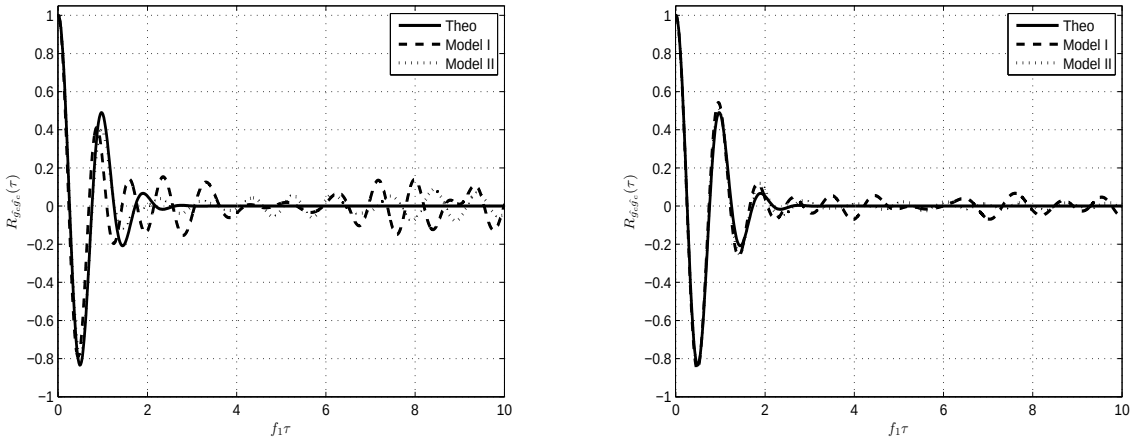

(a) Autocorrelation with 1 trial

(b) Autocorrelation with 3 trials

Figure 4.1: Autocorrelation of No-Isotropic, MMEA, $\kappa = 40$, $M = 50$, $N = M + 2$, $t = 2$ sec

Correlation statistics for Model III The Autocorrelation, Cross correlation, and autocorrelation of the complex envelopes for the Non-Isotropic with LOS can be expressed as

$$R_{\ell_c\ell_c}(\tau) = \mathbb{E}\big[\ell_c(t)\ell_c(t+\tau)\big] = \frac{R_{r_c r_c}(\tau) + K\cos\big(2\pi f_3\tau\cos(\phi_3)\big)}{2(1+K)} \tag{4.3.15}$$

TABLE 4.1:

MODELS CONVERGENCE

Model	Mean error	Mean square error
Model I ACF	1.26×10^{-2}	4.1268×10^{-4}
Model I CCF	1.32×10^{-2}	4.4673×10^{-4}
Model II ACF	8.80×10^{-3}	1.7618×10^{-4}
Model II CCF	9.30×10^{-3}	1.9832×10^{-4}

$$R_{\ell_s\ell_c}(\tau) = \mathbb{E}\big[\ell_s(t)\ell_c(t+\tau)\big] = \frac{R_{r_sr_c}(\tau) + K\sin\big(2\pi f_3\tau\cos(\phi_3)\big)}{2(1+K)} \tag{4.3.16}$$

$$R_{\ell_s\ell_s}(\tau) = \mathbb{E}\big[\ell_s(t)\ell_s(t+\tau)\big] = R_{\ell_c\ell_c}(\tau) \tag{4.3.17}$$

$$R_{\ell_c\ell_s}(\tau) = \mathbb{E}\big[\ell_c(t)\ell_s(t+\tau)\big] = -R_{\ell_s\ell_c}(\tau) \tag{4.3.18}$$

$$R_{\ell\ell}(\tau) = \frac{1}{2}\mathbb{E}\big[\ell^*(t)\ell(t+\tau)\big] = \frac{R_{rr}(\tau) + Ke^{j2\pi f_3\tau\cos(\phi_3)}}{1+K} \tag{4.3.19}$$

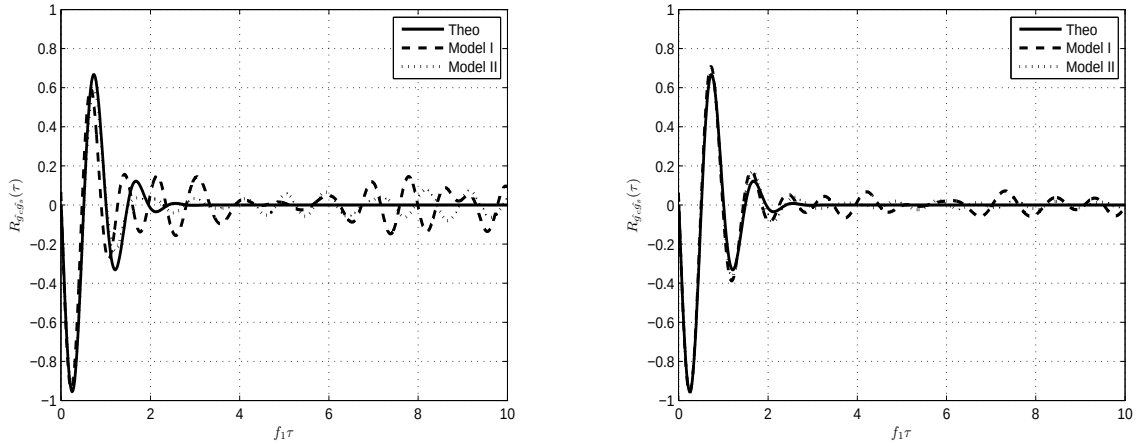

(a) Cross-correlation with 1 trial

(b) Cross-correlation with 3 trials

Figure 4.2: Cross-correlation of No-Isotropic, MMEA, $\kappa = 40$, $M = 50$, $N = M + 2$, $t = 2$ sec

4.4 Simulations Results

4.4.1 Correlation Analysis

The Auto- and cross-correlation comparisons in 1 and 3 trials between the reference model I and the proposed model II are shown in Figs. 4.1 and 4.2. The results were obtained for No-Isotropic using MMEA, $\kappa = 40$, $Q = M = 50$, $P = N = M + 2$, $t = 2$ sec. It can be observed that the proposed model has a better convergence even in 1 trial as shown in Figs. 4.1(a) and 4.2(a). Results in Figs. 4.1(b) and 4.2(b) show an even identical match for Model II in contrast to the reference model. In Table. 4.5, a models convergence study is shown using a total number of 50 trials. The MSE is reduced by half for Model II in compare with Model I.

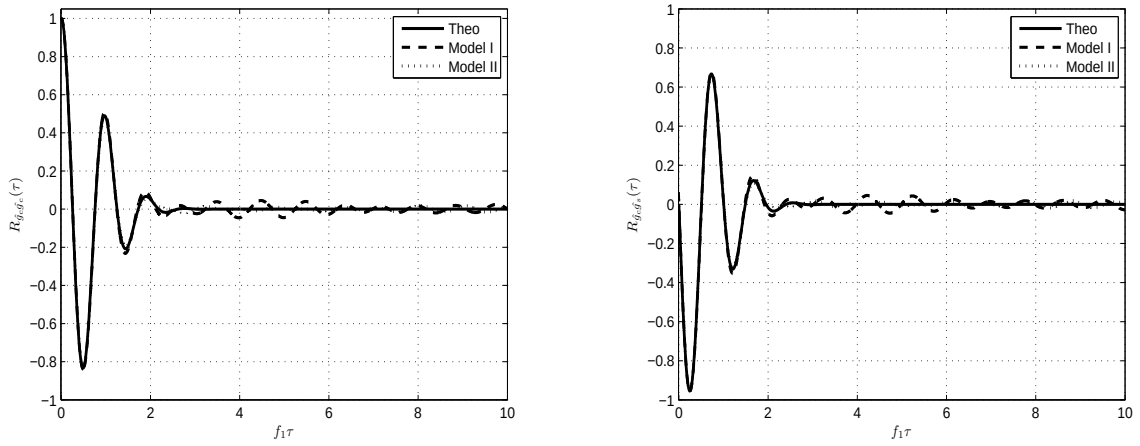

(a) Autocorrelation with 50 trials Comparison

(b) Cross-correlation with 50 trials Comparison

Figure 4.3: Comparison of Auto-correlation and Cross-correlation of No-Isotropic, MMEA, $\kappa = 40$, $M = 50$, $N = M + 2$, $t = 2$ sec

Figs. 4.4(a) and 4.4(b) show the mean absolute errors (MAE) of auto- and cross correlations of Models I and II. The MAE in autocorrelation is obtained using a total number of

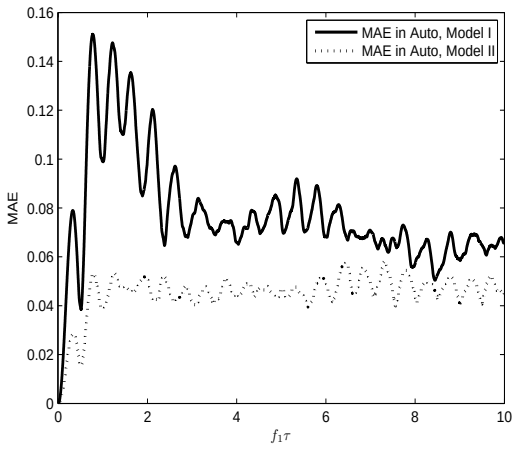

(a) MAE in Autocorrelation with 50 trials

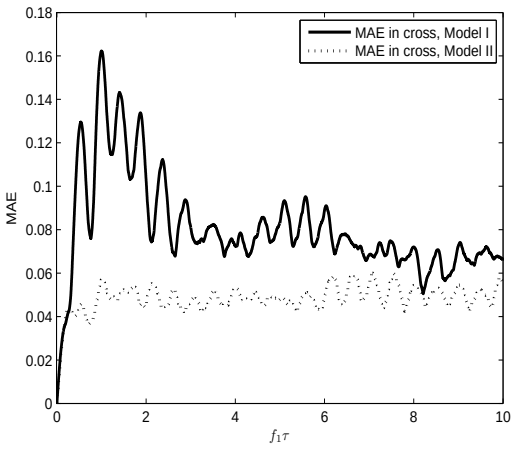

(b) MAE in Cross-correlation with 50 trials

Figure 4.4: MAE of auto- and cross correlations of Models I and II in No-Isotropic, MMEA, $\kappa = 40$, $M = 50$, $N = M + 2$, $t = 2$ sec

$\triangle = 50$ trials as $\frac{1}{2\triangle}\sum_{k=1}^{\triangle} |\hat{R}_{r_c r_c}(\tau) - R_{r_c r_c}(\tau)| + |\hat{R}_{r_s r_s}(\tau) - R_{r_s r_s}(\tau)|$, while cross correlation MAE is obtained as $\frac{1}{2\triangle}\sum_{k=1}^{\triangle} |\hat{R}_{r_c r_s}(\tau) - R_{r_c r_s}(\tau)| + |\hat{R}_{r_s r_c}(\tau) - R_{r_s r_c}(\tau)|$, where $\hat{R}_{r_c r_c}(\tau)$, $\hat{R}_{r_s r_s}(\tau)$, $\hat{R}_{r_c r_s}(\tau)$, and $\hat{R}_{r_s r_c}(\tau)$ are the simulated autocorrelations and cross correlations.

4.4.2 Power Spectrum Analysis

In this section, we study effects of different parameters on the channel behavior, such as K, κ_x, and $\hat{a}_x$, where $x = T,\ R$. The Doppler power spectrum $S_{hh}(f)$ for (4.3.9) and (4.2.9) can be obtained by calculating the fourier transform of (4.3.19). Numerical integration was used in these simulations as their is no closed form for it. The results were obtained using $N = 200000$ samples and 40 trials for Model IV. The doppler frequency spectrum was normalized to the f_1. Scatter gains were normalized as $\varsigma_n = \varepsilon_m = 0$ for all n, m.

- **Effect of K:** Fig (4.6), illustrates the effect of different K on the doppler frequency spectrum. The result was obtained as an average of 40 trials, where $\kappa = 2$, and

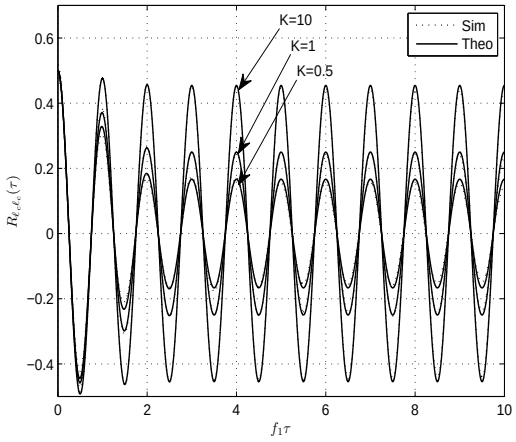

(a) Autocorrelation with 3 trials for Model II

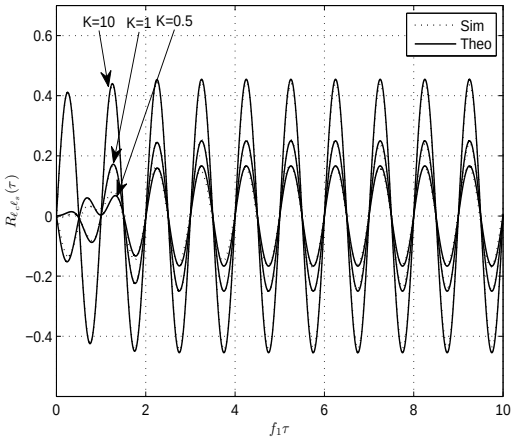

(b) Cross-correlation with 3 trials for Model II

Figure 4.5: Auto- and cross correlations for Model II in No-Isotropic, MMEA, $\kappa = 40$, $M = 50$, $N = M + 2$, $t = 2$ sec

$\hat{a}_T = \hat{a}_R = 0$. It can be observed that the asymmetric shape of the doppler spectrum which resulted from the scatter non-isotropic in starts loosing its its component at $f_1 + f_2$ as K increases. While the peak at $-f_1$, resulted from spectral component, is very close for all K.

- **Effect of κ_x:** The effect of the angular spread is shown in Fig. (4.7). The power spectrum is shown for different κ with $\hat{a}_T = \hat{a}_R = 0$, $K = 1$ using an average of 40 trials. It is clear as κ increases, the power component at $f_1 + f_2$ increases. This suggests that at high κ, the component of the scatter is more focused.

- **Effect of $\hat{a}_x$:** Different mean of AOD and AOA are shown in Fig. (4.8) using $K = 0$, and $\kappa = 2$, in average of 40 trials. The effect of on the the spectrum is by shifting it from right to left or vise versa around the carrier frequency.

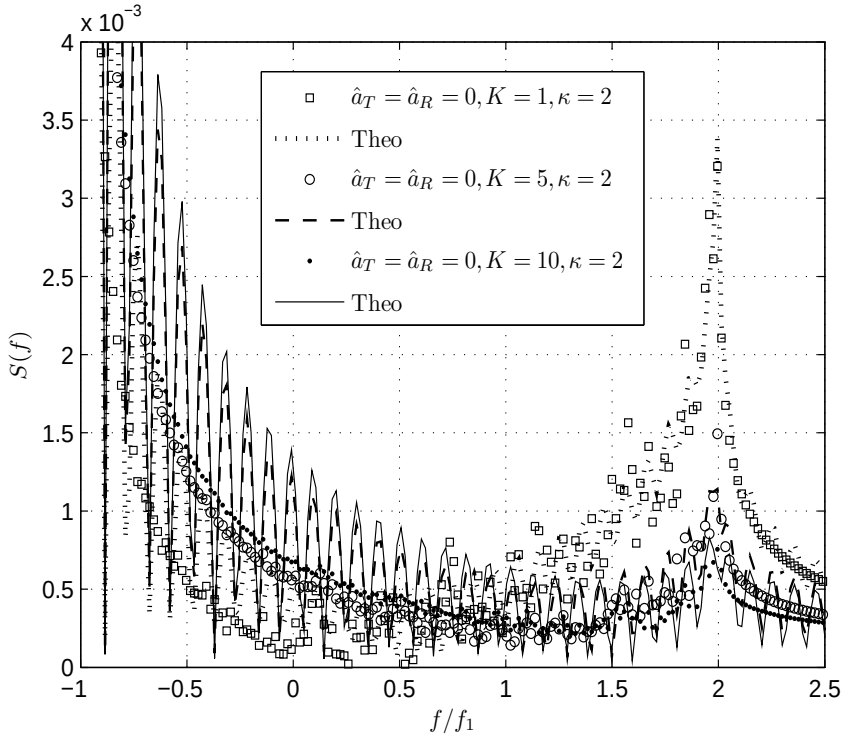

Figure 4.6: Model I-L: Power spectrum for different K, $\kappa = 2$, $\hat{a}_T = \hat{a}_R = 0$ in 40 trials

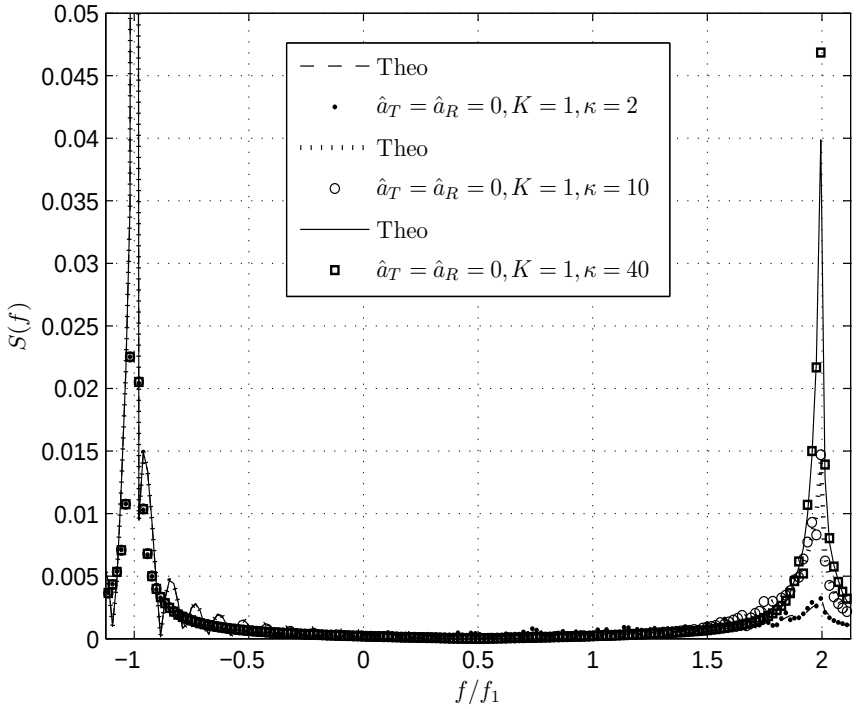

Figure 4.7: Model I-L: Power spectrum for different κ, $\hat{a}_T = \hat{a}_R = 0$, $K = 1$, in 40 trials

4.5 Summary

In this chapter, we presented statistical channel models based on Cascaded-Rayleigh with and without LOS for M2M scenario in non-isotropic scattering environment. We assumed that the AOA and AOD follow von Mises distribution as suggested in published measurements. The statistical properties for these proposed channel models are derived and verified using monte carlo simulations.

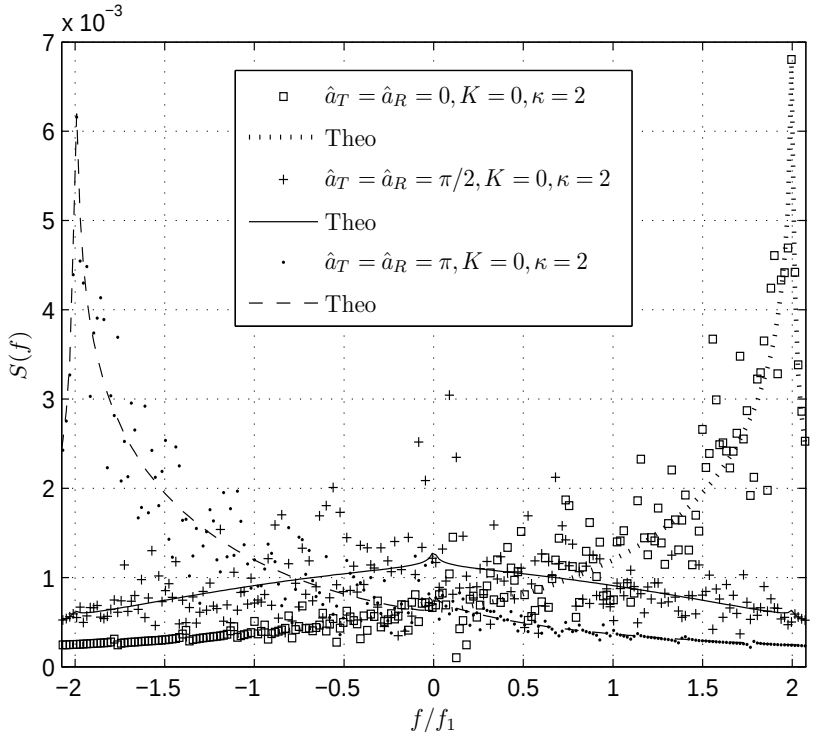

Figure 4.8: Model I-L: Power spectrum for different $\hat{a}_T$ and $\hat{a}_R$, $K = 0$, and $\kappa = 2$, in 40 trials

Models convergence was tested using MSE similarly to isotropic channels. While stability of the proposed models was tested using MAE of auto and cross correlations. The fourier transform or the psd of the auto- and cross correlations for proposed channel models brought

additional dimension to the study. The psd show asymmetric channel frequency response with respect to the carrier frequency in contrast to F2M and M2M in isotropic. And different psd in compare with F2M in non-isotropic environment.

4.6 Supplemental Material

The distribution is Rayleigh for M2M non-isotropic as shown in [49]. The proposed simulation channel model can be written as

$$u(t) = u_c(t) + ju_s(t) \tag{4.6.1}$$

$$u_c(t) = \sum_{n=1}^{M} B_n(t)\cos[2\pi(C_{1,n} + C_{2,n})t + \phi_n] \tag{4.6.2}$$

$$u_s(t) = \sum_{n=1}^{M} B_n(t)\sin[2\pi(C_{1,n} + C_{2,n})t + \phi_n] \tag{4.6.3}$$

where

$$B_n(t) = \sqrt{\frac{2}{M}}\cos[2\pi(S_{1,n} + S_{2,n})t + \hat{\phi}_n] \tag{4.6.4}$$

$$C_{i,n} = f_{d_i}\cos\mu_i\cos\beta_{i,n}, \qquad i = 1,..,I \tag{4.6.5}$$

$$S_{i,n} = f_{d_i}\sin\mu_i\sin\beta_{i,n}, \qquad i = 1,..,I \tag{4.6.6}$$

$$\tag{4.6.7}$$

N is the number of propagation paths. $M = N/2$ is the number of sinusoids, f_{d_i} are the max doppler frequencies. eg. f_{d_1}, f_{d_2} for the Tx and Rx respectively. And the random variables are independent for all n and distributed as

$$\beta_{1,n} \sim M(0,\kappa_1), \beta_{2,n} \sim M(0,\kappa_2) \tag{4.6.8}$$

$$\phi_n \sim U[-\pi,\pi], \hat{\phi}_n \sim U[-\pi,\pi] \tag{4.6.9}$$

von Mises AOD is $M(\mu_1, \kappa_1)$ and AOA is $M(\mu_2, \kappa_2)$, where μ_1 and μ_2 are the mean direction of AOD and AOA respectively. This model as shown in [49] requires a high number of sinusoids, $M = 140$ was used to get close results to theoretical.

CHAPTER 5

CONCLUSION AND FUTURE WORK

5.1 Statistical Models

M2M communications have gained researchers attention recently. Rapidly growing mobile applications where nodes are no longer fixed, such as ad-hoc networks, WLAN, and V2V are motivating researchers to study these channels and understand its statistical properties. Earlier versions of channel models are not suitable for all M2M communications scenarios. Users are likely to have outdoor-to-indoor conversations, such as outdoor Tx to indoor Rx inside a car or a building, or move in a dense scattering environment, such as in suburban streets or forest, or between buildings.

In this work, we proposed new statistical channel models based on two cascaded Raleigh principle with and without LOS. These models are designed for such M2M in dense scattering environments where the received signal experience severe fading such as scattering due to trees in forest, diffracting at building edges and streets corners, or in an outdoor-to-indoor scenario.

Extensive Monte Carlo simulations are performed for various statistical properties to validate the proposed models. Results show that the proposed models converge very well to all desired properties, including the PDF, various auto- and cross-correlations, LCR, and AFD. The new proposed models converge fast to its required statistical properties; require small number of trials and have low complexity in terms of design, which was key objective in our work. Due to the lack of similar cascaded Rayleigh models, and to test its complexity and fast convergence, we simulated another existing model, double-ring model, for complexity

comparison purpose although it is used for different catagories of M2M channels. We showed that the proposed models can achieve the desired statistical properties using $M+N$ sinusoids compared to a total of MN sinusoids required for double-ring model.

Weibull fading statistical channel models are very limited in the literature. The work in this dissertation suggested that this distribution is a better fit than mainly known distribution as Rician. This distribution and its statistical properties provide more understanding of channel behavior in dense scattering environments.

5.2 Empirical Models

Earlier measurements did not study all M2M communications scenarios. Users are likely to have outdoor-to-indoor or IV2W or IV2IV conversations in dense scattering environments such as suburban streets or forest/high-dense of trees, or experiencing a key-hole effect.

In this work, we presented M2M measurements without and with visibility in the 2.1GHz and 700MHz bands. Measurements of IV2IV and IV2W were conducted in a highly dense scattering environments. Different locations were selected in northern new Jersey where rainforest trees exist heavily.

New empirical models were proposed for path loss, shadowing, and small-scale fading. The statistical properties such as first-order, second-order are studied for these data sets of measurements. Studying small-scale had a great attention in this study. Different distributions were used to try ft the data. Weighted sum of single and double Rayleigh was also used in attempt to represent the channel envelope. It is shown in forest environments, that cascaded Rayleigh with LOS, and a combination of %80 Cascaded with LOS and %20 of Rician distribution had the closest fit to the measured data envelope . The weibull distribution

was found as the best fit distribution for suburban IV2IV and IV2W scenarios.

W2W channel measurements seems to have no attention in the literature. With availability of portable transmitters and receivers, old limitations of equipment size and power supplies are no longer issues.

Measurements in the 700Mhz band can be extended to farther distances. This will provide more insight on path loss in this band. No measurements of IV2IV were conducted in the 700Mhz band in this work. This can be a potential case study in M2M field measurements.

5.3 Non-isotropic Models

In this work, we proposed new statistical channel models for M2M channels based on Cascaded-Rayleigh fading with and without LOS in a non-isotropic scattering. We adopted MMEA method for calculating AOAs and AODs under the assumption that these angles follow von Mises distribution. This choice of distributions was selected among other proposed ones in the literature as supported with recent measurements.

The statistical properties for the proposed models are derived and verified using monte carlo simulations. Simulations show good agreement between simulated models and its theoretical. The MSE and MAE were used to test convergence and stability of the new models. The frequency spectrum of the proposed models provided a better understanding of key parameters of these models such as mean of AOA and AOD, spectral to scatter ratio, and the spread factor around the mean. The psd show asymmetric channel frequency response in contrast to isotropic channels.

The available literature on Non-isotropic is limited and there is a plenty of room to present new models. Other Worse-than-Rayeligh in Non-isotropic are potential distribution

to be studied. More comprehensive M2M channel measurement campaigns using directional antennas are needed to better understand these types of channels.

REFERENCES

REFERENCES

[1] P. Buccio, E. Masala, N. Kawaguchi, K. Takeda, and J. C. De Martin, "Performance evaluation of H. 264 video streaming over inter-vehicular 802.11 ad hoc networks," in *Proc. IEEE Symp. on Personal, Indoor and Mobile Radio Commun.*, Berlin, Germany, Sept. 2005, vol. 3, pp. 1936–1940.

[2] J. Ott and D. Kutscher, "The drive-thru architecture: WLAN-based Internet access on the road," in *Proc. IEEE Veh. Technol. Conf.*, Milan, Italy, May 2004, vol. 5, pp. 2615–2622.

[3] Z. Jing and S. Roy, "MAC for dedicated short range communications in intelligent transport system," *IEEE Commun. Mag.*, vol. 41, no. 12, pp. 60–67, Dec. 2003.

[4] S. Dashtinezhad, "Traffic view: A driver assistant device for traffic monitoring based on car-to-car communication," in *Proc. IEEE Veh. Technol. Conf.*, Milan, Italy, May 2004, vol. 5, pp. 2946–2950.

[5] S. Biswas, R. Tatchikou, and F. Dion, "Vehicle-to-vehicle wireless communication protocols for enhancing highway traffic safety," *IEEE Commun. Mag.*, vol. 44, no. 1, pp. 74–82, Jan. 2006.

[6] Y. Zang, L. Stibor, G. R. Hiertz, and H. J. Reumerman, "Vehicular Wireless Media Network (VWMN) - A distributed broadband MAC for inter-vehicle communication," in *Proc. ACM Int. Wksp. Veh. Ad Hoc Netw.*, Cologne, Germany, Sept. 2005, pp. 95–96.

[7] T. J. Harrold and A. R. Nix, "Capacity enhancement using intelligent relaying for future personal communication systems," in *Proc. IEEE Veh. Technol. Conf.*, Boston, MA, Sept. 2000, vol. 5, pp. 2115–2120.

[8] A. Abdi and M. Kaveh, "A space-time correlation model for multielement antenna systems in mobile fading channels," *IEEE J. Sel. Areas Commun.*, vol. 20, no. 3, pp. 550–560, Apr. 2002.

[9] A. G. Zajic, G. L. Stüber, T. G. Pratt, and S. Nguyen, "Envelope level crossing rate and average fade duration in mobile-to-mobile fading channels," in *Proc. IEEE Int. Conf. on Commun.*, Beijing, May 2008, pp. 4446–4450.

[10] M. Pätzold, U. Killat, F. Laue, and Y. Li, "On the statistical properties of deterministic simulation models for mobile fading channels," *IEEE Trans. Veh. Technol.*, vol. 47, no. 1, pp. 254–269, 1998.

[11] M. Pätzold, B. Hogstad, and D. Kim, "A new design concept for highperformance fading channel simulators using set partitioning," *Wireless Personal Commun.*, vol. 40, no. 2, pp. 267–279, Feb. 2007.

[12] A. Akki and F. Haber, "A statistical model for mobile to-mobile land communication channel," *IEEE Trans. Veh. Technol.*, vol. 35, pp. 2–10, Feb. 1986.

[13] A. Akki, "Statistical properties of mobile-to-mobile land communication channels," *IEEE Trans. Veh. Technol.*, vol. 43, pp. 826–831, Nov . 1994.

[14] C. Patel, G. Stüber, and T. Pratt, "Simulation of Rayleigh-faded mobile-to-mobile communication channels," *IEEE Trans. Commun.*, vol. 53, pp. 1876–1884, Nov. 2005.

[15] A. Zajic and G. Stüber, "A new simulation model for mobile-to-mobile Rayleigh fading channels," in *Proc. IEEE Wireless Commun. Netw. Conf.*, Las Vegas, NV, Apr. 2006, vol. 3, pp. 1266–1270.

[16] Y. Zheng and C. Xiao, "Improved models for the generation of multiple uncorrelated Rayleigh fading waveforms," *IEEE Commun. Lett.*, vol. 6, no. 6, pp. 256–258, Jun. 2002.

[17] L. Wang, W. Liu, and Y. Cheng, "Statistical analysis of a mobile-to-mobile Rician fading channel model," *IEEE Trans. Veh. Technol.*, vol. 58, no. 1, pp. 32–38, Jan. 2009.

[18] C. Xiao and Y. R. Zheng, "A statistical simulation model for mobile radio fading channels," in *Proc. IEEE Wireless Commun. Netw. Conf.*, New Orleans, LA, Mar. 2003, vol. 1, pp. 144–149.

[19] C. Xiao and Y. R. Zheng, "Novel sum-of-sinusoids simulation models for Rayleigh and Rician fading channels," *IEEE Trans. Wireless Commun.*, vol. 5, no. 12, pp. 3667–3679, Dec. 2006.

[20] D. Matolak, I. Sen, W. Xiong, and N. Yaskoff, "5 GHz wireless channel characterization for vehicle to vehicle communications," in *Proc. IEEE Military Commun. Conf.*, Atlantic City, NJ, Oct. 2005, vol. 5, pp. 3016–3022.

[21] I. Sen and D. Matolak, "Vehicle-vehicle channel models for the 5-GHz band," *IEEE Trans. Intell. Transp. Syst.*, vol. 9, no. 2, pp. 235–245, Jun. 2008.

[22] A. Paier, J. Karedal, N. Czink, H. Hofstetter, C. Dumard, T. Zemen, F. Tufvesson, A. Molisch, and C. Mecklenbrauker, "First results from car-to-car and car-to-infrastructure radio channel measurements at 5.2GHz," in *Proc. IEEE Int. Symp. on Personal Indoor and Mobile Radio Commun.*, Athens, Greece, Sept. 2007, vol. 1, pp. 1–5.

[23] I. Kovächs, P. Eggers, K. Olesen, and L. Patersen, "Investigations of outdoor-to-indoor mobile-to-mobile radio communication channels," in *Proc. IEEE Veh. Technol. Conf.*, Vancouver, Canada, May 2002, vol. 1, pp. 430–434.

[24] J. Maurer, T. Fugen, and W. Wiesbeck, "Narrow-band measurement and analysis of the inter-vehicle transmission channel at 5.2 GHz," in *Proc. IEEE Veh. Technol. Conf.*, Birmingham, AL, May 2002, vol. 3, pp. 1274–1278.

[25] V. Erceg, S. Fortune, J. Ling, A. Rustako, and R. Valenzuela, "Comparisons of a computer-based propagation prediction tool with experimental data collected in urban microcellular environments," *IEEE Journal Sel. Areas Commun.*, vol. 15, no. 4, pp. 677–684, May 1997.

[26] J. B. Andersen, "Statistical distributions in mobile communications using multiple scattering," in *Proc. 27th URSI Gen. Assem. of Int. Union of Radio Sci.*, Maastricht, Netherlands, Aug. 2002.

[27] J. B. Andersen and I. Z. Kovächs, "Power distributions revisited," in *Proc. COST273, Towards Mobile Broadband Multimedia Netw.*, Guildford, UK, Jan. 2002, TD (02)004.

[28] D. W. Matolak, F.-C. Yang, and H. B. Riley, "Short range forest channel modeling in the 5 GHz band," in *Proc. IEEE Euro. conf. on Anten. and Prop.*, Athens, OH, Mar. 2012, pp. 3337–3341.

[29] Q. Wu, D. W. Matolak, and I. Sen, "5-GHz-band vehicle-to-vehicle channels: Models for multiple values of channel bandwidth," *IEEE Trans. Veh. Technol.*, vol. 59, no. 5, pp. 2620–2625, June 2010.

[30] H. Iwai and S. Goto, "Multipath delay profile models for ITS in 700MHz band," in *Proc. IEEE Veh. Technol. Conf.*, Kyoto, Japan, Sept. 2011, pp. 1–5.

[31] R. Sevlian, C. Chun, I. Tan, A. Bahai, and K. Laberteaux, "Channel characterization for 700MHz DSRC vehicular communication," *Journal of Elect. Comp. Eng.*, vol. 2010, no. 840895, pp. 1–9, Jul. 2010.

[32] L. Cheng, B. E. Henty, D. D. Stancil, F. Bai, and P. Mudalige, "Mobile vehicle-to-vehicle narrow-band channel measurement and characterization of the 5.9 GHz dedicated short range communication (DSRC) frequency band," *IEEE Journal Sel. Areas Commun.*, vol. 25, no. 8, pp. 1501–1516, Oct. 2007.

[33] T. S. Rappaport, *Wireless Communications: Principles and Practice*, Prentice Hall, 2nd edition, Dec. 2001.

[34] C. F. Mecklenbrauker, A. F. Molisch, J. Karedal, F. Tufvesson, A. Paier, L. Bernado, T. Zemen, O. Klemp, and N. Czink, "Vehicular channel characterization and its implications for wireless system design and performance," *Proc. IEEE*, vol. 99, no. 7, pp. 1189–1212, Jul. 2011.

[35] J. Karedal, N. Czink, A. Paier, F. Tufvesson, and A. F. Molisch, "Path loss modeling for vehicle-to-vehicle communications," *IEEE Trans. Veh. Technol.*, vol. 60, no. 1, pp. 323–328, 2011.

[36] G. L. Stüber, *Principles of Mobile Communication*, Kluwer Academic Pulishrs, 2nd edition, Dec. 2001.

[37] COST235, *Radio propagation effects on next-generation fixed-service terrestrial telecommunication systems*, Final Report, Luxembourg, 1996.

[38] M. A. Weissberger, *An initial critical summary of models for predicting the attenuation of radio waves by trees*, Rep. ESD-TR-81-101, Electromagnetic Compatibility Analysis Center, Annapolis, MD, Jul. 1982.

[39] M. O. Al-Nuaimi and R. B. L. Stephens, "Measurements and prediction model optimization for signal attenuation in vegetation media at centimetre wave frequencies," *IEE Proc. Microw. Antennas Propag.*, vol. 145, no. 3, pp. 201–206, 1998.

[40] Y. S. Meng, Y. H. Lee, and B. C. Ng, "Empirical near ground path loss modeling in a forest at VHF and UHF bands," *IEEE Trans. Antennas Propag.*, vol. 57, no. 5, pp. 1461–1468, May 2009.

[41] J. Salz and J. H. Winters, "Effect of fading correllation on adaptive arrays in digital-mobile radio," *IEEETrans. Veh. Technol.*, vol. 43, pp. 1049–1057, 1994.

[42] K. Anim-Appiah, "Complex envelope correlations for nonisotropic scattering," *IEEE Electron. Lett.*, vol. 34, pp. 918–919, 1998.

[43] Ed. L. M. Correia, *Wireless Flexible Personalised Communications*, John Wiley & Sons, Ltd, 2001.

[44] Q. Spencer, M. Rice, B. Jeffs, and M. Jensen, "A statistical model for angle of arrival in indoor multipath propagation," in *Proc. IEEE Veh. Technol. Conf.*, Phoenix, AZ, 1997, pp. 1415–1419.

[45] J. Salz and J. H. Winters, "Effect of fading correlation on adaptive arrays in digital mobile radio," *IEEE Trans. Veh. Technol.*, vol. 43, no. 4, pp. 1049–1057, Nov. 1994.

[46] M. D. Austin and G. L. Stüber, "Velocity adaptive handoff algorithms for microcellular systems," *IEEE Trans. Veh. Technol.*, vol. 43, pp. 549–561, 1994.

[47] A. Abdi, J. A. Barger, and M. Kaveh, "A parametric model for the distribution of the angle of arrival and the associated correlation function and power spectrum at the mobile station," *IEEE Trans. Veh. Technol*, vol. 51, no. 3, pp. 425–434, MAY 2002.

[48] A. Alimohammad, S. F. Fard, and B. F. Cockburn, "Accurate simulation of non-isotropic fading channels with arbitrary temporal correlation," *IET Commun.*, vol. 6, no. 5, pp. 557–564, 2012.

[49] Y. R. Zheng, "A non-isotropic model for mobile-to-mobile fading channel simulations," in *Proc. IEEE Military Commun. Conf.*, Oct. 2006, pp. 1–6.

[50] X. Cheng, C-X. Wang, D. Laurenson, S. Salous, and A. V. Vasilakos, "An adaptive geometry-based stochastic model for non-isotropic MIMO mobile-to-mobile channels," *IEEE Trans. Wireless Commun.*, vol. 8, no. 9, pp. 4824–4835, Sept. 2009.

[51] M. Pätzold, B. O Hogstad, and N. Youssef, "Modeling, analysis, and simulation of MIMO mobile-to-mobile fading channels," *IEEE Trans. Wireless Commun.*, vol. 7, no. 2, pp. 510–520, Feb. 2008.

[52] Y. Ibdah, Y. Ding, H. M. Kwon, and K. Lee, "Simulations on the statistical properties for cascaded Rayleigh fading channel," in *Proc. IEEE Military Commun. Conf.*, Baltimore, MD, Nov. 2011, pp. 435–440.

[53] D. W. Matolak, "Channel modeling for vehicle-to-vehicle communications," *IEEE Commun. Mag.*, vol. 46, no. 5, pp. 76–83, May 2008.

[54] G. Acosta-Marum and M. A. Ingram, "Six time- and frequency- selective empirical channel models for vehicular wireless LANs," *IEEE Veh. Technol. Mag.*, vol. 2, no. 4, pp. 4–11, Dec. 2007.

[55] F. Vatalaro and A. Forcella, "Doppler spectrum in mobile-to-mobile communications in the presence of three-dimensional multipath scattering," *IEEE Trans. Veh. Technol*, vol. 46, no. 2, pp. 213–219, Feb. 1997.

[56] B. Talha and M. Pätzold, "A geometrical three-ring-based model for MIMO mobile-to-mobile fading channels in cooperative networks," in *Proc. IEEE Veh. Technol. Conf.*, Barcelona, Spain, Apr. 2009, vol. 1, pp. 1–7.

[57] D. W. Matolak and J. Frolik, "Worse-than-Rayleigh fading: Experimental results and theoretical models," *IEEE Commun. Mag.*, vol. 49, no. 4, pp. 140–146, Apr. 2011.

[58] C. Xiao and Y. R. Zheng, "Simulation models with correct statistical properties for Rayleigh fading channels," *IEEE Trans. Commun.*, vol. 53, no. 6, pp. 920–928, Jun. 2003.

[59] S. Koltz, T. J. Kozubowski, and K. Podgorski, *The Laplace Distribution and Generalizations: A Revisit with Applications to Communications, Economics, Engineering, and Finance.*, Springer-Verlag New York, Birkhauser, 1st edition, May 2001.

[60] B. Talha and M. Pätzold, "Statistical modeling and analysis of mobile-to-mobile fading channels in cooperative networks under line-of-sight condition," *Wireless Pers. Commun.*, vol. 54, no. 1, pp. 3–19, Apr. 2009.

[61] G. Karagiannidis, N. Sagias, and P. Mathiopoulos, "N-nakagami: A novel stochastic model for cascaded fading channels," *IEEE Trans. Commun.*, vol. 55, no. 8, pp. 1453–1458, Aug. 2007.

[62] Z. Velkov, N. Zlatanov, and G Karagiannidis, "On the second order statistics of the multihop Rayleigh fading channel," *IEEE Trans. Commun.*, vol. 57, no. 6, pp. 1815–1823, Jun. 2009.

[63] I. Gradshteyn and I. Ryzhik, *Table of Integrals, Series, and Products*, Academic Press, 7th edition, 2007.

[64] A. G. Zajic and G. L. Stüber, "Space-time correlated mobile-to-mobile channels: modeling and simulation," *IEEE Trans. Veh. Technol.*, vol. 57, no. 2, pp. 715–726, Mar. 2008.

[65] D. Gesbert, H. Bölcskei, D. A. Gore, and A. J. Paulraj, "Outdoor MIMO wireless channels: Models and performance prediction," *IEEE Trans. Commun.*, vol. 50, pp. 1926–1934, Dec. 2002.

[66] X. Cheng, C.-X. Wang, D. I. Laurenson, and A. V. Vasilakos, "Second order statistics of non-isotropic mobile-to-mobile Ricean fading channels," in *Proc. IEEE Conf. Commun.*, Dresden, Germany, Jun. 2009, pp. 14–18.

[67] A. Paier, J. Karedal, N. Czink, C. Dumard, T. Zemen, F. Tufvesson, A. F. Molisch, and C. F. Mecklenbruker, "Characterization of vehicle-to-vehicle radio channels from measurements at 5.2GHz," *Wireless Pers. Commun.*, vol. 50, no. 1, pp. 19–32, Jul. 2009.

[68] C. Hill and T. Kneisel, "Portable radio antenna performance in the 150, 450, 800, and 900 MHz bands outside and in-vehicle," *IEEE Trans. Veh. Technol.*, vol. 40, no. 4, pp. 750–756, Nov. 1991.

[69] E. Tanghe, W. Joseph, L. Verloock, and L. Martens, "Evaluation of vehicle penetration loss at wireless communication frequencies," *IEEE Trans. Veh. Technol.*, vol. 57, no. 4, pp. 2036–2041, Jul. 2008.

[70] I. Kostanic, C. Hall, and J. McCarthy, "Measurements of the vehicle penetration loss characteristics at 800MHz," in *Proc. IEEE Veh. Technol. Conf.*, Ottawa, Ont, May 1998, vol. 1, pp. 1–4.

[71] W. Gellert, S. Gottwald, M. Hellwich, H. Kästner, and H. Küstner, *The VNR Concise Encyclopedia of Mathematics*, Springer, 2nd edition, Feb. 1990.

[72] S. Shekhar and H. Xiong, *Encyclopedia of GIS*, Springer, 1st edition, Dec. 2007.

[73] R. W. Sinnott, "Virtues of the haversine," *Sky and Telescope*, vol. 68, no. 2, pp. 158–159, 1984.

[74] CCIR, *Influences of terrain irregularities and vegetation on troposphere propagation*, CCIR Report, Geneva, 1986.

[75] J. Goldman and Jr. G. W. Swenson, "Radio wave propagation through woods," *IEEE Mag. Antennas Propag.*, vol. 41, no. 5, pp. 34–36, 1999.

[76] Y. S. Meng, Y. H. Lee, and B. C. Ng, "Near ground channel characterization and modeling for a tropical forested path," in *Proc. URSI General Assembly*, Chicago, IL, 2008.

[77] Andreas F. Molisch, *Wireless Communications*, John Wiley & Sons Ltd, 2nd edition, Dec. 2010.

[78] L. Bernado, T. Zemen, J. Karedal, A. Paier, A. Thiel, O. Klemp, N. Czink, F. Tufvesson, A. Molisch, and C. F. Mecklenbraüker, "Multi-dimensional K-factor analysis for V2V radio channels in open suburban street crossings," in *Proc. IEEE Symp. Personal Indoor Mobile Radio Commun.*, Istanbul, Turkey, Sep. 2010, pp. 58–63.

[79] A. Abdi, C. Tepedelenlioglu, M. Kaveh, and G. Giannakis, "On the estimation of the K parameter for the Rice fading distribution," *IEEE Commun. Lett.*, vol. 5, no. 3, pp. 92–94, Mar. 2001.

[80] N. C. Sagias, D. A. Zogas, G. K. Karagiannidis, and G. S. Tombras, "Channel capacity and Second-order statistics in Weibull fading," *IEEE Commun. Lett.*, vol. 8, no. 6, pp. 377–379, Jun. 2004.

[81] W. C.-Y Lee, "Finding the approximate angular probability density function of wave arrival by using a directional antenna," *IEEE Trans. Veh. Technol.*, vol. 21, no. 3, pp. 328–334, May 1973.

[82] C. A. Gutierrez and M. Pätzold, "Sum-of-sinusoids-based simulation of flat fading wireless propagation channels under non-isotropic scattering conditions," in *Proc. IEEE Global Telecomm. Conf.*, Nov. 2007.

[83] K. V. Mardia and P. E. Jupp, *Directional Statistics*, Wiley, 1st edition, Jan. 1999.

[84] C. Patel, G. Stüber, and T. Pratt, "Comparative analysis of statistical models for the simulation of Rayleigh faded cellular channels," *IEEE Trans. Commun.*, vol. 53, pp. 1017–1026, Jun. 2005.

APPENDICES

APPENDIX A

Proof Of (2.3.1) And (2.3.3), Autocorrelation And Cross-correlation For Model B

From (2.2.7), the real and imaginary parts of Model B are given, respectively, by

$$g_c(t) = \mathrm{Re}\big(g(t)\big) = \sqrt{\frac{2}{NM}} \sum_{n,m=1}^{N,M} \big(A_n(t)B_m(t) - C_n(t)D_m(t)\big) \tag{A.0.1}$$

$$g_s(t) = \mathrm{Im}\big(g(t)\big) = \sqrt{\frac{2}{NM}} \sum_{n,m=1}^{N,M} \big(A_n(t)D_m(t) + C_n(t)B_m(t)\big) \tag{A.0.2}$$

For brevity of notations, we replace $t+\tau$ with ϱ in the proceeding appendices. The autocorrelation can be obtained by

$$\begin{aligned}\mathbb{E}\big[g_c(t)g_c(\varrho)\big] &= \frac{2}{NM}\mathbb{E}\Bigg[\sum_{n,m=1}^{N,M}\big(A_n(t)B_m(t) - C_n(t)D_m(t)\big)\sum_{k,j=1}^{N,M}\big(A_k(\varrho)B_j(\varrho) - C_k(\varrho)D_j(\varrho)\big)\Bigg] \\ &= \frac{2}{NM}\mathbb{E}\Big[\sum_{n,k=1}^{N,N} A_n(t)A_k(\varrho)\sum_{m,j=1}^{M,M} B_m(t)B_j(\varrho) + \sum_{n,k=1}^{N,N} C_n(t)C_k(\varrho)\sum_{m,j=1}^{M,M} D_m(t)D_j(\varrho) \\ &\quad - \sum_{n,k=1}^{N,N} A_n(t)C_k(\varrho)\sum_{m,j=1}^{M,M} B_m(t)D_j(\varrho) - \sum_{n,k=1}^{N,N} C_n(t)A_k(\varrho)\sum_{m,j=1}^{M,M} D_m(t)B_j(\varrho)\Big]\end{aligned} \tag{A.0.3}$$

The cross-correlation is evaluated as

$$\mathbb{E}\big[g_c(t)g_s(\varrho)\big] = \mathbb{E}\Big[\frac{2}{NM}\sum_{n,m=1}^{N,M}\big(A_n(t)B_m(t) - C_n(t)D_m(t)\big)\sum_{j,k=1}^{N,M}\big(A_j(\varrho)D_k(\varrho) + C_j(\varrho)B_k(\varrho)\big)\Big] \tag{A.0.4}$$

Since $\theta_n, \Theta_n, \Phi_m, \Psi_m \in [-\pi, \pi)$ are statistically independent and uniformly distributed for all n and m, we have $\mathbb{E}[\sum_{n,k=1,n\neq k}^{N,N} A_n(t)A_k(\varrho)] = \mathbb{E}[\sum_{n,k=1,n\neq k}^{N,N} C_n(t)C_k(\varrho)] = 0$, and $\mathbb{E}[\sum_{m,j=1,m\neq j}^{M,M} B_m(t)B_j(\varrho)] = \mathbb{E}[\sum_{m,j=1,m\neq j}^{M,M} D_m(t)D_j(\varrho)] = 0$. It is easy to justify $\mathbb{E}\big[g_c(t)g_c(\varrho)\big] = J_0(2\pi f_1\tau)J_0(2\pi f_2\tau)$ and $\mathbb{E}\big[g_c(t)g_s(\varrho)\big] = 0$.

Using [63] (p. 420-421), the following identities are listed for the convenience of the proceeding proof of the models' statistical properties.

$$\mathbb{E}[\sum_{n,k=1}^{N,N} A_n(t)A_k(\varrho)] = \mathbb{E}[\sum_{n}^{N} A_n(t)A_n(\varrho)] = \frac{1}{2}\mathbb{E}[\sum_{n=1}^{N}\tilde{A}_n(\tau)] = \frac{N}{2}J_0(2\pi f_1\tau) \tag{A.0.5}$$

$$\mathbb{E}[\sum_{n,k=1}^{N,N} C_n(t)C_k(\varrho)] = \mathbb{E}[\sum_{n}^{N} C_n(t)C_n(\varrho)] = \frac{1}{2}\mathbb{E}[\sum_{n=1}^{N} \tilde{C}_n(\tau)] = \frac{N}{2}J_0(2\pi f_1\tau) \tag{A.0.6}$$

$$\sum_{m=1,j}^{M,M} \mathbb{E}[B_m(t)B_j(\varrho)] = \sum_{m=1}^{M} \mathbb{E}[B_m(t)B_m(\varrho)] = \frac{1}{2}\mathbb{E}[\sum_{m=1}^{M} \tilde{B}_m(\tau)] = \frac{M}{2}J_0(2\pi f_2\tau) \tag{A.0.7}$$

$$\sum_{m=1,j}^{M,M} \mathbb{E}[D_m(t)D_j(\varrho)] = \sum_{m=1}^{M} \mathbb{E}[D_m(t)D_m(\varrho)] = \frac{1}{2}\sum_{m=1}^{M} \mathbb{E}[\tilde{D}_m(\tau)] = \frac{M}{2}J_0(2\pi f_2\tau) \tag{A.0.8}$$

$$\sum_{n,k=1}^{N,N} \mathbb{E}[A_n(t)C_k(\varrho)] = \sum_{m,j=1}^{M,M} \mathbb{E}[B_m(t)D_j(\varrho)] = 0. \tag{A.0.9}$$

APPENDIX B

Proof Of (2.3.14) And (2.3.17), Autocorrelation And Cross-correlation For Model D

The real and imaginary parts of Model D, respectively, are

$$h_c(t) = \mathrm{Re}\big(h(t)\big) = \frac{1}{\sqrt{1+K}}\bigg(\sqrt{\frac{1}{2}}g_c(t) + \sqrt{K}\cos\big(L(t)\big)\bigg), \tag{B.0.1}$$

$$h_s(t) = \mathrm{Im}\big(h(t)\big) = \frac{1}{\sqrt{1+K}}\bigg(\sqrt{\frac{1}{2}}g_s(t) + \sqrt{K}\sin\big(L(t)\big)\bigg) \tag{B.0.2}$$

where $L(t) = 2\pi f_3 t\cos(\phi_3) + \phi_0$. The autocorrelation is calculated as

$$\mathbb{E}\big[h_c(t)h_c(\varrho)\big] = \frac{1}{1+K}\mathbb{E}\bigg[\bigg(\sqrt{\frac{1}{2}}g_c(t) + \sqrt{K}\cos\big(L(t)\big)\bigg)\bigg(\sqrt{\frac{1}{2}}g_c(\varrho) + \sqrt{K}\cos\big(L(\varrho)\big)\bigg)\bigg] \tag{B.0.3}$$

The cross-correlation of Model D can be obtained as

$$\mathbb{E}\big[h_c(t)h_s(t+\tau)\big] = \frac{1}{1+K}\mathbb{E}\bigg[\bigg(\sqrt{\frac{1}{2}}g_c(t) + \sqrt{K}\cos\big(L(t)\big)\bigg)\bigg(\sqrt{\frac{1}{2}}g_s(t+\tau) + \sqrt{K}\sin\big(L(t+\tau)\big)\bigg)\bigg] \tag{B.0.4}$$

Notice that the phase ϕ_0 in $L(t)$ and $L(\varrho)$ is independent of other random variables in $g_c(t)$ and $g_s(t)$. Taking the expectation with respect to ϕ_0 and using the results in the autocorrelation and cross-correlation for Model B, one can obtain the autocorrelation and cross-correlation as specified in (2.3.14) and (2.3.17).

APPENDIX C

Proof Of (2.3.5): Squared Envelope Correlation For Model B

The squared envelope correlation for Model B can be written as $R_{|g|^2|g|^2}(\tau) = \mathbb{E}\big[g_c^2(t)g_c^2(\varrho)\big]$ $+\mathbb{E}\big[g_c^2(t)g_s^2(\varrho)\big] + \mathbb{E}\big[g_s^2(t)g_c^2(\varrho)\big] + \mathbb{E}\big[g_s^2(t)g_s^2(\varrho)\big]$. The first term is expressed as

$$\mathbb{E}\big[g_c^2(t)g_c^2(\varrho)\big] = \frac{4}{N^2M^2}\mathbb{E}\Big[\sum_{n,m=1}^{N,M}\big(A_n(t)B_m(t) - C_n(t)D_m(t)\big)\sum_{u,p=1}^{N,M}\big(A_u(t)B_p(t) - C_u(t)D_p(t)\big) \times \sum_{q,r=1}^{N,M}\big(A_q(\varrho)B_r(\varrho) - C_q(\varrho)D_r(\varrho)\big)\sum_{s,j=1}^{N,M}\big(A_s(\varrho)B_j(\varrho) - C_s(\varrho)D_j(\varrho)\big)\Big]. \tag{C.0.1}$$

Expanding (C.0.1) and taking expectation with respect to the phases, we obtain $\mathbb{E}\big[g_c^2(t)g_c^2(\varrho)\big]$ $= \frac{4}{N^2M^2}(\Upsilon_A\Upsilon_B+\Upsilon_C\Upsilon_D+\frac{M^2N^2}{8}+4\kappa)$, where $\Upsilon_X = \mathbb{E}\big[\sum_n^N X_n(t)\sum_u^N X_u(t)\sum_q^N X_q(\varrho)\sum_s^N X_s(\varrho)\big]$, where $X = \{A, B, C, D\}$, and

$$\kappa = \mathbb{E}\big[\sum_{n,s}^{N,N} A_n(t)A_s(\varrho)\sum_{u,q}^{N,N} C_u(t)C_q(\varrho)\sum_{m,j}^{M,M} B_m(t)B_j(\varrho)\sum_{p,r=1}^{M,M} D_p(t)D_r(\varrho)] \tag{C.0.2}$$

Similarly, we have $\mathbb{E}\big[g_c^2(t)g_s^2(\varrho)\big] = \mathbb{E}\big[g_s^2(t)g_c^2(\varrho)\big] = \frac{4}{N^2M^2}\big(\frac{M^2}{4}(\Upsilon_A+\Upsilon_C)+\frac{N^2}{4}(\Upsilon_B+\Upsilon_D)-4\kappa\big)$, and $\mathbb{E}\big[g_s^2(t)g_s^2(\varrho)\big] = \frac{4}{N^2M^2}(\Upsilon_A\Upsilon_D + \Upsilon_C\Upsilon_B + \frac{M^2N^2}{8} + 4\kappa)$. The term Υ_A is evaluated as

$$\Upsilon_A = \mathbb{E}\Big[\sum_p^N A_p^2(t)\sum_j^N A_j^2(\varrho)\Big] + \mathbb{E}\Big[\sum_{n,u,n\neq u}^{N,N} A_n(t)A_u(t)\sum_{q,s,q\neq s}^{N,N} A_q(\varrho)A_s(\varrho)\Big] \tag{C.0.3}$$

The first term in (C.0.3) is obtained as

$$\mathbb{E}\big[\sum_p^N A_p^2(t)\sum_j^N A_j^2(\varrho)\big] = \frac{2N^2 + NJ_0(4\pi f_1\tau)}{8}. \tag{C.0.4}$$

The second term in (C.0.3) contains the following seven cases:

- Case 1. $n \neq u, q \neq s, n = q, u \neq s$;
- Case 2. $n \neq u, q \neq s, n = s, q \neq u$;
- Case 3. $n \neq u, q \neq s, u = q, n \neq s$;

- Case 4. $n \neq u, q \neq s, u = s, n \neq q$;
- Case 5. $n \neq u, q \neq s, n \neq q, u \neq s$;
- Case 6. $n \neq u, q \neq s, n = q, u = s$;
- Case 7. $n \neq u, q \neq s, n = s, u = q$.

The value of $\mathbb{E}\big[\sum_n^N A_n(t)A_n(\varrho)\sum_{s,s\neq n}^N A_s(t)A_s(\varrho)\big]$ is zero for Cases 1 to 5 and identical for Cases 6 and 7, and $\mathbb{E}\big[\sum_n^N A_n(t)A_n(\varrho)\sum_{s,s\neq n}^N A_s(t)A_s(\varrho)\big]_{\text{case 6 or 7}} = \frac{N^2J_0^2(2\pi f_1\tau)-\sum_n^N\Big(\mathbb{E}[\tilde{A}_n(\tau)]\Big)^2}{4}$. Therefore, we have $\Upsilon_A = \frac{2N^2+NJ_0(4\pi f_1\tau)+4N^2J_0^2(2\pi f_1\tau)}{8} - \frac{\sum_n^N\Big(\mathbb{E}[\tilde{A}_n(\tau)]\Big)^2}{2}$. In fact, the value of Υ_A can also be obtained following the steps in (48) Appendix I [84].

Similarly, we have $\Upsilon_C = \frac{2N^2+NJ_0(4\pi f_1\tau)+4N^2J_0^2(2\pi f_1\tau)}{8} - \frac{\sum_n^N\Big(\mathbb{E}[\tilde{C}_n(\tau)]\Big)^2}{2}$. It is straightforward to justify $\mathbb{E}\big[\tilde{C}_n(\tau)] = \mathbb{E}\big[\tilde{C}_{N-n}(\tau)], n = 1, \cdots, N$ by the following steps:

$$\begin{aligned}\mathbb{E}\big[\tilde{C}_n(\tau)] &= \int_{-\pi}^{\pi}\cos\big(2\pi f_1\tau\cos(\frac{2n\pi-\pi+\psi}{4N})\big)\frac{1}{2\pi}d\psi\\ &= \int_{\frac{(n-1)\pi}{2N}}^{\frac{n\pi}{2N}}\cos\big(2\pi f_1\tau\cos(\theta)\big)\frac{4N}{2\pi}d\psi\\ &= \int_{\frac{(N-n-1)\pi}{2N}}^{\frac{(N-n)\pi}{2N}}\cos\big(2\pi f_1\tau\sin(\varphi)\big)\frac{4N}{2\pi}d\varphi = \mathbb{E}\big[\tilde{C}_{N-n}(\tau)]\end{aligned} \tag{C.0.5}$$

Denote $\xi(f_1,\tau) = \sum_n^N\Big(\mathbb{E}\big[\tilde{A}_n(\tau)\big]\Big)^2 = \sum_n^N\Big(\mathbb{E}\big[\tilde{C}_n(\tau)\big]\Big)^2$. Then, we have

$$\Upsilon_A = \Upsilon_C = \frac{2N^2+NJ_0(4\pi f_1\tau)+4N^2J_0^2(2\pi f_1\tau)}{8} - \frac{\xi(f_1,\tau)}{2} \tag{C.0.6}$$

$$\Upsilon_B = \Upsilon_D = \frac{2M^2+MJ_0(4\pi f_2\tau)+4M^2J_0^2(2\pi f_2\tau)}{8} - \frac{\xi(f_2,\tau)}{2}, \tag{C.0.7}$$

where $\xi(f_2,\tau) = \sum_m^M\Big(\mathbb{E}\big[\tilde{B}_m(\tau)\big]\Big)^2 = \sum_m^M\Big(\mathbb{E}\big[\tilde{D}_n(\tau)\big]\Big)^2$. Inserting the results for $\mathbb{E}\big[g_c^2(t)g_c^2(\varrho)\big]$, $\mathbb{E}\big[g_c^2(t)g_s^2(\varrho)\big], \mathbb{E}\big[g_s^2(t)g_c^2(\varrho)\big]$, and $\mathbb{E}\big[g_s^2(t)g_s^2(\varrho)\big]$ into $R_{|g|^2|g|^2}(\tau)$, we obtain

$$\begin{aligned}R_{|g|^2|g|^2}(\tau) &= \frac{4}{N^2M^2}\Big(\Upsilon_A+\Upsilon_C+\frac{N^2}{2}\Big)\Big(\Upsilon_B+\Upsilon_D+\frac{M^2}{2}\Big)\\ &= \frac{4}{N^2M^2}\Big(N^2+N^2J_0^2(2\pi f_1\tau)+\frac{NJ_0(4\pi f_1\tau)}{4}-\xi(f_1,\tau)\Big)\\ &\quad\times\Big(M^2+M^2J_0^2(2\pi f_2\tau)+\frac{MJ_0(4\pi f_2\tau)}{4}-\xi(f_2,\tau)\Big).\end{aligned} \tag{C.0.8}$$

Expanding (C.0.8) yields (2.3.5).

APPENDIX D

Proof Of (2.3.20): Squared Envelope Correlation For Model D

The squared envelope correlation for Model D contains four terms as indicated in (2.3.19). The first term is evaluated as

$$\begin{aligned}\mathbb{E}\big[h_c^2(t)h_c^2(\varrho)\big] &= \frac{1}{(1+K)^2}\mathbb{E}\Bigg[\bigg(\sqrt{\frac{1}{2}}g_c(t)+\sqrt{K}\cos\big(L(t)\big)\bigg)^2\bigg(\sqrt{\frac{1}{2}}g_c(\varrho)+\sqrt{K}\cos\big(L(\varrho)\big)\bigg)^2\Bigg]\\ &= \frac{1}{(1+K)^2}\mathbb{E}\Bigg[\bigg(\frac{1}{2}g_c^2(t)+\sqrt{2K}g_c(t)\cos\big(L(t)\big)+K\cos^2\big(L(t)\big)\bigg)\\ &\qquad\times\bigg(\frac{1}{2}g_c^2(\varrho)+\sqrt{2K}g_c(\varrho)\cos\big(L(\varrho)\big)+K\cos^2\big(L(\varrho)\big)\bigg)\Bigg] \qquad \text{(D.0.1)}\end{aligned}$$

Note that $\mathbb{E}[g_c(t)] = \mathbb{E}[g_c(\varrho)] = 0$, $\mathbb{E}[\cos\big(L(\ell t)\big)] = \mathbb{E}[\cos\big(\ell L(\varrho)\big)] = 0, \ell = 1, 2$, and $\mathbb{E}[g_c^2(t)] = \mathbb{E}[g_c^2(\varrho)] = R_{g_cg_c}(0) = 1$. We have

$$\begin{aligned}\mathbb{E}\big[h_c^2(t)h_c^2(\varrho)\big] = \frac{1}{(1+K)^2}\Bigg(&\frac{1}{4}\mathbb{E}\big[g_c^2(t)g_c^2(\varrho)\big]+2KR_{g_cg_c}(\tau)\mathbb{E}\big[\cos\big(L(t)\big)\cos\big(L(\varrho)\big)\big]\\ &+\frac{K}{2}\mathbb{E}\big[\cos^2\big(L(t)\big)+\cos^2\big(L(\varrho)\big)\big]+K^2\mathbb{E}\big[\cos^2\big(L(t)\big)\cos^2\big(L(\varrho)\big)\big]\Bigg)\end{aligned} \qquad \text{(D.0.2)}$$

The autocorrelation of the squared quadrature component $\mathbb{E}\big[h_s^2(t)h_s^2(\varrho)\big]$ can be evaluated following similar steps in obtaining $\mathbb{E}\big[h_c^2(t)h_c^2(\varrho)\big]$. Using identities $\mathbb{E}\big[\cos\big(L(t)\big)\cos\big(L(\varrho)\big)\big] = \frac{1}{2}\cos\big(2\pi f_3\tau\cos(\phi_3)\big), \mathbb{E}\big[\cos^2\big(L(t)\big)\big] = \mathbb{E}\big[\cos^2\big(L(\varrho)\big)\big] = \frac{1}{2}$, and $\mathbb{E}\big[\cos^2\big(L(t)\big)\cos^2\big(L(\varrho)\big)\big] = \frac{1}{4}+\frac{1}{8}\cos\big(4\pi f_3\tau\cos(\phi_3)\big)$, we summarize the auto- and cross-correlations, respectively, as

$$\mathbb{E}\big[h_x^2(t)h_x^2(\varrho)\big] = \frac{2\mathbb{E}\big[g_x^2(t)g_x^2(\varrho)\big]+8KR_{g_xg_x}(\tau)\cos\big(2\pi f_3\tau\cos(\phi_3)\big)+4K+2K^2+K^2\cos\big(4\pi f_3\tau\cos(\phi_3)\big)}{8(1+K)^2} \qquad \text{(D.0.3)}$$

$$\mathbb{E}\big[h_c^2(t)h_s^2(\varrho)\big] = \mathbb{E}\big[h_s^2(t)h_c^2(\varrho)\big] = \frac{2\mathbb{E}\big[g_c^2(t)g_s^2(\varrho)\big]+4K+2K^2-K^2\cos\big(4\pi f_3\tau\cos(\phi_3)\big)}{8(1+K)^2} \qquad \text{(D.0.4)}$$

where $x = \{c, s\}$. Inserting (D.0.3) and (D.0.4) into (2.3.19) yields (2.3.20).

APPENDIX E

Proof Of (2.3.13): Variance Of Time-average Correlations For Model B

The variance of the time-average autocorrelation of the real part for Model B is $\mathrm{Var}[\tilde{R}_{g_cg_c}(\tau)] = \mathbb{E}[\tilde{R}^2_{g_cg_c}(\tau)] - (R_{g_cg_c}(\tau))^2$. The first term is evaluated as

$$\begin{aligned}\mathbb{E}[\tilde{R}^2_{g_cg_c}(\tau)] &= \frac{1}{4M^2N^2}\mathbb{E}\Big[\sum_{n,m=1}^{N,M}\big(\tilde{A}_n(\tau)\tilde{B}_m(\tau)+\tilde{C}_n(\tau)\tilde{D}_m(\tau)\big)\sum_{p,q=1}^{N,M}\big(\tilde{A}_p(\tau)\tilde{B}_q(\tau)+\tilde{C}_p(\tau)\tilde{D}_q(\tau)\big)\Big] \\ &= \frac{1}{4N^2M^2}\Bigg(\mathbb{E}\Big[\sum_{n,q=1}^{N,N}\tilde{A}_n(\tau)\tilde{A}_q(\tau)\sum_{m,p=1}^{M,M}\tilde{B}_m(\tau)\tilde{B}_p(\tau)\Big]+2\mathbb{E}\Big[\sum_{n,q=1}^{N,N}\tilde{A}_n(\tau)\tilde{C}_q(\tau)\sum_{m,p=1}^{M,M}\tilde{B}_m(\tau)\tilde{D}_p(\tau)\Big] \\ &\qquad + \mathbb{E}\Big[\sum_{n,q=1}^{N,N}\tilde{C}_n(\tau)\tilde{C}_q(\tau)\sum_{m,p=1}^{M,M}\tilde{D}_m(\tau)\tilde{D}_p(\tau\Big]\Bigg) \qquad \text{(E.0.1)}\end{aligned}$$

We have the following identities:

$$\begin{aligned}\mathbb{E}\big[\sum_{n,q=1}^{N,N}\tilde{A}_n(\tau)\tilde{A}_q(\tau)\big] &= N^2J_0^2(2\pi f_1\tau) + \mathbb{E}\big[\sum_{n=1}^{N}\tilde{A}_n(\tau)\tilde{A}_n(\tau)\big] - \sum_{n=1}^{N}\mathbb{E}\big[\tilde{A}_n(\tau)\big]\mathbb{E}\big[\tilde{A}_n(\tau)\big] \\ &= N^2J_0^2(2\pi f_1\tau) + \frac{N}{2} + \frac{NJ_0(4\pi f_1\tau)}{2} - \xi(f_1,\tau) \qquad \text{(E.0.2)}\end{aligned}$$

$$\mathbb{E}\big[\sum_{n,q=1}^{N,N}\tilde{C}_n(\tau)\tilde{C}_q(\tau)\big] = \mathbb{E}\big[\sum_{n,q=1}^{N,N}\tilde{A}_n(\tau)\tilde{A}_q(\tau)\big] \qquad \text{(E.0.3)}$$

$$\mathbb{E}\big[\sum_{m,p=1}^{M,M}\tilde{B}_m(\tau)\tilde{B}_p(\tau)\big] = \mathbb{E}\big[\sum_{m,p=1}^{M,M}\tilde{D}_m(\tau)\tilde{D}_p(\tau)\big] = M^2J_0^2(2\pi f_2\tau) + \frac{M}{2} + \frac{MJ_0(4\pi f_2\tau)}{2} - \xi(f_2,\tau) \qquad \text{(E.0.4)}$$

$$\mathbb{E}\big[\sum_{n,q=1}^{N,N}\tilde{A}_n(\tau)\tilde{C}_q(\tau)\big] = N^2J_0^2(2\pi f_1\tau) + V_{\tilde{A}\tilde{C}} \qquad \text{(E.0.5)}$$

$$\mathbb{E}\big[\sum_{m,p=1}^{M,M}\tilde{B}_m(\tau)\tilde{D}_p(\tau)\big] = M^2J_0^2(2\pi f_2\tau) + V_{\tilde{B}\tilde{D}} \qquad \text{(E.0.6)}$$

where $V_{\tilde{A}\tilde{C}} = \sum_{n=1}^{N}\big(\mathbb{E}[\tilde{A}_n(\tau)\tilde{C}_n(\tau)] - \mathbb{E}[\tilde{A}_n(\tau)]\mathbb{E}[\tilde{C}_n(\tau)]\big)$, $V_{\tilde{B}\tilde{D}} = \sum_{m=1}^{M}\big(\mathbb{E}[\tilde{B}_m(\tau)\tilde{D}_m(\tau)] - \mathbb{E}[\tilde{B}_m(\tau)]\mathbb{E}[\tilde{D}_m(\tau)]\big)$. Inserting (E.0.2) to (E.0.6) into (E.0.1), we obtain

$$\begin{aligned}\mathbb{E}[\tilde{R}^2_{g_cg_c}(\tau)] &= \frac{1}{4M^2N^2}\Big(2\big(N^2J_0^2(2\pi f_1\tau) + \frac{N}{2} + \frac{NJ_0(4\pi f_1\tau)}{2} - \xi(f_1,\tau)\big) \\ &\times\big(M^2J_0^2(2\pi f_2\tau)+\frac{M}{2}+\frac{MJ_0(4\pi f_2\tau)}{2}-\xi(f_2,\tau)\big)+2\big(N^2J_0^2(2\pi f_1\tau)+V_{\tilde{A}\tilde{C}}\big)\big(M^2J_0^2(2\pi f_2\tau)+V_{\tilde{B}\tilde{D}}\big)\Big)\end{aligned}$$

$$= \frac{1}{8M^2N^2}\Big(\big(2N^2J_0^2(2\pi f_1\tau)+N+NJ_0(4\pi f_1\tau)-2\ \xi(f_1,\tau)\big)$$
$$\times\big(2M^2J_0^2(2\pi f_2\tau)+M+MJ_0(4\pi f_2\tau)-2\ \xi(f_2,\tau)\big)$$
$$+4\big(N^2J_0^2(2\pi f_1\tau)+V_{\tilde{A}\tilde{C}}\big)\big(M^2J_0^2(2\pi f_2\tau)+V_{\tilde{B}\tilde{D}}\big)\Big) \tag{E.0.7}$$

Recall $\big(\tilde{R}_{g_cg_c}(\tau)\big)^2 = J_0^2(2\pi f_1\tau)J_0^2(2\pi f_2\tau)$. We have

$$\begin{aligned}\mathrm{Var}[\tilde{R}_{g_cg_c}(\tau)] = \frac{1}{8M^2N^2}\Big(&2M^2J_0^2(2\pi f_2\tau)\big(N+NJ_0(4\pi f_1\tau)-2\ \xi(f_1,\tau)+2V_{\tilde{A}\tilde{C}}\big)\\ &+2N^2J_0^2(2\pi f_1\tau)\big(M+MJ_0(4\pi f_2\tau)-2\ \xi(f_2,\tau)+2V_{\tilde{B}\tilde{D}}\big)\\ &+\big(N+NJ_0(4\pi f_1\tau)-2\ \xi(f_1,\tau)\big)\big(M+MJ_0(4\pi f_2\tau)-2\ \xi(f_2,\tau)\big)+4V_{\tilde{A}\tilde{C}}V_{\tilde{B}\tilde{D}}\Big)\end{aligned} \tag{E.0.8}$$

Reorganizing (E.0.8), one can obtain (2.3.13).

The variance of time-average autocorrelation of the imaginary part of Model B is $\mathrm{Var}[\tilde{R}_{g_sg_s}(\tau)] = \mathbb{E}[\tilde{R}^2_{g_sg_s}(\tau)] - (R_{g_sg_s}(\tau))^2$. The first term is evaluated as

$$\begin{aligned}\mathbb{E}[\tilde{R}^2_{g_sg_s}(\tau)] &= \frac{1}{4M^2N^2}\mathbb{E}\Big[\sum_{n,m=1}^{N,M}\big(\tilde{A}_n(\tau)\tilde{D}_m(\tau)+\tilde{C}_n(\tau)\tilde{B}_m(\tau)\big)\sum_{p,q=1}^{N,M}\big(\tilde{A}_p(\tau)\tilde{D}_q(\tau)+\tilde{C}_p(\tau)\tilde{B}_q(\tau)\big)\Big]\\ &= \frac{1}{4N^2M^2}\Bigg(\mathbb{E}\Big[\sum_{n,q=1}^{N,N}\tilde{A}_n(\tau)\tilde{A}_q(\tau)\sum_{m,p=1}^{M,M}\tilde{D}_m(\tau)\tilde{D}_p(\tau)\Big]+2\mathbb{E}\Big[\sum_{n,q=1}^{N,N}\tilde{A}_n(\tau)\tilde{C}_q(\tau)\sum_{m,p=1}^{M,M}\tilde{B}_m(\tau)\tilde{D}_p(\tau)\Big]\\ &\qquad+\mathbb{E}\Big[\sum_{n,q=1}^{N,N}\tilde{C}_n(\tau)\tilde{C}_q(\tau)\sum_{m,p=1}^{M,M}\tilde{B}_m(\tau)\tilde{B}_p(\tau)\Big]\Bigg)\end{aligned} \tag{E.0.9}$$

We have $\mathrm{Var}[\tilde{R}_{g_sg_s}(\tau)] = \mathrm{Var}[\tilde{R}_{g_cg_c}(\tau)]$.

APPENDIX F

Proof Of (2.3.25): Variance Of Time-average Correlations For Model D

We present the derivation of the variance of the time-average autocorrelation of the in-phase component in (2.3.25), while the same steps can be applied to obtain the variance of the time-average autocorrelation of the quadrature component. The variance of the time-average autocorrelation of the in-phase component for model D is $\mathrm{Var}\big[\tilde{R}_{h_c h_c}(\tau)\big] = \mathbb{E}[\tilde{R}^2_{h_c h_c}(\tau)] - \big(R_{h_c h_c}(\tau)\big)^2$. The first term is evaluated as

$$\mathbb{E}[\tilde{R}^2_{h_c h_c}(\tau)] = \mathbb{E}\bigg[\bigg(\frac{\tilde{R}_{g_c g_c}(\tau) + K\cos\big(2\pi f_3 \tau\cos(\phi_3)\big)}{2(1+K)}\bigg)^2\bigg]$$
$$= \frac{1}{4(1+K)^2}\Big(\mathbb{E}\big[\tilde{R}^2_{g_c g_c}(\tau)\big] + 2K\cos\big(2\pi f_3\tau\cos(\phi_3)\big)\mathbb{E}\big[\tilde{R}_{g_c g_c}(\tau)\big] + \big(K\cos(2\pi f_3\tau\cos(\phi_3))\big)^2\Big) \tag{F.0.1}$$

Recall $\mathbb{E}[\tilde{R}_{g_c g_c}(\tau)] = J_0(2\pi f_1\tau)J_0(2\pi f_2\tau)$. Using $\mathbb{E}\big[\tilde{R}^2_{g_c g_c}(\tau)\big]$ obtained in Appendix E and $R_{h_c h_c}(\tau)$ from Appendix B, it is easy to obtain (2.3.25).

APPENDIX G

Proof For PDF Of Envelope For Models A and B

The pdf and phase distribution of Models A and B are readily available in the literature [59]. Denote $g = g_1 g_2 = g_c + j g_s$, $g_1 = x_1 + j x_2$, $g_2 = y_1 + j y_2$, $x_1, x_2 \sim \mathcal{N}(0, \sigma_1^2)$, and $y_1, y_2 \sim \mathcal{N}(0, \sigma_2^2)$ are i.i.d. zero mean Gaussian normally distributed. The joint PDF for the real and imaginary parts of g is given as $p_{g_c g_s}(g_c, g_s) = \frac{1}{2\pi\sigma_1^2\sigma_2^2} K_0\left(\frac{\sqrt{g_c^2+g_s^2}}{\sigma_1\sigma_2}\right)$. To find the pdf of the envelope, we transform the Cartesian coordinates (g_c, g_s) to polar coordinates (z, η), where $z = \sqrt{g_c^2 + g_s^2}$, and $\eta = \arctan\left(\frac{g_s(t)}{g_c(t)}\right)$. The resulted transformation Jacobian is $1/z$. The joint pdf of the envelope and phase is given by $p_{z,\eta}(z, \eta) = z p_{g_c g_s}(g_c, g_s) = \frac{z}{2\pi\sigma_1^2\sigma_2^2} K_0\left(\frac{z}{\sigma_1\sigma_2}\right)$. The PDF of the envelope is obtained as $p_z(z) = \frac{z}{\sigma_1^2\sigma_2^2} K_0\left(\frac{z}{\sigma_1\sigma_2}\right)$. Recognizing $\sigma_1 = \sigma_2 = 1/\sqrt{\sqrt{2}}$ for Models A and B, one can obtain the PDF of their envelopes.

APPENDIX H

Proof Of (3.5.2), Level Crossing Rate For M2M Rician Channel

The LCR can be obtained by considering a general case where the scatter is asymmetric around the spectral [36]. The first and second moments of the power spectral density (psd), b_1 and b_2, are used to obtain the joint pdf (2.91) in [36]. Let $h_{R_c}(t) = \mathrm{Re}[h_R(t)]$ denote the in-phase component of the statistical channel model in (3.4.10). The autocorrelation of the in-phase component is written as $R_{h_{R_c}h_{R_c}}(\tau) = \mathbb{E}\big[h_{R_c}(t)h_{R_c}(t+\tau)\big] = \frac{\Omega}{2(1+K)}\Big(J_0(2\pi f_1\tau)J_0(2\pi f_2\tau) + K\cos(2\pi f_3\tau\cos\theta_{\mathrm{L}})\Big)$, where $J_0(\cdot)$ is the zero-order Bessel function first kind. The second moment of the psd is obtained by $b_2 = -d^2R_{h_{R_c}h_{R_c}}(\tau)/d\tau^2|_{\tau=0}$. Using the identities in Bessel function, $J_{-n}(x) = (-1)^nJ_n(x)$, $\frac{d}{dx}J_n(x) = \frac{J_{n-1}(x)-J_{n+1}(x)}{2}$, and taking the second derivative for the autocorrelation, we obtain

$$b_2 = \frac{\Omega\ \pi^2\big(f_1^2 + f_2^2 + 2Kf_3^2\cos^2\theta_{\mathrm{L}}\big)}{(1+K)}. \tag{H.0.1}$$

It is observed that (H.0.1) can also be calculated as

$$b_2 = (2\pi)^2 b_0 \int_{-\pi}^{\pi} \big(\sqrt{f_1^2+f_2^2}\cos\alpha - \sqrt{K}f_3\cos\theta_{\mathrm{L}}\big)^2 \frac{d\alpha}{2\pi} \tag{H.0.2}$$

The first moment of the psd can be obtained as

$$b_1 = 2\pi b_0 \int_{-\pi}^{\pi} \big(\sqrt{f_1^2+f_2^2}\cos\alpha - \sqrt{K}f_3\cos\theta_{\mathrm{L}}\big) \frac{d\alpha}{2\pi} \tag{H.0.3}$$

Plugging $B = b_0b_2 - b_1^2 = \frac{\Omega^2\pi^2(f_1^2+f_2^2)}{2(1+K)^2}$, b_0, b_1, and b_2 into (3.5.1), one can obtain (3.5.2) from the integral over the slope.